



**AFRL-RQ-WP-TR-2017-0098**

**HYPERSONIC BOUNDARY LAYER TRANSITION  
EXPERIMENTS - HYPERSONIC INTERNATIONAL  
FLIGHT RESEARCH EXPERIMENTATION 5 (HiFIRE-5)  
AND CIRCULAR CONE**

**Roger Kimmel, Joseph S. Jewell, and Matthew Borg  
Hypersonic Sciences Branch  
High Speed Systems Division**

**Benjamin Hagen  
Aero Validation Branch  
Aerospace Vehicles Division**

**Brian Lam  
Spectral Energies, LLC**

**Nick Parziale  
Stevens Institute of Technology**

**OCTOBER 2016  
Interim Report**

**DISTRIBUTION STATEMENT A: Approved for public release.  
Distribution is unlimited.**

**AIR FORCE RESEARCH LABORATORY  
AEROSPACE SYSTEMS DIRECTORATE  
WRIGHT-PATTERSON AIR FORCE BASE, OH 45433-7542  
AIR FORCE MATERIEL COMMAND  
UNITED STATES AIR FORCE**

## Notice and Signature Page

Using Government drawings, specifications, or other data included in this document for any purpose other than Government procurement does not in any way obligate the U.S. Government. The fact that the Government formulated or supplied the drawings, specifications, or other data does not license the holder or any other person or corporation; or convey any rights or permission to manufacture, use, or sell any patented invention that may relate to them.

This report was cleared for public release by the 88<sup>TH</sup> Air Base Wing Public Affairs Office and is available to the general public, including foreign nationals.

Copies may be obtained from the Defense Technical Information Center (DTIC)  
(<http://www.dtic.mil>).

AFRL-RQ-WP-TR-2017-0098 HAS BEEN REVIEWED AND IS APPROVED FOR  
PUBLICATION IN ACCORDANCE WITH ASSIGNED DISTRIBUTION STATEMENT.

\*//Signature//



---

Roger L. Kimmel  
Principal Aerospace Engineer  
Hypersonic Sciences Branch

\*//Signature//



---

Michael S. Brown  
Chief, Hypersonic Sciences Branch  
High Speed Systems Division

\*//Signature//



---

James H. Miller  
Principal Advisor  
High Speed Systems Division

This report is published in the interest of scientific and technical information exchange, and its publication does not constitute the Government's approval or disapproval of its ideas or findings.

\*Disseminated copies will show “//Signature//” stamped or typed above the signature blocks.

REPORT DOCUMENTATION PAGE					Form Approved OMB No. 0704-0188	
<p>The public reporting burden for this collection of information is estimated to average 1 hour per response, including the time for reviewing instructions, searching existing data sources, gathering and maintaining the data needed, and completing and reviewing the collection of information. Send comments regarding this burden estimate or any other aspect of this collection of information, including suggestions for reducing this burden, to Department of Defense, Washington Headquarters Services, Directorate for Information Operations and Reports (0704-0188), 1215 Jefferson Davis Highway, Suite 1204, Arlington, VA 22202-4302. Respondents should be aware that notwithstanding any other provision of law, no person shall be subject to any penalty for failing to comply with a collection of information if it does not display a currently valid OMB control number. <b>PLEASE DO NOT RETURN YOUR FORM TO THE ABOVE ADDRESS.</b></p>						
1. REPORT DATE (DD-MM-YY) October 2016		2. REPORT TYPE Interim		3. DATES COVERED (From - To) 01 April 2015 – 13 June 2016		
4. TITLE AND SUBTITLE HYPERSONIC BOUNDARY LAYER TRANSITION EXPERIMENTS - HYPERSONIC INTERNATIONAL FLIGHT RESEARCH EXPERIMENTATION 5 (HIFIRE-5) AND CIRCULAR CONE				5a. CONTRACT NUMBER In-house		
				5b. GRANT NUMBER		
				5c. PROGRAM ELEMENT NUMBER 61102F		
6. AUTHOR(S) Roger Kimmel, Joseph S. Jewell, and Matthew Borg (AFRL/RQHF) Benjamin Hagen (AFRL/RQVX) Brian Lam (Spectral Energies, LLC) Nick Parziale (Stevens Institute of Technology)				5d. PROJECT NUMBER 3002		
				5e. TASK NUMBER		
				5f. WORK UNIT NUMBER Q1FN		
7. PERFORMING ORGANIZATION NAME(S) AND ADDRESS(ES) Hypersonic Sciences Branch (AFRL/RQHF) High Speed Systems Division Aero Validation Branch (AFRL/RQVX) Aerospace Vehicles Division Air Force Research Laboratory, Aerospace Systems Directorate Wright-Patterson Air Force Base, OH 45433-7542 Air Force Materiel Command, United States Air Force				Spectral Energies, LLC 5100 Springfield Street Beavercreek, OH 45431  Stevens Institute of Technology 1 Castle Point Terrace Hoboken, NJ 07030		
9. SPONSORING/MONITORING AGENCY NAME(S) AND ADDRESS(ES)  Air Force Research Laboratory Aerospace Systems Directorate Wright-Patterson Air Force Base, OH 45433-7542 Air Force Materiel Command United States Air Force				10. SPONSORING/MONITORING AGENCY ACRONYM(S) AFRL/RQHF		
				11. SPONSORING/MONITORING AGENCY REPORT NUMBER(S) AFRL-RQ-WP-TR-2017-0098		
12. DISTRIBUTION/AVAILABILITY STATEMENT DISTRIBUTION STATEMENT A: Approved for public release. Distribution is unlimited.						
13. SUPPLEMENTARY NOTES PA Case Number: 88ABW-2016-4800; Clearance Date: 03 October 2016.						
14. ABSTRACT This interim technical report summarizes activity on AFRL 6.1 laboratory task LRIR 15RQCOR102 during fiscal year 2016. The objective of this task is to better understand boundary layer transition in hypersonic flowfields with spanwise nonuniformity. Several advances were made under this task during FY16. Quantitative simultaneous infrared thermography and fluctuating pressure measurements on the HIFIRE-5 configuration were made in a quiet flow wind tunnel. These measurements quantified the growth and structure of traveling cross flow instabilities and provided high-sensitivity thermal imaging for heat transfer measurements of transition. Benchmark experiments on blunt-cone transition carried out in the 1980s have been reanalyzed using modern computational methods. This analysis shows that transition behavior on cones with small bluntness is consistent with second-mode transition behavior, but cones with higher bluntness do exhibit either first or second-mode transition behavior. Finally, multi-point FLDI and high-speed schlieren imaging have been demonstrated for measuring wind tunnel disturbance spectra and convection velocities.						
15. SUBJECT TERMS boundary layer transition, hypersonic, flight test						
16. SECURITY CLASSIFICATION OF:			17. LIMITATION OF ABSTRACT: SAR	18. NUMBER OF PAGES 75	19a. NAME OF RESPONSIBLE PERSON (Monitor) Roger L. Kimmel 19b. TELEPHONE NUMBER (Include Area Code) N/A	
a. REPORT Unclassified	b. ABSTRACT Unclassified	c. THIS PAGE Unclassified				

## Table of Contents

List of Figures .....	ii
List of Tables .....	iv
Acknowledgments.....	v
1. Summary .....	1
2. Simultaneous Infrared and Pressure Measurements of Crossflow Instability Modes for HIFiRE-5 .....	2
2.1. Background and Experimental Overview .....	2
2.2. Tunnel Freestream Characterization .....	8
2.3. Quiet Flow .....	10
2.3.1. Stationary Crossflow Instability .....	10
2.3.2. Traveling Cross Flow Instability .....	15
2.4. Noisy Flow .....	21
2.4.1. Heat Flux.....	21
2.4.2. Pressure Sensors.....	22
2.5. Summary and Conclusions.....	22
3. Boundary Layer Stability Analysis for Stetson’s Mach 6 Blunt Cone Experiments.....	26
3.1. Background .....	26
3.2. Computational Methods .....	27
3.3. Mean Flow Based Transition Correlations.....	28
3.4. Stability Computations.....	33
3.5. Conclusion.....	37
4. Disturbance and Phase Speed Measurements for Shock Tubes and Hypersonic Boundary-Layer Instability .....	40
4.1. Introduction .....	40
4.2. Focusing schlieren Setup.....	40
4.3. Double Focused Laser Differential Interferometry (FLDI) .....	41
4.4. Shock Tube Focusing schlieren and FLDI Results .....	42
4.5. Double FLDI Boundary Layer Results .....	46
5. Development of High-Speed Schlieren System for the New AFRL Mach-6 Ludwig Tube Hypersonic Wind Tunnel .....	49
5.1. Background .....	49
5.2. Experimental Setup .....	49
5.3. Results and Discussion.....	52
List of Acronyms, Abbreviations, Symbols.....	58
References.....	61

## List of Figures

Figure 2-1 Photograph of model.....	4
Figure 2-2 Model surface profiles.....	6
Figure 2-3 Schematic of pressure-sensor locations. The dashed red line denotes approximate field of view of IR camera. ....	7
Figure 2-4 a) Freestream Pitot noise 0–276 kHz. Stars are no IR window, circles are with the IR window installed. b) Freestream Pitot noise 6–276 kHz c) Freestream Pitot spectra.....	9
Figure 2-5 Heat flux contours in quiet flow.....	12
Figure 2-6 Spanwise heat flux profiles and DFTs at $x=305.1$ mm.....	13
Figure 2-7 Heat flux contours for instrumented and uninstrumented shells, $Re=12.3 \times 10^6/m$ .....	13
Figure 2-8 Spanwise heat flux profiles and DFTs at $x=305.1$ mm for instrumented and uninstrumented PEEK shells.....	15
Figure 2-9 Stationary crossflow wavelengths from oil flow and IR.....	16
Figure 2-10 PSDs for sensor 20.....	16
Figure 2-11 PSDs for sensors 2, 8, 14, and 20.....	18
Figure 2-12 Wave angles and phase speeds at sensors 13–15.....	19
Figure 2-13 PSDs for sensors 20 and 43. Solid lines are sensor 20, dashed are sensor 43. ....	20
Figure 2-14 PSDs for sensor 20 on aluminum and PEEK models. Solid lines are PEEK model, dashed are aluminum. ....	21
Figure 2-15 Difference of IR images in noisy flow.....	24
Figure 2-16 PSDs for sensors 2, 8, 14, and 20.....	25
Figure 3-1 Stability results from the $R_N = 0.508$ mm (1%), unit Reynolds number $92.1 \times 10^6/m$ convergence study.....	29
Figure 3-2 Stanton number vs. Reynolds number for the sharp $p_0 = 700$ psi condition, with laminar and turbulent correlations, and laminar computation, for comparison. ....	30
Figure 3-3 Sharp and blunt total enthalpy profiles with boundary layer edge indicated, $p_0 = 1400$ psi.....	30
Figure 3-4 Sharp and blunt unit Reynolds number contours (detail), $p_0 = 1400$ psi. ....	32
Figure 3-5 Nosedip bluntness normalized by swallowing length vs. the transition location ratio. ....	32
Figure 3-6 Nosedip bluntness normalized by swallowing length vs. transition Reynolds number ratio. ....	33
Figure 3-7 Sharp and blunt cone entropy contours (detail), $p_0 = 1400$ psi. ....	34
Figure 3-8 Results as a function of nosetip freestream Reynolds number, where $ReX_{TB} = Re_{unit,\infty}X_{Tr}$ and $Re_{RN} = Re_{unit,\infty}RN$ .....	34
Figure 3-9 LST contours of $-\alpha_i$ for $R_N = 1.016$ mm (2%) for $p_0 = 1400$ psi. ....	36
Figure 3-10 Computed $N$ -factor at experimentally measured transition location.....	36
Figure 3-11 Transition $N$ -factor vs. computed most amplified frequency at transition location..	38
Figure 3-12 Edge Mach number effects: a) Mach number vs. $X_T/X_{SW}$ , b) $N$ -factor vs. Mach number. ....	39
Figure 4-1 Schematic of focusing schlieren imaging optics.....	41
Figure 4-2 Annotated schematic of the FLDI. ....	42
Figure 4-3 AFRL shock tube rendering.....	43
Figure 4-4 AFRL shock tube schematic, with locations indicated for wall pressure transducers 1, 2, and 4, and Pitot transducer 3.....	43

Figure 4-5 Pressure data, including Pitot, from a typical shock tube experiment. The transducer locations are indicated in Figure 4-3.....	43
Figure 4-6 Focusing schlieren images from five successive frames of incident shock propagation for a shock tube experiment. The Pitot probe is visible as a shadow. ....	44
Figure 4-7 4x4 Window .....	45
Figure 4-8 FLDI spectrogram for a shock tube experiment, arbitrary units calculated with the initial fill density. The time scale is in milliseconds.....	45
Figure 4-9 Cross-correlation of double FLDI signals for one shock tube experiment, compared with simultaneous Pitot measurements recorded just downstream.....	47
Figure 4-10 FLDI and focusing schlieren signals (left) and power spectral density (right) compared.....	47
Figure 4-11 Arbitrary logarithmic units of change in density, the spectrum is estimated by the short time Fourier transform. Darker shading indicates larger amplitude. ....	48
Figure 4-12 FLDI Frequency and Time.....	48
Figure 5-1 AFRL Mach-6 Ludwig Tube Hypersonic Wind Tunnel. ....	50
Figure 5-2 Schematic of Pitot rake at the test section.....	50
Figure 5-3 Pressure time histories at nozzle entrance, nozzle exit, and Pitot rake. ....	51
Figure 5-4 Mach number determination for the 90 psi run.....	51
Figure 5-5 Movement of the starting shock for the 90 psi run. ....	52
Figure 5-6 Sample frames during the start-up process for the 90 psi run.....	53
Figure 5-7 Pressure time history for Pitot sensor 3 (marked with 4 major events) for the 90 psi run. ....	54
Figure 5-8 Schlieren image for the Pitot rake in the vertical orientation.....	54
Figure 5-9 Plot of normalized magnitude over a 2x2 pixel window area over time for the 375 psi run.....	55
Figure 5-10 Power-spectral-density (PSD) analysis on schlieren signals for the 375-psi run.....	56
Figure 5-11 Sample shadowgraph image for the flat plate experiment (at the adiabatic wall temperature). ....	56
Figure 5-12 Shadowgraph image for laminar-turbulent boundary layer transition on the flat plate.....	57
Figure 5-13 PSD analysis on normalized shadowgraph signals for the flat plate experiment. ....	57

## List of Tables

Table 2-1 Instrumentation locations and notation .....	7
Table 3-1 Sample inflow conditions (minimum, maximum, and midpoint Reynolds numbers) computed for each bluntness value.....	27
Table 3-2 Summary of grids generated for the present study, each corresponding to a different sharp or blunt nose tip used by Stetson. <sup>38</sup> .....	28
Table 3-3 Characteristics of most unstable modes for cases where oblique modes dominate .....	35
Table 4-1 Summary of reservoir and edge conditions for shot 2821 in 50% CO <sub>2</sub> , 50% air by mass. For further details on this condition see Jewell and Shepherd.....	48

## **Acknowledgments**

This work was supported by the Air Force Office of Scientific Research under Laboratory Research Initiation Request 15RQCOR102. Prof. Steven Schneider of Purdue University supplied test time in the Purdue Quiet Tunnel Ludwig Tube and provided valuable discussions.



## 1. Summary

This interim technical report summarizes technical activity on AFRL 6.1 laboratory task LRIR 15RQCOR102 during fiscal year 2016. The objective of this task is to better understand boundary layer transition in hypersonic flowfields with spanwise nonuniformity. Several advances were made under this task during FY16. Quantitative simultaneous infrared thermography and fluctuating pressure measurements on the HIFiRE-5 configuration were made in a quiet flow wind tunnel. These measurements quantified the growth and structure of traveling cross flow instabilities and provided high-sensitivity thermal imaging for heat transfer measurements of transition. In preparation for experiments on cones at angle of attack, benchmark experiments on blunt-cone transition carried out in the 1980s have been reanalyzed using modern computational methods. This analysis shows that transition behavior on cones with small bluntness is consistent with second-mode transition behavior, but cones with higher bluntness do exhibit either first or second-mode transition behavior. Finally, multi-point FLDI and high-speed schlieren imaging have been demonstrated for measuring wind tunnel disturbance spectra and convection velocities.

This report is compiled from previously published abstracts and conference papers. Section 2 on HIFiRE-5 stability was previously published as AIAA paper 2016-0354.<sup>1</sup> Section 3 on blunt-cone stability analysis has been accepted for publication in the *AIAA Journal of Spacecraft and Rockets*, and is based on AIAA paper 2016-0598.<sup>2</sup> Section 4 on FLDI measurements was published as AIAA paper 2016-3112,<sup>3</sup> and section 5 on high-speed schlieren has been submitted to the AIAA 2017 Scitech meeting.

## 2. Simultaneous Infrared and Pressure Measurements of Crossflow Instability Modes for HIFiRE-5

### 2.1. Background and Experimental Overview

The crossflow instability can become the dominant path to boundary layer transition for realistic, 3D vehicle configurations. Both stationary and traveling modes are possible. The stationary mode manifests as co-rotating, streamwise vortices, while traveling crossflow wavefronts are inclined relative to the inviscid streamlines.<sup>4</sup> The wave number vector of the most unstable traveling mode has a spanwise component opposite the direction of the crossflow.<sup>5</sup> For incompressible flows, the stationary modes are typically dominant in low noise environments of flight and “quiet” wind tunnels, whereas the traveling modes tend to dominate in conventional tunnels.<sup>6</sup> The stationary mode is thought to be seeded by surface roughness, while the traveling mode is generated by vortical disturbances in the freestream which are entrained in the boundary layer.<sup>7</sup>

Considerable study has been made of crossflow instabilities for incompressible flows.<sup>6-12</sup> It has been established that stationary modes undergo a period of linear growth, saturate nonlinearly, and then develop secondary instabilities that rapidly lead to transition.<sup>6, 10</sup> The majority of historic crossflow research has focused on stationary modes, since this is expected to be the dominant crossflow instability in the low- noise flight environment. However, the role and importance of traveling modes, possible interactions with stationary crossflow, and possible nonlinear self-interaction have not been well documented.

Recently, interest in the crossflow instability at supersonic and hypersonic flows has grown. Saric<sup>6,13</sup> suggested that the same basic behavior observed for incompressible flows should also be expected for compressible flows. King<sup>14</sup> measured crossflow-dominated transition on a 5 degree sharp circular cone at Mach 3.5 in both quiet and noisy flow. However, these experiments focused primarily on crossflow transition location rather than a detailed study of the instabilities themselves. He noted that the effect of freestream turbulence on transition location decreased substantially with increasing crossflow. Recent experiments by Beeler et al.<sup>15</sup> confirmed the presence of stationary crossflow vortices on a wedge-cone model in a Mach 3.5 quiet tunnel. Future experiments will focus on determining if traveling modes are also present. Poggie and Kimmel<sup>16</sup> measured traveling crossflow wave properties with hot films in a Mach 8 conventional tunnel using a 2:1 elliptic cone, but did not find good agreement with complementary computations. They suggested that the poor agreement was due to the limitations of the computations. Malik et al.<sup>4</sup> reported experimental and computational results from a crossflow-dominated supersonic swept-wing flight test for Mach numbers from four to five. The flight transition locations correlated with stationary crossflow  $N$ -factors of 7.0–12.4 and traveling crossflow  $N$ -factors of 7.6–14.1. Choudhari et al.<sup>17</sup> described stability computations for flight and wind tunnel conditions for HIFiRE-5. They found strong stationary and traveling crossflow growth over large portions of the vehicle acreage. They also investigated the effect of flow non-parallelism and integration path on  $N$ -factors for both types of crossflow instability. Swanson and Schneider<sup>18</sup> detected stationary cross- flow vortices with temperature sensitive paint at Mach 6 with both quiet and conventional freestream noise levels. Craig and Saric<sup>19</sup> made hotwire measurements of stationary crossflow waves on an inclined circular cone in a quiet Mach 6 freestream. They found great similarities to low-speed crossflow in structure, growth patterns,

and a secondary instability. Ward et al.<sup>20</sup> also made measurements of crossflow instabilities on an inclined circular cone in a quiet Mach 6 freestream. Temperature-sensitive paint confirmed the presence of stationary crossflow vortices. Pressure sensors detected the traveling crossflow instability, as well as a high-frequency instability that may be a secondary instability of the stationary crossflow vortices. Dinzl and Candler<sup>21</sup> report direct numerical simulation computations of the flowfield for the HIFiRE-5 model. Due to the sensitivity of this flowfield to the crossflow instability, great care needed to be taken to ensure that the mean flow was accurately computed without seeding crossflow vortices into the base flow. Previous testing and analysis for elliptic cones demonstrated that a 2:1 elliptic cone would generate significant crossflow instability at the expected flight conditions for HIFiRE-5.<sup>22-24</sup> In order to exploit this prior body of work and expedite configuration development, the 2:1 elliptical geometry was selected as the test article.

Previous ground tests on the HIFiRE-5 geometry revealed a number of interesting features as well as several limitations of both the experimental methods and model.<sup>25, 26</sup> For noisy and quiet flows, stationary crossflow vortices were readily detected with oil flow visualization. However, temperature sensitive paint (TSP) did not show any vortices in noisy flow, and only revealed vortices in quiet flow for a subset of the Reynolds numbers for which they were detected with the oil flow.<sup>27</sup> In an attempt to study traveling crossflow waves in both conventional “noisy” and quiet freestream environments, previous experiments were performed on the HIFiRE-5 elliptic cone geometry in Purdue University’s BAM6QT and Texas A&M University’s ACE hypersonic wind tunnels. Traveling crossflow waves and transition were clearly measured in the quiet freestream environment. Since the traveling mode is conventionally thought to dominate crossflow transition in noisy environments, traveling waves were also expected in noisy flow. However, there was no evidence of traveling crossflow waves with a noisy freestream, even though the spectra of the surface pressure signals showed an expected progression from laminar to turbulent as the Reynolds number was increased.<sup>26</sup> It was thought that perhaps the very noisy freestream environment of the BAM6QT when run noisy caused transition apart from the traveling crossflow mode. Thus, the model was also tested in ACE at similar freestream temperatures and pressures, but with lower noise levels. Again, even though transition was observed, the traveling crossflow instability was not.<sup>25</sup> The model used in these past experiments was not originally designed for surface instrumentation. Thus, pressure sensors were mounted flush with the model surface in only one grouping near the back of the model with no feasible way of adding more instrumentation farther forward on the model. The results of these experiments motivate the current work.

In an attempt to obviate some of the experimental difficulties and answer some of the outstanding questions raised by the previous work, a new HIFiRE-5 model was designed and used for the work presented in this paper. The new model design satisfied two primary objectives. First, the new model accommodated IR heating measurements. The IR method alleviates roughness and steps induced by temperature-sensitive paint, and it was hoped the method might provide higher heat-transfer sensitivity over TSP. TSP could only image crossflow at relatively high Reynolds numbers. Under noisy flow, the boundary layer transitioned at Reynolds numbers well below the TSP detection limit. It was hoped that the more sensitive IR method would provide quantitative heat transfer measurements of stationary crossflow under noisy conditions, to support the qualitative oil-flow imaging. Secondly, the new model contained streamwise-distributed arrays of pressure sensors well upstream of the one measuring station

available on the previous model. The streamwise-distributed sensors permit quantitative measurements of the evolution of crossflow instabilities at a variety of  $x$ -locations and unit Reynolds numbers. It was hoped that both the IR and distributed pressure measurements would illuminate the evolution of instabilities leading to transition under noisy and quiet flow. The new model, shown in Figure 2-1, maintains the same outer mold line as the previous model. It is a 38.1% scale model of the flight vehicle, is 328.1 mm long, and has a base semi-major axis of 82.3 mm. The half-angle of the elliptic cone in the minor axis plane is  $7.00^\circ$ , and  $13.80^\circ$  in the major axis ( $x$ - $y$  plane).

The nosetip cross-section in the minor axis plane is a 0.95 mm radius circular arc, tangent to the cone ray describing the minor axis, and retains a 2:1 elliptical cross-section to the tip.

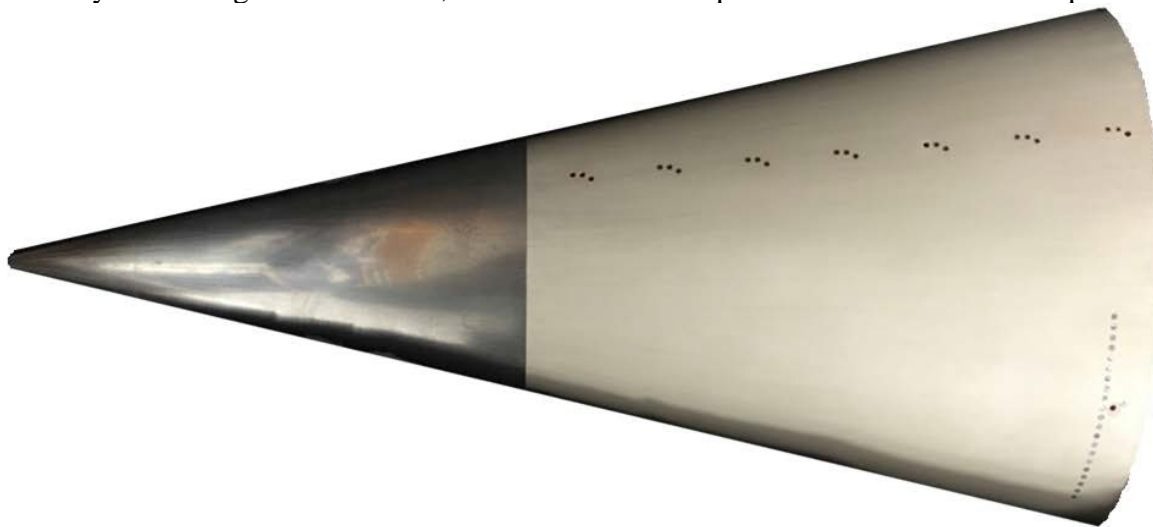


**Figure 2-1 Photograph of model**

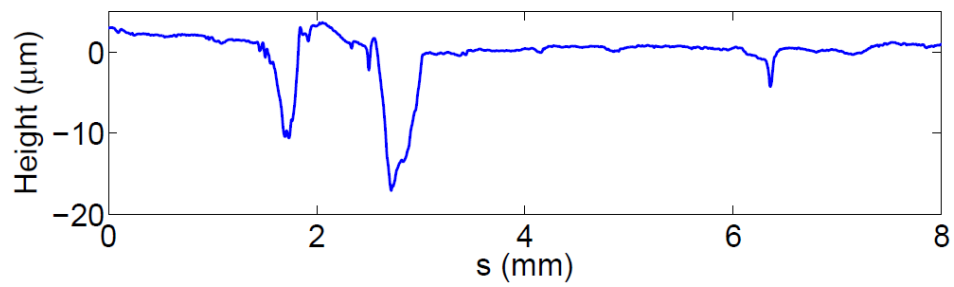
The model is made of solid 15-5PH H-1100 stainless steel from the nose to  $x=150.3$  mm. The RMS surface finish of the steel is  $0.4\text{ }\mu\text{m}$  ( $16\mu\text{in}$ ). Downstream of  $x=150.3$  mm, the model is a shell made of unfilled PEEK, a high emissivity, high temperature plastic. The surface-normal thickness of the PEEK is 10.0 mm, except along the leading edges where it is thicker. The use of a shell, rather than a solid model, facilitates the installation of surface-flush pressure sensors in many locations and much farther forward than in the previous model. The instrumented shell has forty-four holes for instrumentation. Since the shell has a high emissivity and low thermal conductivity, it is also well-suited for infrared (IR) thermography. The use of IR thermography was inspired by previous successes in imaging crossflow vortices in hypersonic wind tunnels.<sup>28-30</sup>

Due to poor machining practice, the model manufacturer overcut portions of the stainless steel nose. The overcut was backfilled with solder and then re-machined. Unfortunately, this resulted in some portions of the nose with discrete roughness patches and/or steps. On the top, instrumented side of the model near the steel/PEEK junction ( $x \approx 150$  mm), there are several divots near the leading edge that are  $30\text{--}40\text{ }\mu\text{m}$  deep and about 0.9 mm wide. Farther upstream on the leading edge, at  $x \approx 50$  mm, there are several divots that are  $10\text{--}15\text{ }\mu\text{m}$  deep and about 0.5 mm wide. Sample surface-profile traces of a few of the divots can be seen in Figure 2-2. The bottom

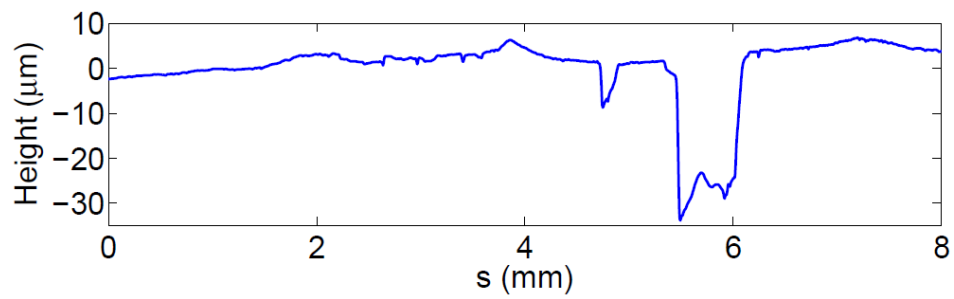
half of the model does not have such divots on the leading edge. The impact of this roughness near the leading edge is unknown. However, the data presented in this paper exhibit some top/bottom asymmetry that may be due to this roughness.

The experiments described in this paper aimed to test the new model in freestream conditions that were identical to the previous experiments. The model was always held at 0 degrees in pitch and yaw. All data were obtained in the BAM6QT at Purdue University. In an attempt to determine the effect of freestream noise on crossflow instability modes, the current experiments were performed with both quiet and noisy freestreams. Quiet flow was realized for freestream Reynolds numbers ( $Re$ ) up to  $13.1 \times 10^6/m$ . The Purdue tunnel achieves quiet noise levels by maintaining a laminar boundary layer on the tunnel walls.<sup>31</sup> A laminar boundary layer is maintained by removing the nozzle boundary layer just upstream of the throat via a bleed suction system. A new, laminar boundary layer begins near the nozzle throat. The boundary layer is kept laminar by maintaining a highly-polished nozzle wall to reduce roughness effects. The divergence of the nozzle is very gradual to mitigate the centrifugal Görtler instability on the tunnel wall.

For the current experiments, twenty-two pressure sensors were used for some of the runs, though one sensor broke part way through the experimental campaign. Table 1 lists the locations of the sensors relative to the nosetip. Figure 2-3 shows a sketch of the model and sensor locations. Seven groups of three sensors were located 25.4 mm apart along a line inclined  $5^\circ$  with respect to the centerline. This is the approximate angle between an inviscid streamline and the centerline.<sup>32</sup> The middle sensor of the most downstream group of sensors (sensor 20) has coordinates identical to one of the sensors on the previous model. In these experiments, sensor 43 was located at the same coordinates as sensor 20, but reflected across the model centerline. Sensor holes that did not have sensors installed were plugged with nylon rods that were flush with the model surface.



(a) Leading edge near  $x = 50$  mm



(b) Leading edge near  $x = 150$  mm

**Figure 2-2 Model surface profiles**

**Table 2-1 Instrumentation locations and notation**

Sensor	$x$ (mm)	$y$ (mm)	Sensor	$x$ (mm)	$y$ (mm)
1	163.6	26.5	12	244.8	32.0
2	166.4	26.5	13	264.8	35.3
3	168.9	25.3	14	267.6	35.3
4	188.9	28.7	15	270.1	34.2
5	191.7	28.7	16	290.1	37.6
6	194.2	27.5	17	292.9	37.6
7	214.2	30.9	18	295.4	36.4
8	217.0	30.9	19	315.4	39.8
9	219.5	29.8	20	318.2	39.8
10	239.5	33.1	21	320.7	38.6
11	242.3	33.1	43	318.2	-39.8

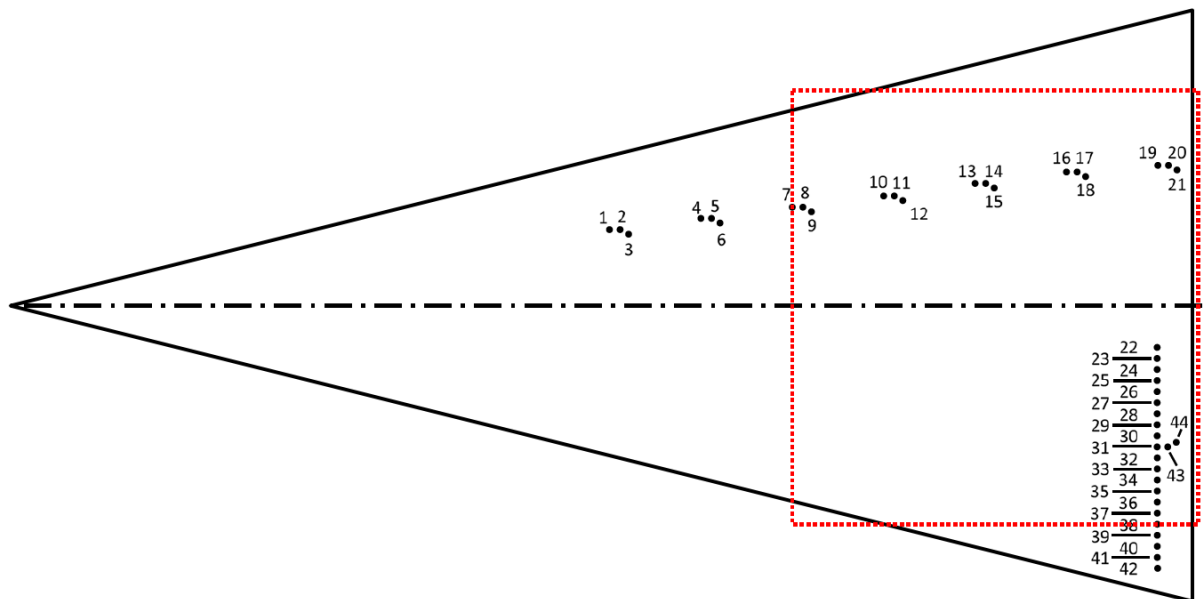


**Figure 2-3 Schematic of pressure-sensor locations. The dashed red line denotes approximate field of view of IR camera.**

Kulite XCQ-062-15A and XCE-062-15A pressure transducers with A screens were mounted flush with the model surface to detect traveling crossflow waves. The Kulite sensors are mechanically stopped at about 100 kPa so that they can survive exposure to high pressures but still maintain the sensitivity of a 100 kPa full-scale sensor. These sensors typically have flat frequency response up to about 30–40% of their roughly 270–285 kHz resonant frequency.<sup>33</sup>

In addition to the pressure transducers, the PEEK shell of the model was imaged with a Xenics Onca IR camera. The camera is a mid-wave, 14-bit camera which is sensitive to IR radiation from 3.7–4.8  $\mu\text{m}$ . The sensing array is 640 x 512 pixels. Images were acquired at about 80 Hz.

Using a subroutine called QCALC, IR data were reduced to heat flux by solving the transient one-dimensional heat equation on a pixel-by-pixel basis. QCALC uses second order Euler-explicit finite differences to solve for the temperature distribution through the model. Heat flux is calculated from a second-order approximation of the derivative of the temperature profile at the surface.<sup>34</sup> The measured surface temperature was used as one boundary condition. An adiabatic backface temperature was used as the other boundary condition. The thermal conductivity, density, and specific heat of PEEK were obtained from the manufacturer and are 0.29 W/(m·K), 1300 kg/m<sup>3</sup>, and 1026 J/(kg·K), respectively. The size of the model precluded an accurate measurement of its emissivity. A skilled researcher estimated the emissivity to be 0.88–0.93, depending on how diffuse the reflection from the model is. A future project is to procure a smaller sample of PEEK for a much more accurate determination of the actual model emissivity. For the results presented here, the emissivity was taken to be 0.91. A full uncertainty analysis has not yet been completed for the IR measurements on the PEEK model, but is planned for the future.

## 2.2. Tunnel Freestream Characterization

In order to more fully understand the response of the model's boundary layer to the freestream disturbance field, attendant freestream Pitot surveys were completed on the tunnel centerline for the Reynolds numbers tested during the experiments. The Pitot sensor was positioned on the tunnel centerline at the approximate location of the model nosetip.

In order to use the IR camera for these experiments, a new IR-clear window was designed and used in the wind tunnel. Due to affordability constraints, the window is flat, rather than conformal to the axisymmetric nozzle contour as the typical Plexiglas windows are. The freestream Pitot surveys are also used to determine if the IR window has any large upstream influence on the tunnel flow quality. There was some concern that the cavity over the window would cause a separation or other disturbances to feed upstream, contaminating the core flow. Figure 2-4a shows noise levels for quiet runs without the IR window (stars) and with the IR window (circles). The noise level is defined as the RMS Pitot pressure normalized by the mean Pitot pressure. The Pitot RMS pressure was found by removing the mean, computing the PSD, and then integrating the PSD from 0–276 kHz. These integration bounds ensure that the Kulite resonance at 295 kHz does not contribute to the reported RMS Pitot pressure. The various colors correspond to different individual tunnel runs. For any given run, the noise level is seen to increase somewhat as the Reynolds number drops. This corresponds to increased time into the run. Nevertheless, the noise levels for quiet flow are always less than 0.03%. Most of the noise increase was due to higher power in the 0–6 kHz band, much lower than the frequencies of expected traveling crossflow waves. Noise levels with the PSDs integrated from 6–276 kHz are shown in Figure 2-4b. For the runs at higher freestream Reynolds numbers, the noise levels show little variation as  $Re$  drops. The runs at lower freestream Reynolds numbers still show significant growth as  $Re$  drops. This is thought to be due to the acoustic noise levels falling below the electronic noise floor of the pressure sensors. For these lower  $Re$  runs, the actual RMS does not change throughout the runs. This would be expected if the electronic noise were greater than the pressure noise. The normalizing pressure, however, continues to decrease throughout the runs, giving rise to the appearance of increased normalized freestream noise. No appreciable or systematic effect of the window is observed at the location of the Pitot sensor.



PSDs of the Pitot signal are shown in Figure 2-4c for select Reynolds numbers with quiet flow. Disturbances are evident between 25 and 50 kHz. However, there is no systematic trend of the peak power with Reynolds number. It is unclear if these disturbances are due to an aerodynamic effect or electronic noise. No electronic noise signal was recorded during these experiments. These spectra look qualitatively similar to previous Pitot surveys in the BAM6QT (Figure 3.3 of Reference 35). So, whatever the cause of the disturbances, they were not unique to these experiments. It is noteworthy that the frequencies of the observed traveling crossflow instability (discussed in section 2.3.2) typically falls between 40 and 60 kHz.

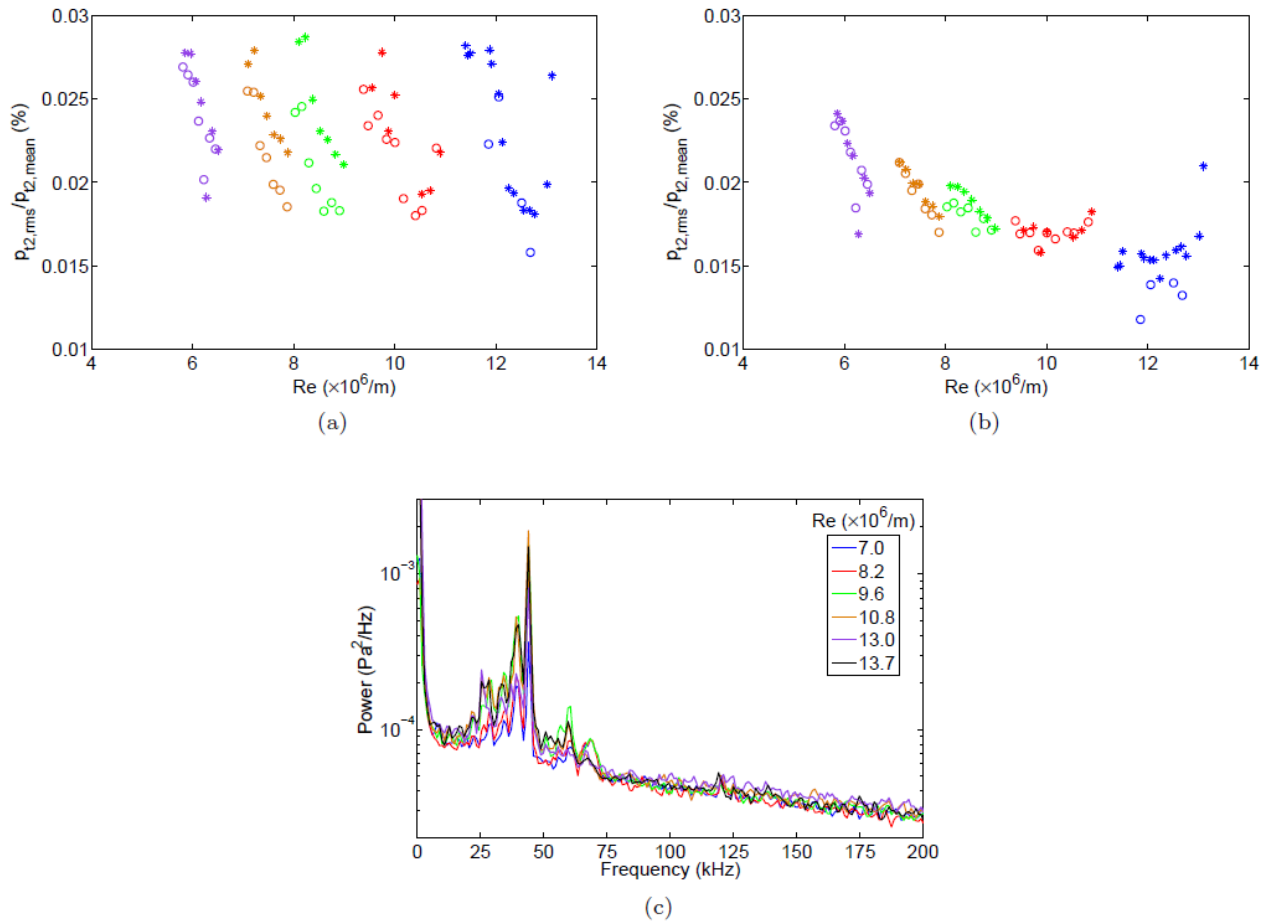


**Figure 2-4 a) Freestream Pitot noise 0–276 kHz. Stars are no IR window, circles are with the IR window installed. b) Freestream Pitot noise 6–276 kHz c) Freestream Pitot spectra**

## 2.3. Quiet Flow

### 2.3.1. Stationary Crossflow Instability

With the model in the tunnel, a freestream Reynolds number sweep was performed for  $Re=5.8\text{--}13.0\times 10^6/\text{m}$ . Heat flux contours for select Reynolds numbers are shown in Figure 2-5. It was not possible to image the entire PEEK shell at once. The PEEK shell extends approximately 66 mm upstream of the upstream extent of the images presented. The dashed red line in Figure 2-3 shows the approximate field of view of the IR camera. The heat flux scales in Figure 2-5 change with each Reynolds number and are selected to best highlight the salient features.

In each image, streaks that are oriented in nearly the streamwise direction are apparent. These streaks are due to stationary crossflow vortices. As the freestream Reynolds number increases, the maximum heat flux along a given streak increases as does the upstream extent of the higher heat flux. Spectra from the Kulites embedded in the model surface appear turbulent when the amplitudes of the streaks on top of them reach relatively high values. Thus, the increased heat flux with increased  $Re$  is likely reflective of both the higher Reynolds number flows as well as transition along the stationary crossflow vortices.

There is some apparent top/bottom asymmetry in the pattern of the vortices. The primary reason for this discrepancy may be a small patch of noticeable, discrete roughness along the leading edge on the sensor side of the model near  $x=50$  mm, in the stainless steel portion of the model.

Of note are the higher heat flux regions surrounding the pressure sensors for  $Re=8.2$  and  $9.3\times 10^6/\text{m}$ . It was discovered that the powered pressure sensors serve to heat the model appreciably. Such localized heating is especially evident for the lower Reynolds number cases where the range of heat flux displayed is considerably less than for higher Reynolds numbers. In order to mitigate this heating as much as possible, the sensors were powered off immediately following a run. They were not turned back on until just before the next run.

In order to determine spanwise wavelengths from the IR data, a spanwise cut was taken at  $x=305.1$  mm for each Reynolds number. It should be noted that the lens used for these experiments introduced significant distortion into the IR images that has not yet been corrected. The “spanwise” cuts are actually the intensities at one horizontal pixel location. Thus, the cuts are not entirely spanwise and sweep through a finite range of streamwise stations. Future analysis will seek to correct for this distortion. These spanwise cuts are shown in Figure 2-6a. Each spanwise cut is artificially offset in order to unambiguously see the results for each Reynolds number. For each spanwise cut, the mean was removed and some smoothing was employed. DFTs were calculated for each spanwise cut for both the bottom (negative  $y$  values) and top (positive  $y$  values) halves of the model. These are shown in Figure 2-6b and Figure 2-6c, respectively.

As can be seen from the spanwise cuts of intensity and the DFTs, the stationary crossflow vortices are present for all Reynolds numbers, with the largest amplitudes occurring for  $Re=11.3\text{--}13.0\times 10^6/\text{m}$ . The streak amplitudes are roughly consistent with those measured by Muñoz et al.<sup>29</sup> on an inclined circular cone at similar freestream conditions using an IR camera. At these Reynolds numbers, most of the streaks at  $x=305.1$  mm are turbulent. Evidently, the

vortices persist well downstream of transition. On the bottom side of the model, two wavelengths are prominent, approximately 3.0 and 4.2 mm. The top side of the model shows spectral peaks at approximately 2.8–3.0 and 3.5–4.5 mm for  $Re=10.3\text{--}13.0\times 10^6/\text{m}$ . Additional peaks are also present, depending on the Reynolds number, as well as more broadband content. There is a clear top/bottom asymmetry. Since stationary crossflow vortices are seeded by surface roughness, this asymmetry suggests that the surface roughness on the top side of the model is different than on the bottom side.

In order to assess whether the pressure transducers were responsible for the asymmetry in the stationary crossflow vortices, the instrumented PEEK shell was removed and an uninstrumented PEEK shell was tested at  $Re=12.3\times 10^6/\text{m}$ . IR images for the instrumented and uninstrumented shells are shown in Figure 2-7a and Figure 2-7b, respectively. A very similar stationary crossflow vortex pattern is present on both shells. Some top/bottom asymmetry is still evident.

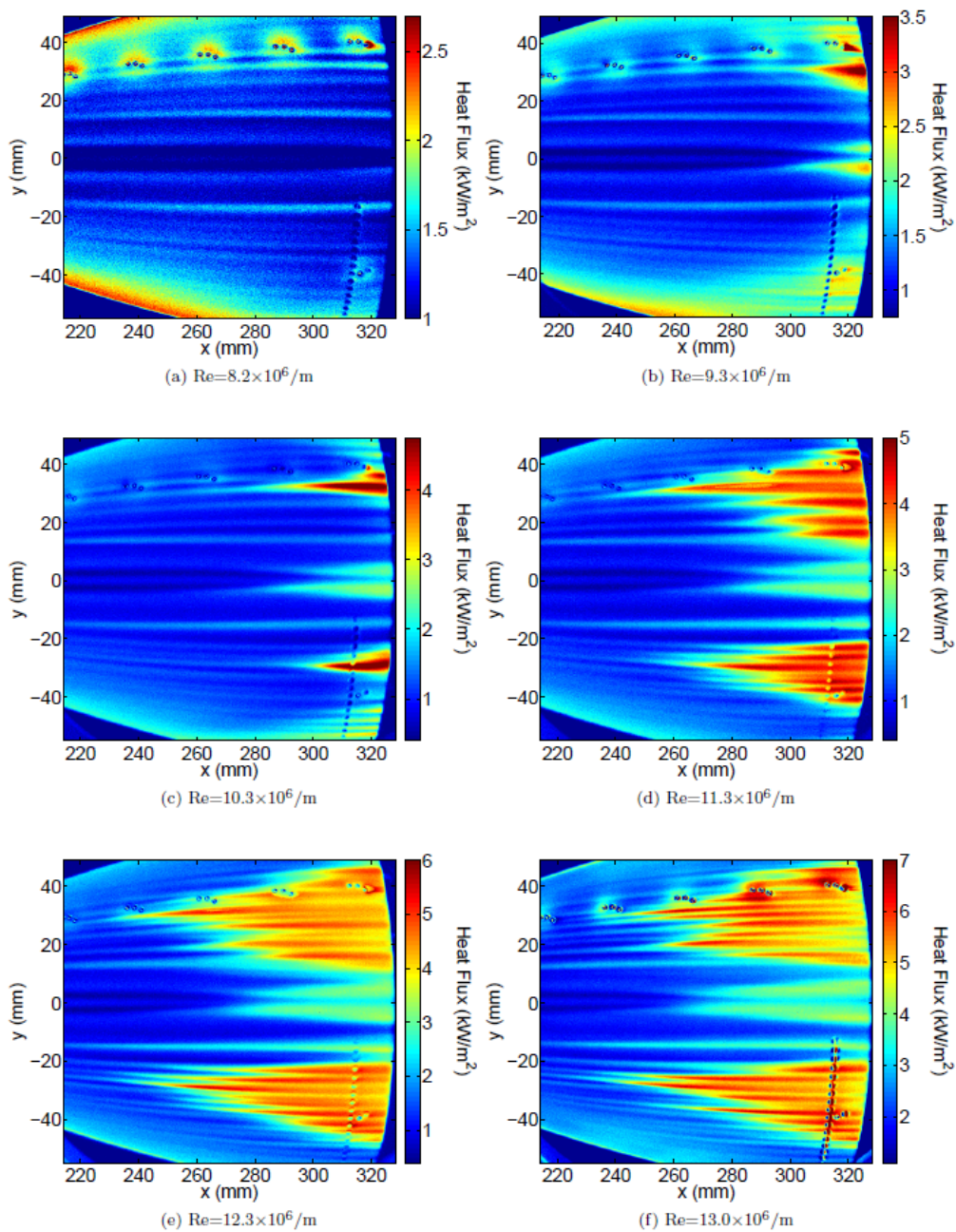


**Figure 2-5 Heat flux contours in quiet flow**

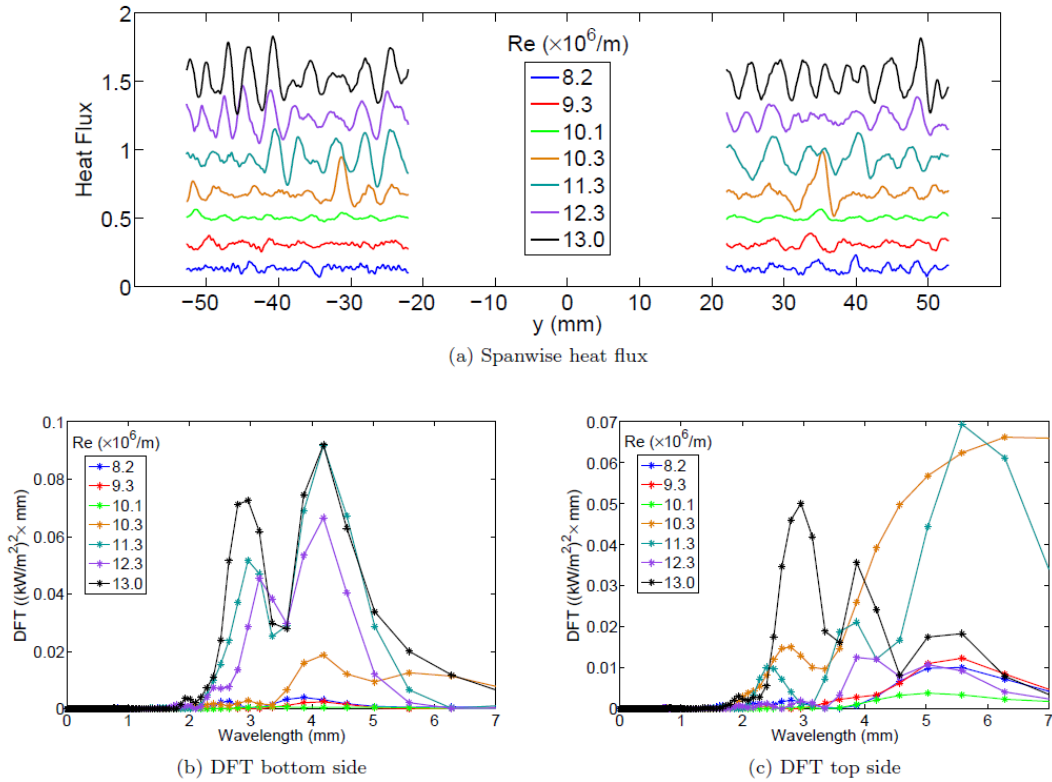


**Figure 2-6 Spanwise heat flux profiles and DFTs at  $x=305.1$  mm**

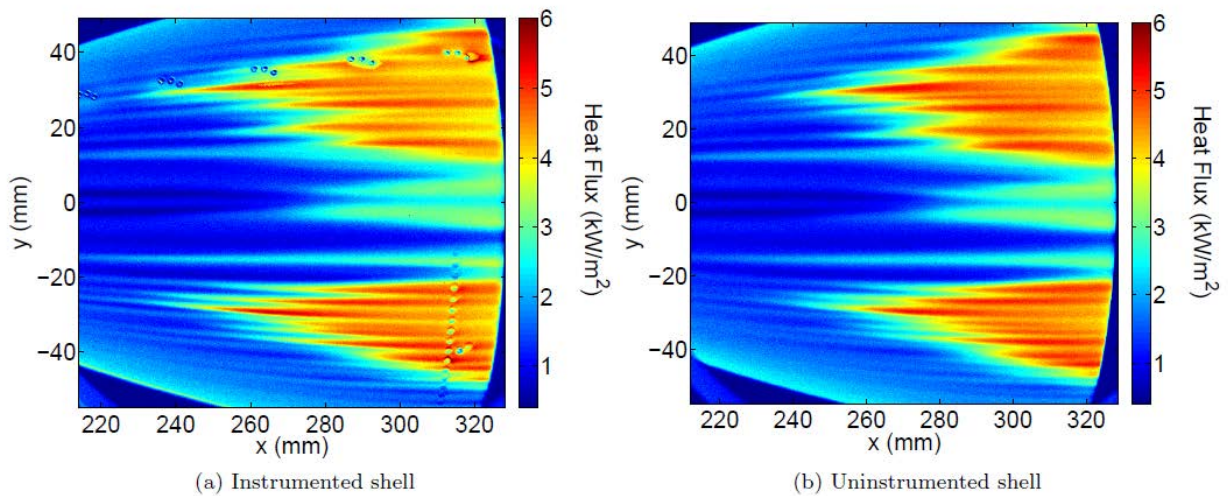


**Figure 2-7 Heat flux contours for instrumented and uninstrumented shells,  $Re=12.3 \times 10^6/m$**

Figure 2-8a shows spanwise cuts at  $x=305.1$  mm for both the instrumented and uninstrumented shells. DFTs for both the top and bottom sides of each shell are also shown in Figure 2-8b and Figure 2-8c, respectively.

The spanwise cuts for the bottom half of the model (the left side of Figure 2-8a) are nearly the same for both shells. The DFTs for the bottom half of the model show distinct peaks at 3.0 and 4.2 mm. The peaks for the instrumented shell have slightly higher amplitudes than for the uninstrumented model. Nevertheless, the stationary crossflow vortex patterns show good agreement for the two shells on the bottom half of the model.

The agreement between the shells is not as good for the top half of the model. The spanwise cuts for the top halves appear to have very similar patterns, but are offset slightly in space. The DFTs have broad peaks centered around 4.5 mm. Lower-amplitude peaks are also visible at 2.4 and 3.0 mm.

Due to the excellent agreement in the stationary crossflow vortex pattern on the lower half of the model, it appears that the vortex pattern there is dominated by surface roughness on the steel nose. The moderate agreement on top half of the model suggests that the vortex pattern is dominated by roughness on the nose, but is modulated to some degree by the pressure transducers in the instrumented model.

Previous work on the solid aluminum model with oil flow visualization was instructive in determining the wavelength of stationary crossflow vortices.<sup>27</sup> Figure 2-9 shows DFTs at  $x=296.3$  mm from the oil flow visualization on the earlier model and from the IR on the lower half of the PEEK model for  $Re=12.1$  and  $12.3 \times 10^6/m$ , respectively. The oil flow was not a calibrated method. Therefore, the DFT derived from oil flow images was semi-quantitative and used only to derive crossflow wavelengths. In order to compare the oil flow to the IR DFT, the oil flow DFT was scaled to approximately match that from the IR. Excellent agreement is seen in the peak wavelengths. This suggests that the distributed surface roughness on the aluminum model and the bottom half of the PEEK model are similar, and that this flow condition naturally selects the observed wavelengths.

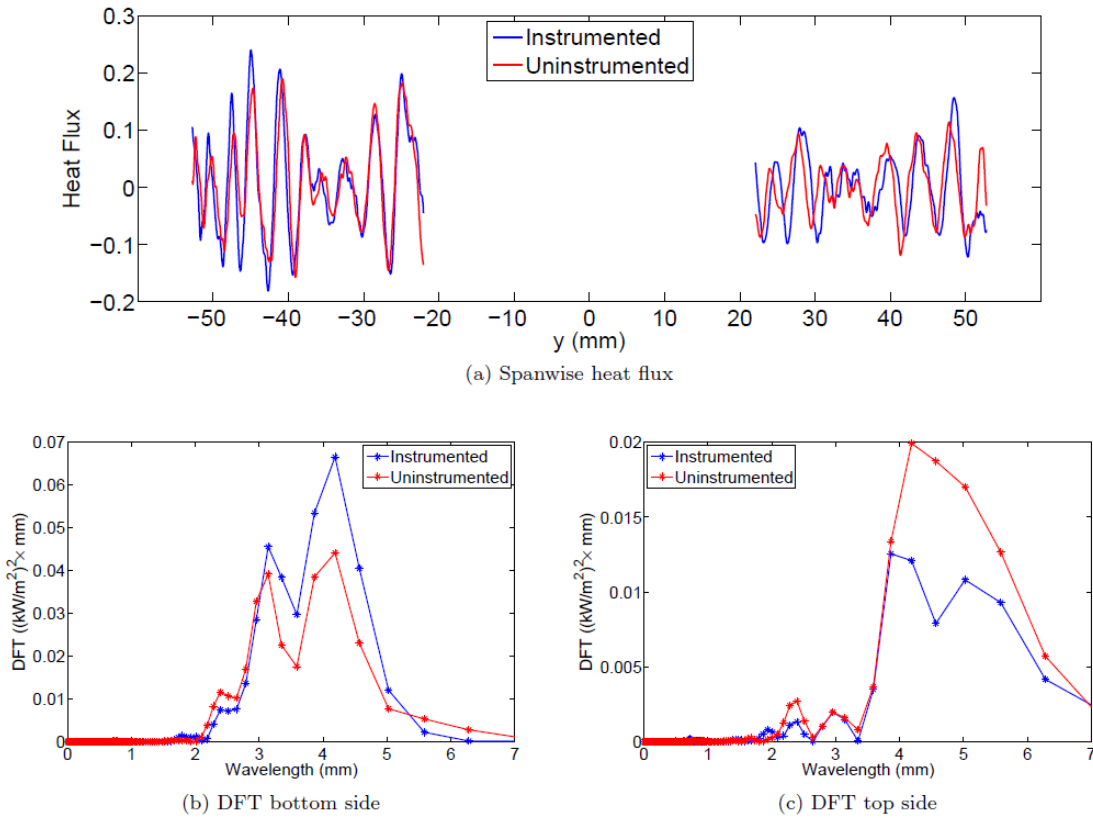


**Figure 2-8 Spanwise heat flux profiles and DFTs at  $x=305.1$  mm for instrumented and uninstrumented PEEK shells**

### 2.3.2. Traveling Cross Flow Instability

Pressure sensors mounted flush with the model surface were used to detect the traveling crossflow instability. Traveling crossflow was first examined by measuring the evolution of instabilities at a fixed  $x$ -location as unit Reynolds number varied. Next, streamwise-distributed transducers demonstrated the spatial evolution of the traveling crossflow at several unit Reynolds numbers. Transducer arrays provided quantitative wave-angle and phase-velocity measurements.

Figure 2-10 shows PSDs for sensor 20 for freestream Reynolds numbers ranging from  $6.6$  to  $12.8 \times 10^6/m$ . In each case, the pressure signal is normalized by the freestream static pressure. For  $Re=6.6 \times 10^6/m$ , no distinct peaks are observed. As the Reynolds number is increased, a peak centered on about  $45$  kHz is observed to grow. This peak is attributed to the traveling crossflow instability. For  $Re>8.9 \times 10^6/m$ , spectral broadening is observed, indicating the onset of transition. For  $Re=11.2 \times 10^6/m$ , the boundary layer is nearly turbulent. As  $Re$  increases further, a fully turbulent boundary layer is indicated.

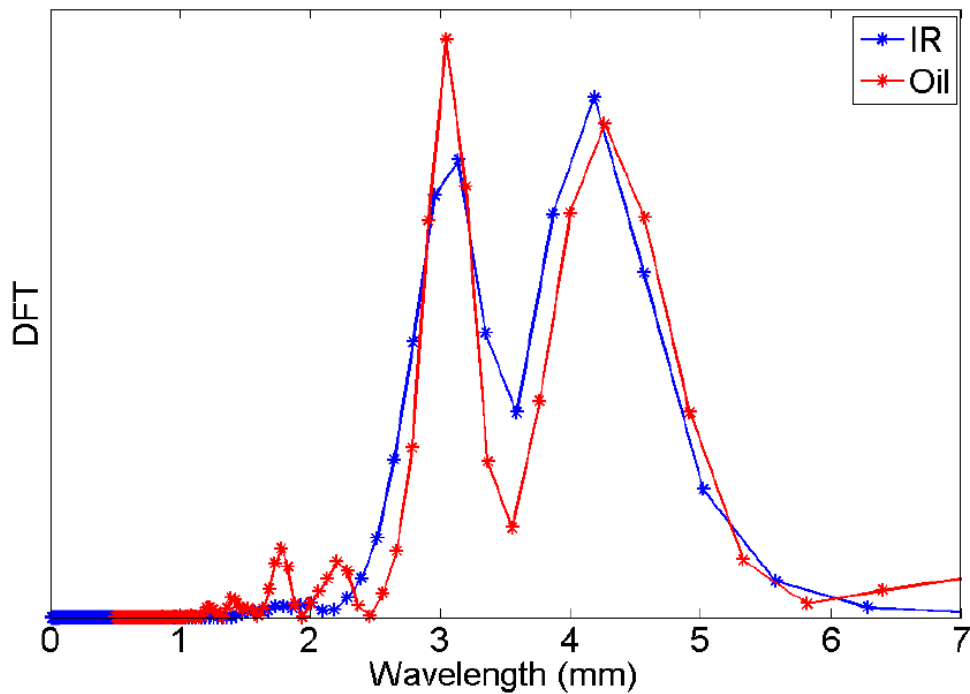


**Figure 2-9 Stationary crossflow wavelengths from oil flow and IR**

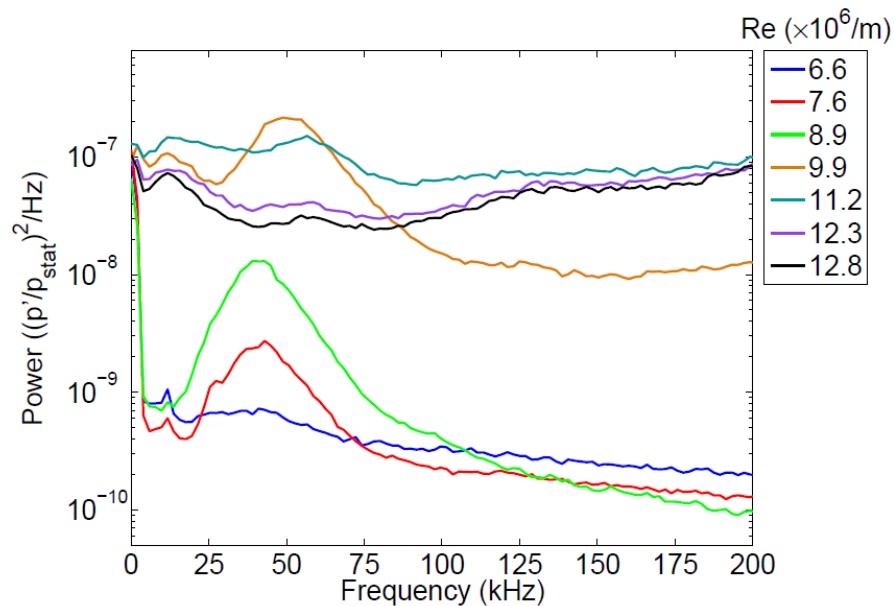


**Figure 2-10 PSDs for sensor 20**

Figure 2-11 presents PSDs for sensors 2, 8, 14, and 20 for freestream Reynolds numbers of 6.6, 8.9, 9.9, and 12.8  $\times 10^6/\text{m}$ . The streamwise location on the model increases with sensor number. For  $Re=6.6 \times 10^6/\text{m}$ , no traveling crossflow is observed for any sensors. As  $Re$  is increased to  $8.9 \times 10^6/\text{m}$ , peaks in the PSD due to traveling crossflow are present for sensors 14 and 20. The



spectra for these sensors reflect a perturbed laminar boundary layer. Since the power levels for higher frequencies relax back to the unperturbed spectra, the traveling crossflow at this Reynolds number is assumed to be growing linearly. When  $Re$  is further increased to  $9.9 \times 10^6/m$ , traveling crossflow is now seen for sensors 8, 14, and 20. Traveling crossflow at sensor 8 appears to be growing linearly. At sensor 14, significant spectral broadening is observed, indicating the onset of breakdown. The boundary layer at sensor 20 appears to be almost turbulent. At the highest Reynolds number,  $12.8 \times 10^6/m$ , there may be a small spectral peak for sensor 2, but it is not obvious that traveling crossflow there is of measurable amplitude. Traveling crossflow is still present at sensor 8, with significant broadening of the spectrum. The boundary layer at sensor 14 is nearly turbulent, and is fully turbulent at sensor 20.

The spectra in Figure 2-11 tell a consistent story. For a given sensor, traveling crossflow first grows linearly. As  $Re$  is increased, transition onset is evidenced by nonlinear spectral broadening. For still larger Reynolds numbers, the boundary layer becomes fully turbulent. This progression occurs farther upstream with each increase in freestream Reynolds number. For this data set, the spectra of the signals from the pressure sensors and the IR images can be compared in a limited, qualitative sense. The spectra are observed to broaden before the streaks in the vicinity of those sensors undergo the rapid streamwise increase in heat flux. When a given sensor is located in the region of increased heat flux, the spectra there appear nearly or fully turbulent. It appears that the boundary layer begins to transition prior to any indication in the heat flux.

The pressure sensors were installed in groups of three in the model so that wave angles and phase speeds of the traveling crossflow instability could be calculated. Unfortunately, such wave properties could only be calculated for one sensor group for these particular experiments. As seen in Figure 2-11, sensor group 1-2-3 did not detect traveling crossflow waves for even the highest quiet freestream Reynolds number that was achievable. Sensor groups 4-5-6, 10-11-12, and 16-17-18 were all conditioned with new electronics that proved to have prohibitively high levels of electronic noise. The electronic noise was such that the signatures of the traveling crossflow waves were largely obscured, and not suitable for the calculation of wave properties. Due to a limited number of oscilloscopes, the sensors in sensor group 7-8-9 were each connected to different oscilloscopes. Exact synchronization of all three oscilloscopes was not achieved. This resulted in relative phase shifts among the signals from sensors 7, 8, and 9 that were not related to the propagation of traveling crossflow waves. There is no way to correct for these synchronization errors. Sensor 21 broke early into the test campaign. Thus wave properties cannot be determined from sensor group 19-20-21. This leaves only sensor group 13-14-15 for the determination of traveling crossflow wave properties.

PSDs for sensor 14, as well as wave angles and phase speeds for traveling crossflow waves at sensor group 13-14-15 are shown in Figure 2-12 for freestream Reynolds numbers ranging from 8.4 to  $9.9 \times 10^6/m$ . These quantities were calculated using the method described in Reference 26. The wave angles for the peak frequency near 50 kHz are between 70 and 80° for  $Re=8.4$ – $9.1 \times 10^6/m$ . For larger Reynolds numbers, the wave angles diverge sharply from what was observed for lower Reynolds numbers. Phase speeds were found to be between 200 and 250 m/s for 50 kHz traveling crossflow waves for  $Re=8.4$ – $9.1 \times 10^6/m$ . Calculated phase speeds also diverge sharply for higher Reynolds numbers. These values and trends are very similar to what was measured on the previous model at a location approximately 50.8 mm downstream of sensor

group 13-14-15. <sup>26</sup> The divergence at higher Reynolds numbers is attributed to nonlinear effects and transition onset.

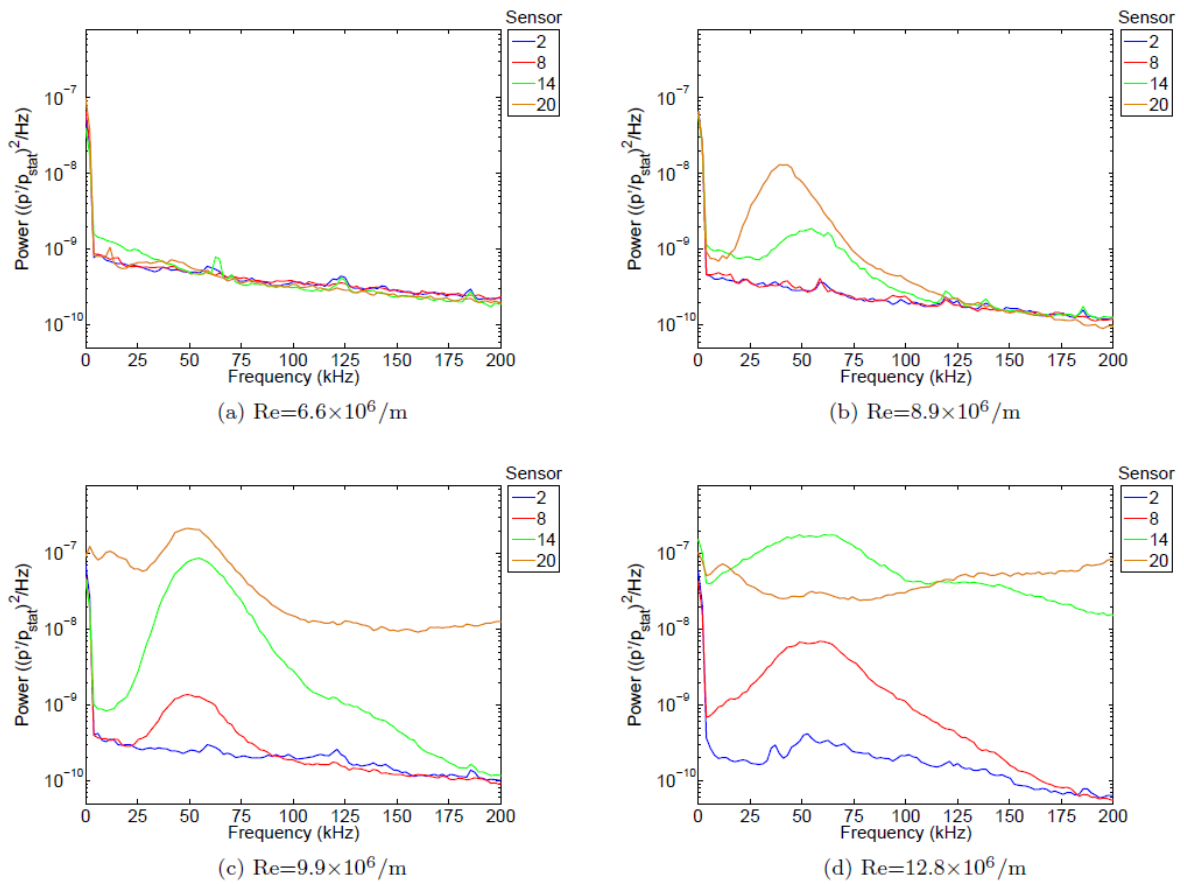


**Figure 2-11 PSDs for sensors 2, 8, 14, and 20**

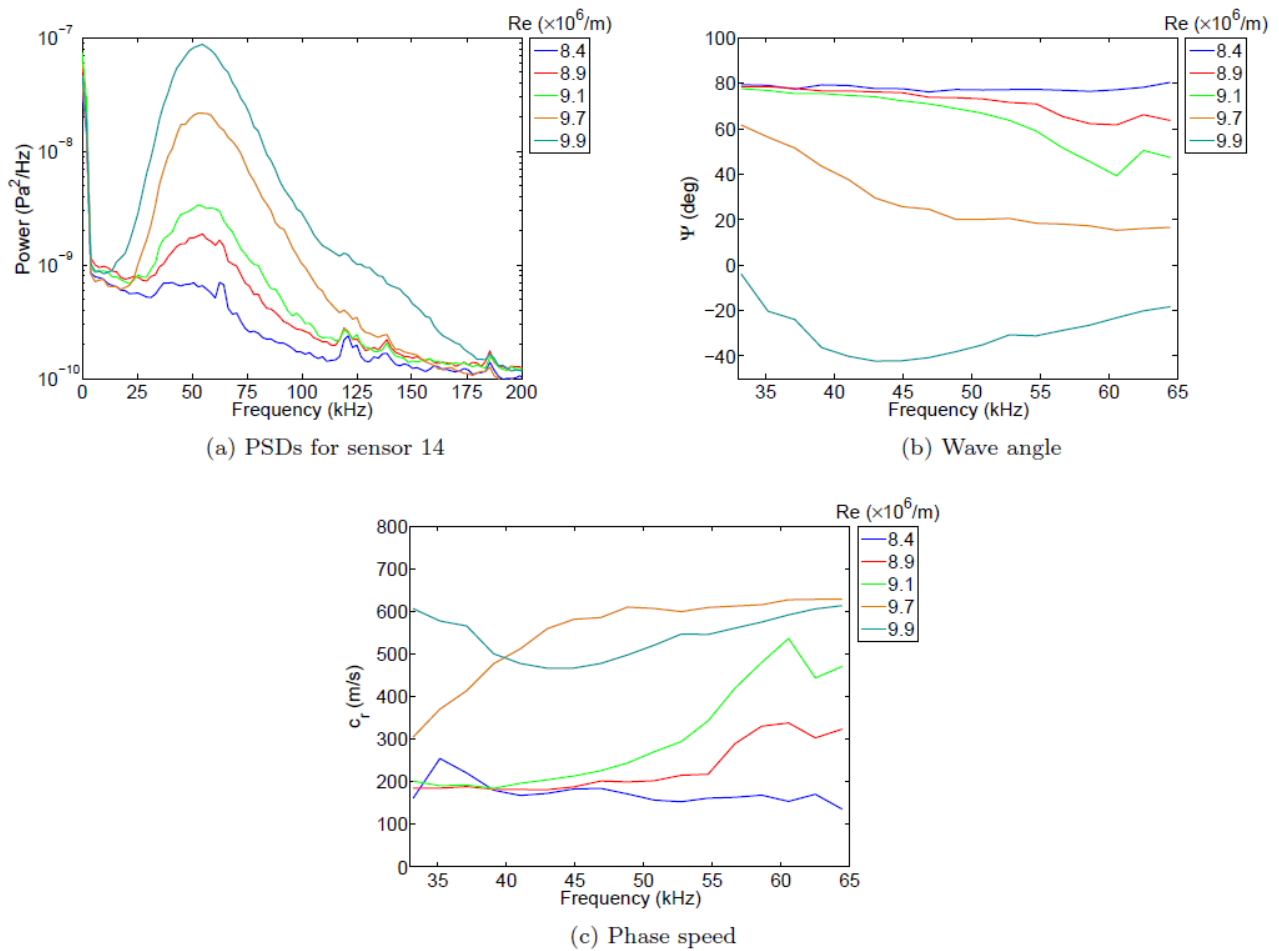
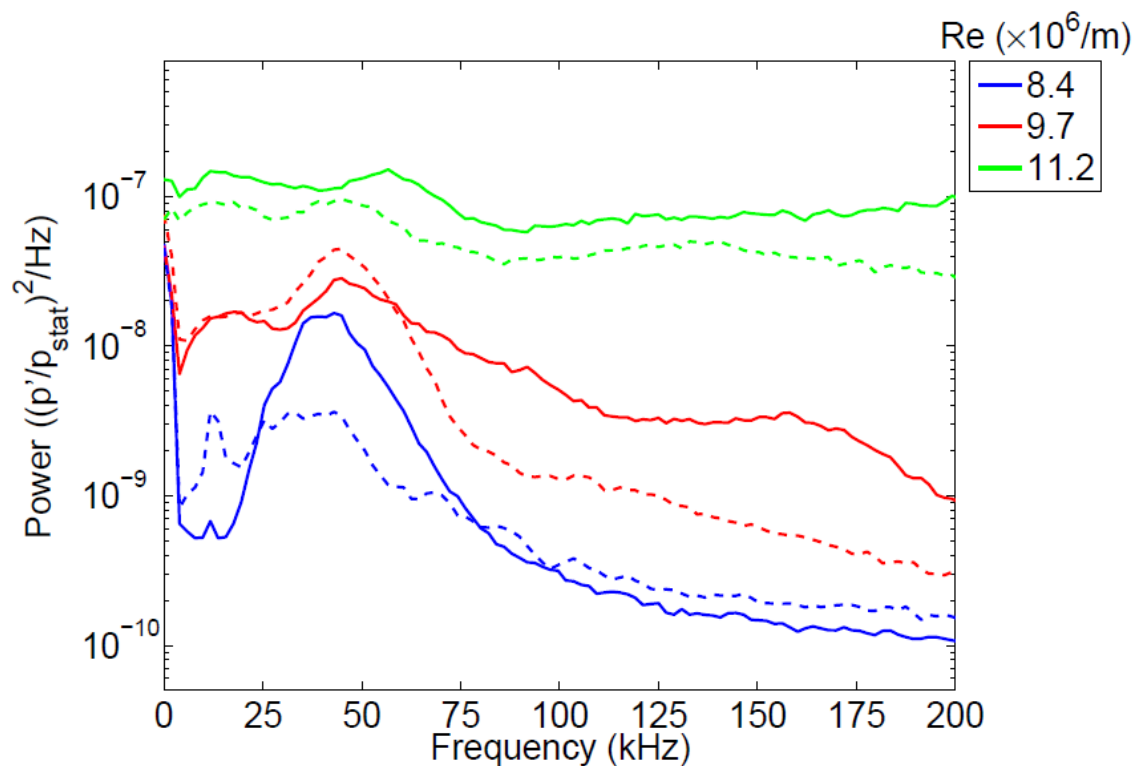


**Figure 2-12 Wave angles and phase speeds at sensors 13–15**

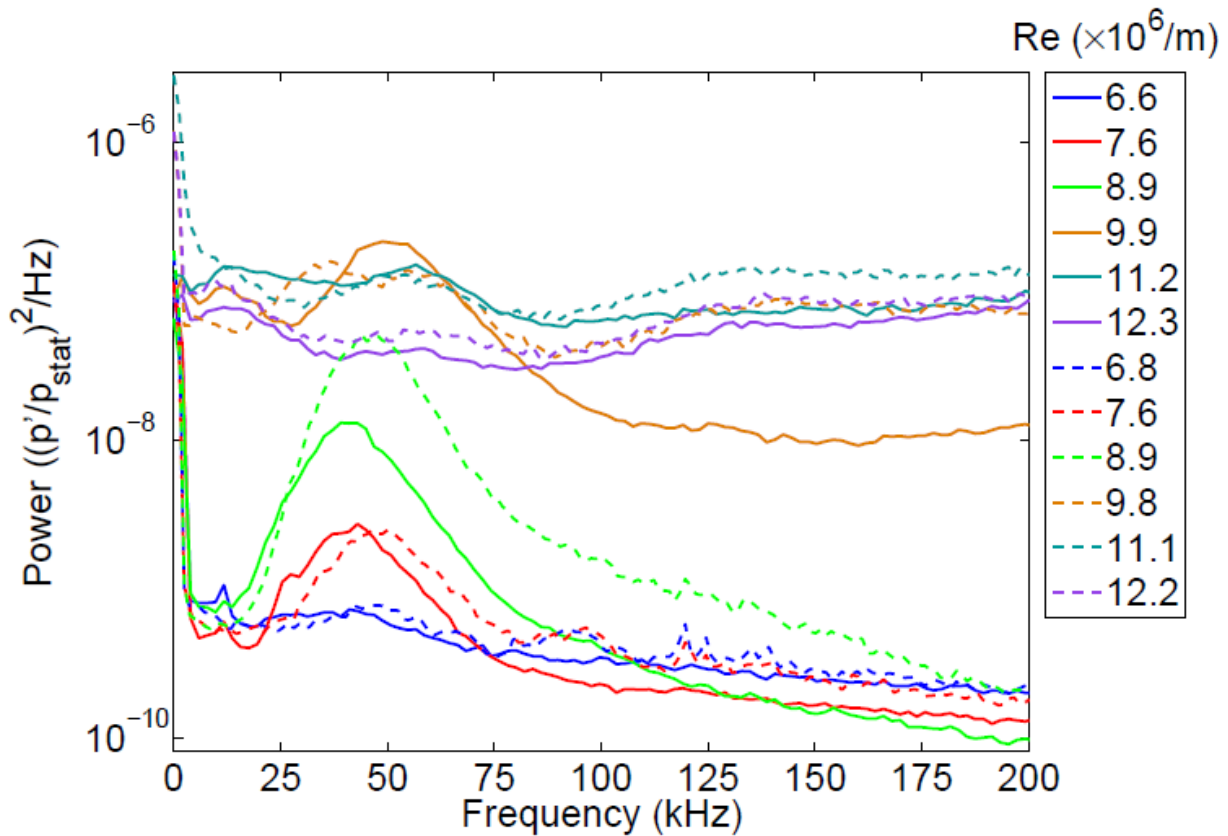
In addition to the seven groups of three pressure sensors on the top half of the model, one sensor was located in the same location as sensor 20, but on the bottom half of the model. Figure 2-13 shows PSDs for both sensors at three different freestream Reynolds numbers. Although the spectra from the two sensors bear some resemblance to each other, they do not match to the degree that would be expected if the model and the flow over it were truly symmetric about the model centerline. Traveling crossflow waves appear to be present at both sensors, but the peaks are not generally as pronounced for sensor 43 as they are for sensor 20. It may be that the differences in the stationary crossflow vortex pattern on the two halves of the model modulate the traveling crossflow waves. In previous work, DREs placed near the model leading edge were used to modify the stationary crossflow vortex pattern. The traveling crossflow waves were also significantly modified, being almost entirely suppressed for one DRE configuration.<sup>27</sup> Additionally, the model may have a small, non-zero yaw, the model geometry may exhibit some top/bottom asymmetry, or the tunnel flow may be slightly non-uniform.

Figure 2-14 shows PSDs for the new PEEK model and the previous aluminum model for pressure sensors at the sensor 20 location. Agreement in the spectra from the two models is generally quite good. For the aluminum model, the peak frequencies are shifted slightly higher

and the spectra look slightly further along in the transition process. This is evidenced by greater spectral broadening and higher broadband power levels. Nevertheless, the agreement suggests that the flow conditions and models are quite similar. Evidently, the aforementioned discrete surface roughness farther upstream on the PEEK model does not significantly alter the traveling crossflow waves when compared to the model used in the earlier experiments. However, the differences in surface roughness on the top and bottom sides of the PEEK model may still account for the differences between the top and bottom halves of the model.



**Figure 2-13 PSDs for sensors 20 and 43. Solid lines are sensor 20, dashed are sensor 43.**



**Figure 2-14 PSDs for sensor 20 on aluminum and PEEK models. Solid lines are PEEK model, dashed are aluminum.**

## 2.4. Noisy Flow

### 2.4.1. Heat Flux

Previous work utilizing oil flow visualization in noisy flow revealed stationary crossflow vortices.<sup>27</sup> However, temperature-sensitive paint (TSP) never showed such vortices. It was hoped that the more sensitive IR technique would be able to detect stationary crossflow vortices in noisy flow. The BAM6QT was intentionally run with elevated freestream noise levels. Heat flux contours for noisy flow for Reynolds numbers ranging from  $1.7\text{--}11.2 \times 10^6/\text{m}$  are shown in Figure 2-15. The intensity scales in Figure 2-15 change with each Reynolds number and are selected to best highlight the salient features.

For  $\text{Re}=1.7 \times 10^6/\text{m}$ , the two streaks adjacent to the model centerline undergo transition, while the boundary layer remains laminar elsewhere. As the Reynolds number is increased to  $2.8 \times 10^6/\text{m}$ , turbulent lobes are observed outboard of the near-centerline streaks. For further increases in the Reynolds number, the outboard turbulent lobes move farther upstream and spread outboard. The

location at which the near- centerline streaks transition also moves upstream. Stationary crossflow vortices are not visible in any of the IR images.

For  $Re=7.0$  and  $11.2\times 10^6/m$ , an interesting feature appears in the heat flux contours. Downstream of the transition front, the heat flux appears to first decrease and then suddenly increase. The location of the increase seems to move downstream at the higher Reynolds number. More recent data that could not be included in this paper did not show this feature. It is thus assumed that this feature is an artifact of this particular experimental setup. It may be due to a spurious reflection that was not accounted for.

Stationary crossflow vortices were not observed under quiet flow on the PEEK until  $Re\approx 8\times 10^6/m$ . Under noisy flow, the boundary layer on the model is largely turbulent for this and larger Reynolds numbers. For a given  $Re>8.0\times 10^6/m$ , in noisy flow the boundary layer is turbulent over the area of the model where vortices are visible in quiet flow. The earlier work with oil flow showed stationary vortices in noisy flow for  $Re=3.9-10.6\times 10^6/m$ .<sup>27</sup> It is unknown why the vortices are observed with oil flow in a noisy freestream, but are not seen in the IR data. Even though the vortices are not visible in noisy flow, it appears that the IR technique is more sensitive than earlier work with TSP.<sup>27, 36</sup>

#### **2.4.2. Pressure Sensors**

PSDs for pressure sensors 2, 8, 14, and 20 are shown in Figure 2-16. For sensors 8, 14, and 20, the spectra indicate that the boundary layer progresses from laminar to fully turbulent as the Reynolds number increases. Sensor 2 never appears to indicate a fully turbulent boundary layer, even at the highest Reynolds number shown. The spectra from all four sensors show small, low-frequency peaks. This is very similar behavior to what was reported in Ref. 25. No peaks due to the traveling crossflow instability are seen. As in the earlier work on an aluminum model, transition is observed, but there is no indication that it was precipitated by the growth and breakdown of traveling crossflow waves, even farther upstream.

#### **2.5. Summary and Conclusions**

A 38.1% scale model of the 2:1 elliptic cone HIFiRE-5 geometry was tested in both the noisy and quiet flows of the BAM6QT. IR thermography was used for the first time in this tunnel and was found to be suitable for detecting stationary crossflow vortices in quiet flow. The IR technique appears to offer superior sensitivity when compared to similar TSP measurements. Additionally, traveling crossflow instability waves were detected at some Reynolds number for almost all of the pressure sensor locations. The model used in the earlier experiments and the new model had stationary and traveling crossflow instabilities that were very similar. Thus, the crossflow instability properties appear to be somewhat insensitive to the particulars of each model and mostly dependent on the freestream flow conditions.

Stationary and traveling crossflow vortices were concurrently observed in quiet flow. Wave angles and phase speeds for traveling crossflow waves were calculated for one location on the model and were found to be between  $70-80^\circ$  and  $200-250$  m/s, respectively, for the peak frequency. The stationary vortex pattern appeared to be determined by surface roughness upstream of the PEEK shell on the bottom half of the model. The stationary vortex pattern on the top half of the

model appeared to be mostly determined by roughness upstream of the PEEK shell, but was somewhat modulated by the presence of the pressure sensors. Two predominant wavelengths were observed for the stationary vortices on the bottom half of the model, 3.0 and 4.2 mm, with only minor changes with Reynolds number. Neither crossflow mode was observed in noisy flow, even though the boundary layer over most of the model was observed to transition from fully laminar to fully turbulent as the freestream Reynolds number was increased. Thus, no primary transition mechanism could be determined for noisy flow.

The determination of the transition mechanism is fundamentally important in understanding and extrapolating transition measurements to flight. For example, Mack-mode instabilities produce transition on sharp and slightly-blunted cones at zero AoA, under both noisy and quiet flow. This commonality of transition mode gives some confidence in extrapolating transition to flight and accounting for trends due to differing boundary conditions. The difference in transition mechanism between noisy and quiet flow for the elliptic cone means that wind-tunnel-derived transition trends must be treated with more skepticism. An example of such an effect appears when planar and conical boundary layer transition is compared.<sup>37</sup> Future work will focus on acquiring improved pressure measurements to better diagnose the spatial evolution of traveling instabilities under noisy and quiet flow, with the aim of improving transition prediction and understanding the limitations of transition measurements made under noisy conditions.

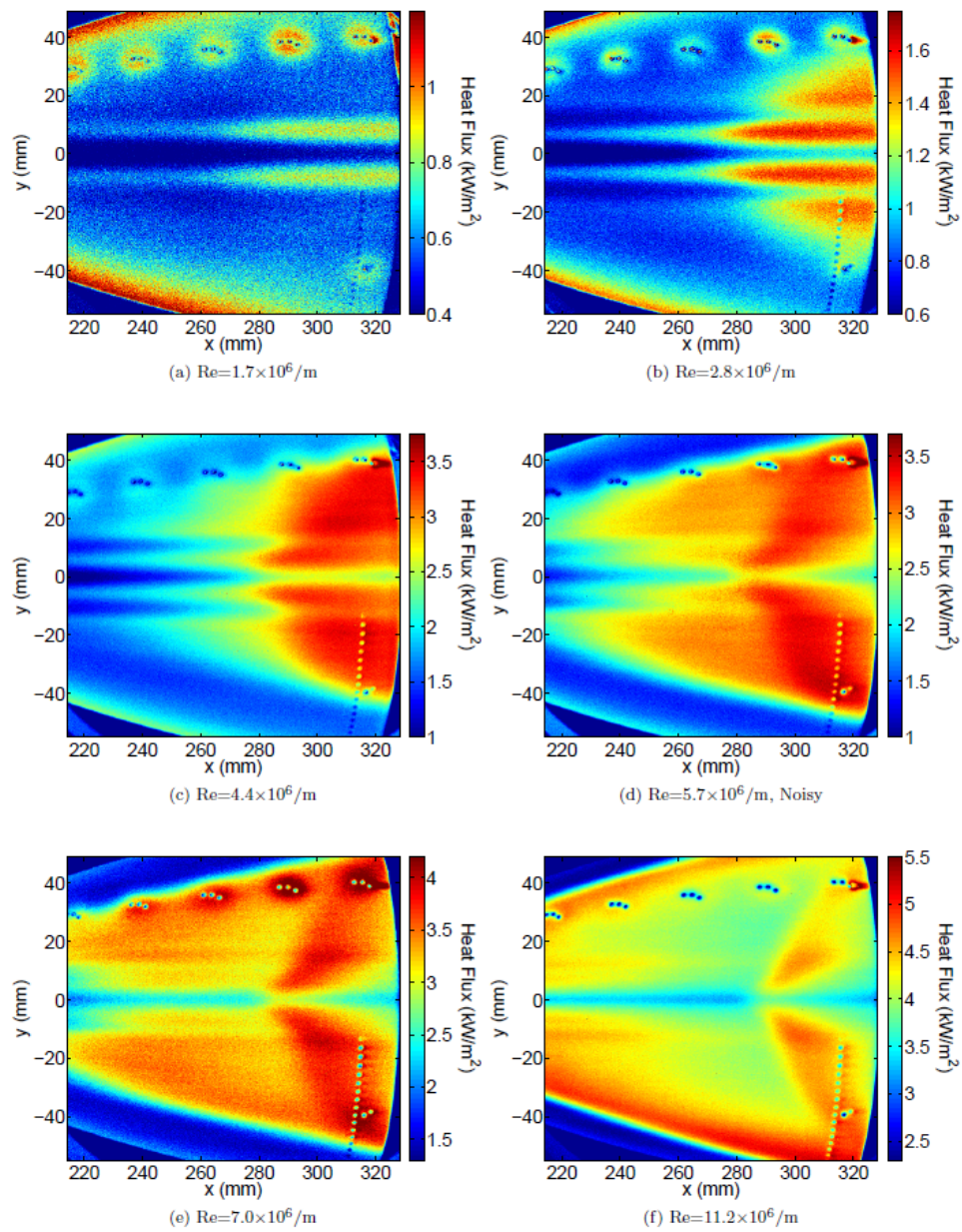


**Figure 2-15 Difference of IR images in noisy flow**



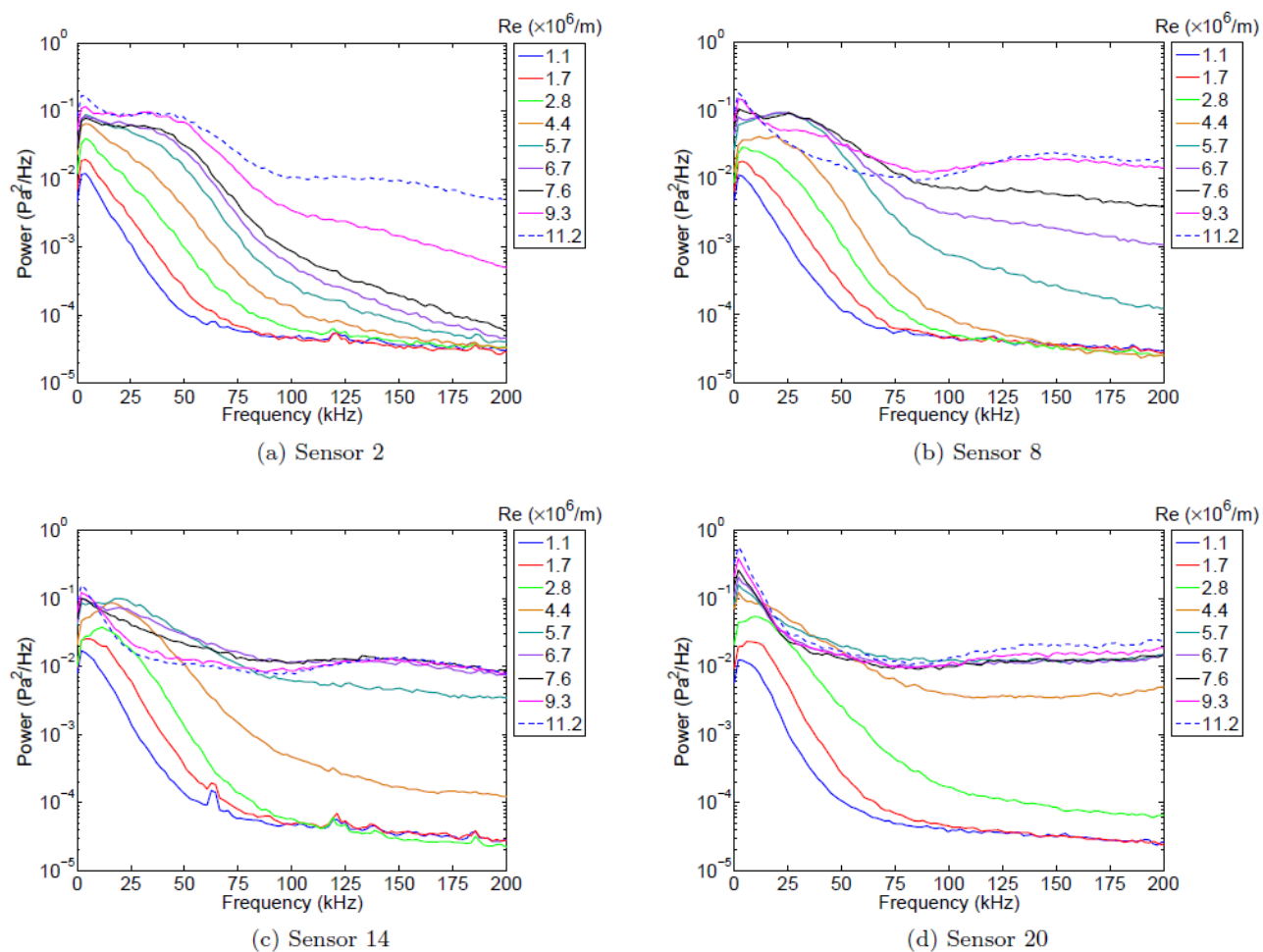


**Figure 2-16 PSDs for sensors 2, 8, 14, and 20**

### 3. Boundary Layer Stability Analysis for Stetson's Mach 6 Blunt Cone Experiments

#### 3.1. Background

Boundary layer transition is a critical factor in the design of hypersonic vehicles, with profound impact on both heat transfer and control characteristics. While many practical aerospace vehicles are blunt, the mechanisms that lead to boundary layer instability and transition on sharp bodies are more thoroughly understood at present. However, over the past half century, a wealth of relevant wind tunnel and flight data has been acquired. Analytical and computational techniques, as well as the rapid development of economical and powerful computer processors, have made possible comprehensive computational analysis of existing experimental datasets.

Between 1978 and 1982, K. F. Stetson performed a total of 196 sharp- and blunt-cone experiments [1, 2] on an 8-degree half-angle, 4 in. (10.16 cm) diameter cone in the AFRL Mach 6 High Reynolds Number facility.<sup>38, 39</sup> These experiments were reported in a 1983 paper<sup>38</sup> along with results from AEDC Tunnel F with a larger cone at Mach 9. While a subset of the AEDC Mach 9 results have received computational analysis,<sup>40</sup> the AFRL Mach 6 results have not, to date.

The availability of well-tested mean flow and stability prediction computer codes, along with multi-core machines, now makes it possible to analyze Stetson's Mach 6 results with detail and fidelity unavailable in 1983. Marineau et al. showed the utility of applying PSE stability predictions to transition experiments on blunt cones at Mach 10.<sup>41</sup> Stetson's Mach 6 experiments form a counterpoint to Marineau's Mach 10 experiments. Although the maximum length Reynolds numbers were comparable in the two experiments ( $47 \times 10^6$  for Marineau,  $33 \times 10^6$  for Stetson), the Stetson experiments were carried out in a smaller wind tunnel at higher freestream unit Reynolds number. Since wind tunnel noise scales on unit Reynolds number and wind tunnel size, and roughness effects depend on unit Reynolds number, the conditions for Stetson's Mach 6 experiments were substantially different from Marineau's.

The AFRL Mach 6 facility operates at stagnation pressure  $p_0$  from 700 to 2100 psi (4.83 to 14.5 MPa). Details of the maximum and minimum Reynolds numbers conditions, along with a sample intermediate case at the midpoint, are presented in Table 1. A total of 196 experiments encompassing 108 unique conditions comprise the Stetson Mach 6 results (see Section III).<sup>38</sup> Mean-flow and stability calculations for each unique condition were performed at a computational cost of about 100 processor-hours each.

**Table 3-1 Sample inflow conditions (minimum, maximum, and midpoint Reynolds numbers) computed for each bluntness value.**

$p_0$		unit $Re_\infty$	$M_\infty$	$\rho_\infty$	$P_\infty$	$T_\infty$	$U_\infty$	$T_w/T_0$
[psi]	[MPa]	$\times 10^6/\text{m}$	-	[kg/m <sup>3</sup> ]	[kPa]	[K]	[m/s]	-
700	4.83	30.7	5.9	0.154	3.40	76.7	1038	0.56
1400	9.65	61.4	5.9	0.308	6.80	76.7	1038	0.56
2100	14.5	92.1	5.9	0.461	10.2	76.7	1038	0.56

### 3.2. Computational Methods

The mean flow over the cone is computed by the reacting, axisymmetric Navier-Stokes equations with a structured grid, using a version of the NASA DPLR code<sup>42</sup> which is included as part of the STABL-2D software suite, as described by Johnson<sup>43</sup> and Johnson et al.<sup>44</sup>. This flow solver is based on the finite-volume formulation. The use of an excluded volume equation of state is not necessary because the static pressure over the cone is sufficiently low (typically, 10–50 kPa) that the gas can be treated as ideal. The mean flow is computed on a single-block, structured grid with dimensions of 361 cells by 359 cells in the streamwise and wall-normal directions, respectively. The inflow gas composition in each case is air with 0.233 O<sub>2</sub> and 0.767 N<sub>2</sub> mass fractions. While the computation includes chemistry, the impact of chemical reactions is negligible, as the local maximum temperature does not exceed 611 K for any case.

Grids for the 8-degree half angle sharp cone and each of the 10 bluntness conditions (see Table 2) were generated using STABL's built-in grid generator, and mean flow solutions examined to ensure that at least 100 points normal to the cone surface were placed in the boundary layer for each stagnation pressure. For simplicity and to match the Stetson nomenclature, bluntness as a percentage of the base radius of 2.0 in. (5.08 cm) is used to label the cases analyzed in the present work. The boundary layer profiles and edge properties are extracted from the mean flow solutions during post-processing. The wall-normal extent of the grid increases down the length of the cone, from 0.25 mm at the tip to 50 mm at the base, allowing for the shock to be fully contained within the grid for all cases tested. The grid is clustered at the wall as well as at the nose in order to capture the gradients in these locations. The non-dimensional wall distance  $y^+$  for the grid, extracted from the DPLR solution for each case, is everywhere less than 1, where  $y^+$  is used as a measure of local grid quality at the wall in the wall-normal direction.

**Table 3-2 Summary of grids generated for the present study, each corresponding to a different sharp or blunt nose tip used by Stetson.<sup>38</sup>**

	$R_N$		Bluntness
	in.	mm	%
0	0	0	0
0.02	0.508	1	
0.04	1.016	2	
0.06	1.524	3	
0.08	2.032	4	
0.10	2.540	5	
0.20	5.080	10	
0.30	7.620	15	
0.40	10.16	20	
0.50	12.70	25	
0.60	15.24	30	

A grid convergence study was performed on the  $R_N = 0.508$  mm (1%) and  $R_N = 5.08$  mm (10%) bluntness cases at the study's maximum unit Reynolds number,  $92.1 \times 10^6/\text{m}$ , which corresponds to tunnel stagnation pressure  $p_0 = 2100$  psi (14.5 MPa). As the boundary layer is thinnest for the highest stagnation pressure, these represent the most challenging cases for each grid to properly resolve. In addition to the normal  $361$  streamwise and  $359$  wall-normal cell case, grids of  $301 \times 299$ ,  $431 \times 419$ , and  $501 \times 499$  cells were computed for these two cases. The normal  $361 \times 359$  cell case was found to be sufficiently converged for both bluntnesses examined. The stability results from the  $R_N = 0.508$  mm (1%) convergence study are presented in Figure 3-1. While there is a minimal discrepancy at the end of the computational geometry for the most coarse grid, convergence is sufficiently achieved for the other three cases, including the  $361 \times 359$  cell case, which was used for the rest of the study.

### 3.3. Mean Flow Based Transition Correlations

Stetson<sup>38</sup> reported results by “normalizing” the transition Reynolds numbers for blunted cones by the transition Reynolds numbers for sharp cones at the same inflow conditions, which are calculated as

$$\frac{X_{\text{TrB}}}{X_{\text{TrS}}} = \frac{(\text{Re}_X)_{\text{TrB}} (\text{Re}_{\text{unit}})_{\text{eS}}}{(\text{Re}_X)_{\text{TrS}} (\text{Re}_{\text{unit}})_{\text{eB}}}$$

:

1

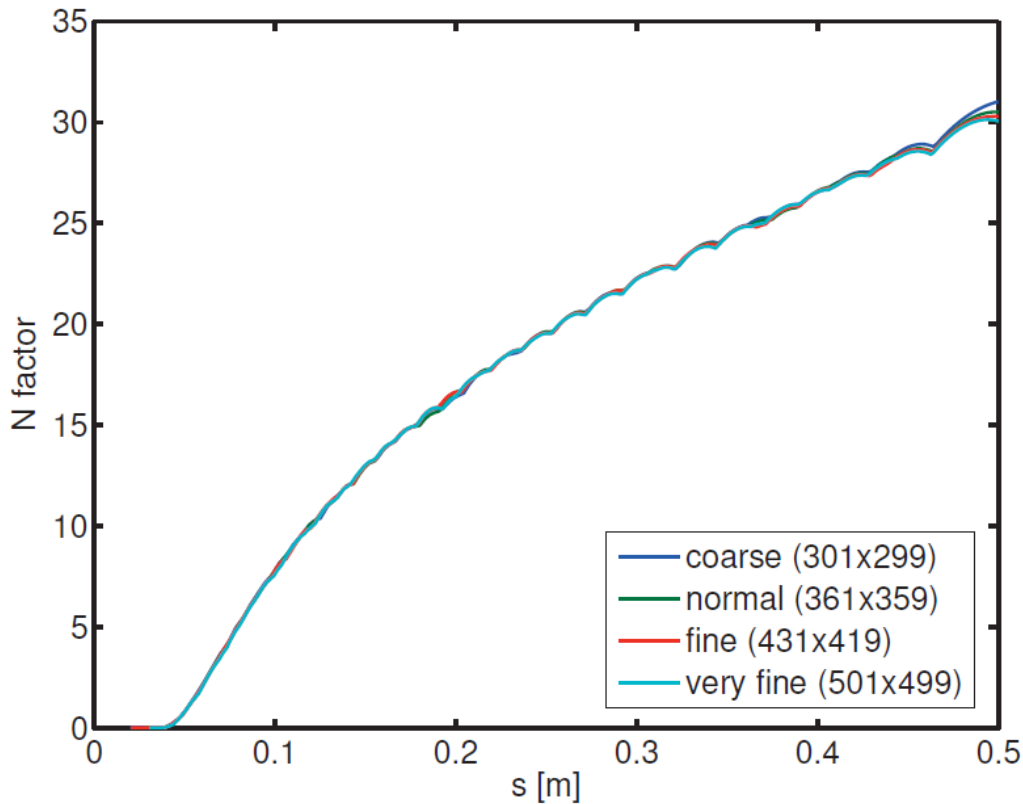


**Figure 3-1 Stability results from the  $R_N = 0.508$  mm (1%), unit Reynolds number  $92.1 \times 10^6/\text{m}$  convergence study.**

Stetson found  $X_{Tr}$  values by examining heat transfer plots and selecting the first data point elevated above the laminar curve (see Figure 3-2 for an illustration of this process). As the thermocouples were spaced at 0.5 in. (12.7 mm) intervals, this is the approximate uncertainty of the measurement. All of the transition locations in the present work were reported in Stetson's notebook.<sup>39</sup> The original heat transfer plots were not available, but one example from the same series of experiments, a sharp condition with  $p_0 = 700$  psi, is available in Figure 7 of Reference 45. The heat transfer results from this plot were digitized, replotted in terms of Stanton number and Reynolds number, and are reproduced in Figure 3-2 along with Stetson's indicated transition location, as well as laminar and turbulent sharp cone Stanton number correlations<sup>46</sup>, and laminar computations from the present work, for comparison. The laminar computation and correlation both agree well with the non-dimensionalized heat transfer data, and the experimental points reach the turbulent value after transition onset.

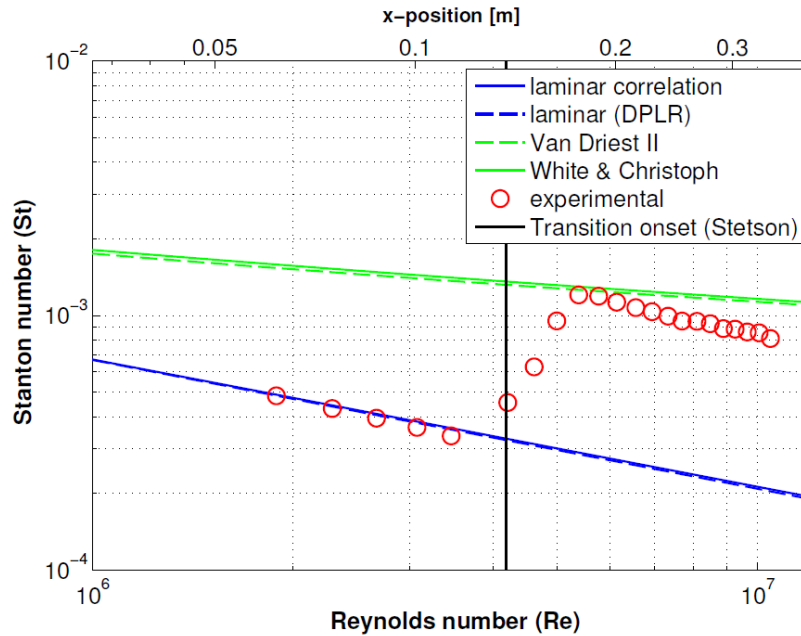


**Figure 3-2 Stanton number vs. Reynolds number for the sharp  $p_0 = 700$  psi condition, with laminar and turbulent correlations, and laminar computation, for comparison.**

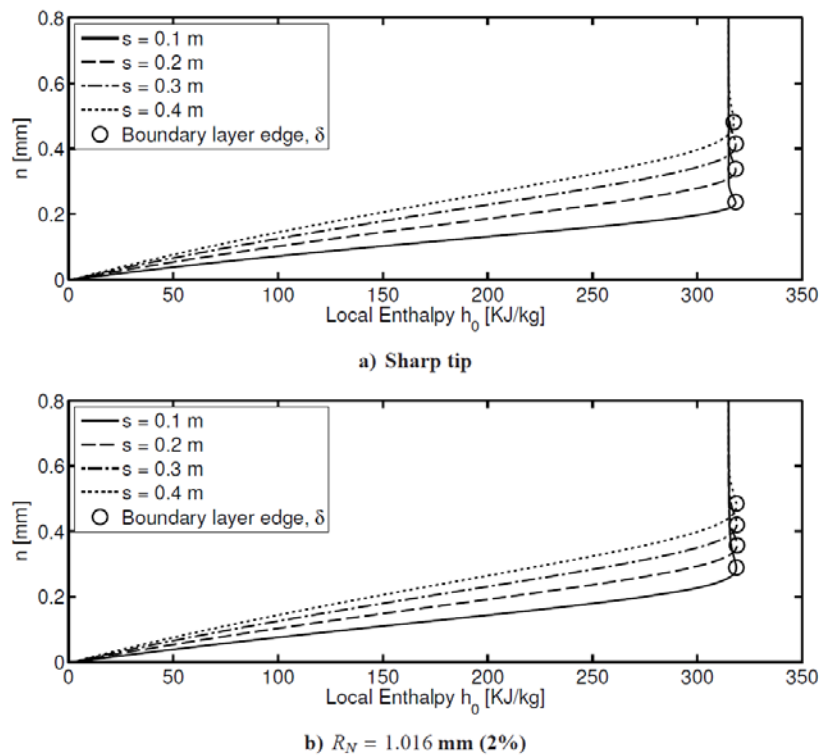


**Figure 3-3 Sharp and blunt total enthalpy profiles with boundary layer edge indicated,  $p_0 = 1400$  psi.**

The boundary layer edge, throughout the present work, is defined as the point at which the derivative of the total enthalpy (see Figure 3-3) along a line extending orthogonally from the surface of the cone becomes zero, as suggested by Bertin<sup>47</sup> for cases where the total enthalpy  $h$  near the edge of the boundary layer locally exceeds  $h_\infty$ . Stetson<sup>38</sup> utilized selected computations with two boundary layer codes and used some interpolations to find the unit Reynolds number and Mach number at the boundary layer edge and throughout the entropy layer, but notes that “it was not considered practical to make boundary layer calculations for all of the geometric and flow variations of the present investigation.” This is now possible; in fact, the full flow field including the shock was calculated for each case in the present study, and two examples for a sharp and blunt case are presented in Figure 3-4. While the freestream unit Reynolds number is  $61.4 \times 10^6/\text{m}$  for both cases, the large “swallowing length” of the blunt case is evident as a large local region of low unit Reynolds number fluid next to the wall.

The entropy layer swallowing length estimate of Rotta<sup>48</sup> ( $X_{sw}$ ) was used by Stetson and Rushton<sup>49</sup> to correlate results, and was also applied to the current analysis. This correlation involves the edge unit Reynolds number, which can be difficult to define for a blunt cone. Because of this, it was considered worthwhile to re-compute the edge unit Reynolds number using DPLR, and compare the derived swallowing length correlation to Stetson’s original results. Stetson’s experimental data from Figure 9 of Reference 38 is replotted in Figure 3-5 and Figure 3-6 with DPLR-derived values of edge unit Reynolds number to obtain the swallowing length from Rotta’s correlation. Figure 3-5 and Figure 3-6 show no significant differences from Stetson’s<sup>38</sup> Figure 9 data, which is replotted from the calculated values recorded in Stetson’s notebook as small dots. The maximum difference from the data reported by Stetson is less than 2%.

In addition to the Rotta estimate, DPLR solutions were used to visualize the entropy layer, as shown in Figure 3-7. The Cantera<sup>50</sup> thermodynamics software package was used to calculate entropy for each cell based on the computed gas composition, temperature, and pressure. The large entropy layer swallowing length of the blunt case is evident as a large local region of high entropy fluid behind the curved shock and next to the wall, which is initially much thicker than the boundary layer. The estimated swallowing length  $X_{sw}$  calculated with the method of Rotta<sup>48</sup> as applied by Stetson and Rushton<sup>49</sup> is 24.2 cm for this case, well beyond the field of view in Figure 3-7b.

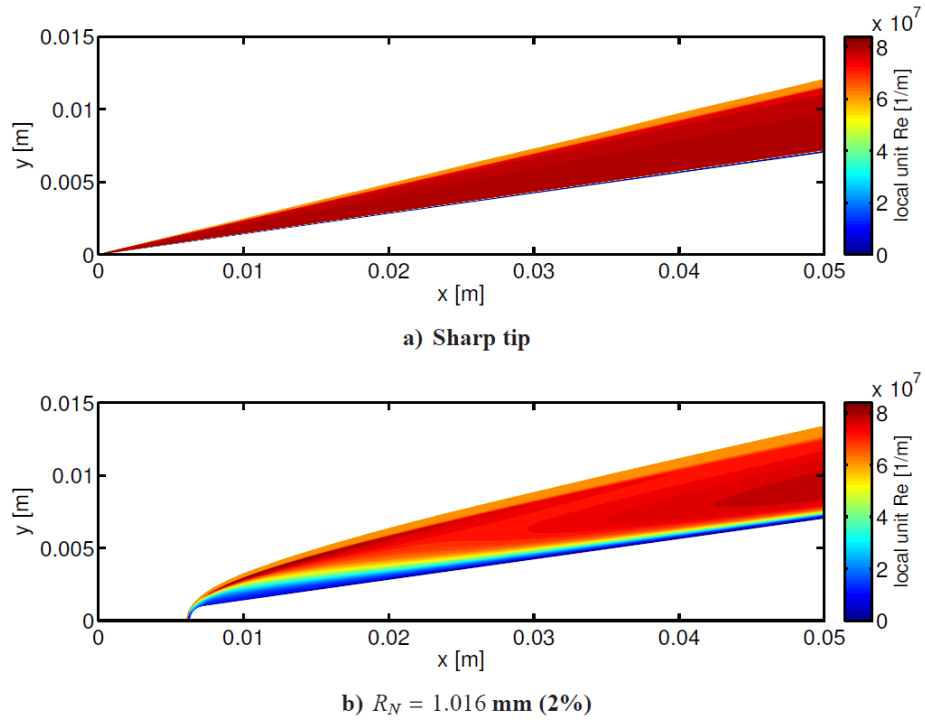


**Figure 3-4 Sharp and blunt unit Reynolds number contours (detail),  $p_0 = 1400$  psi.**

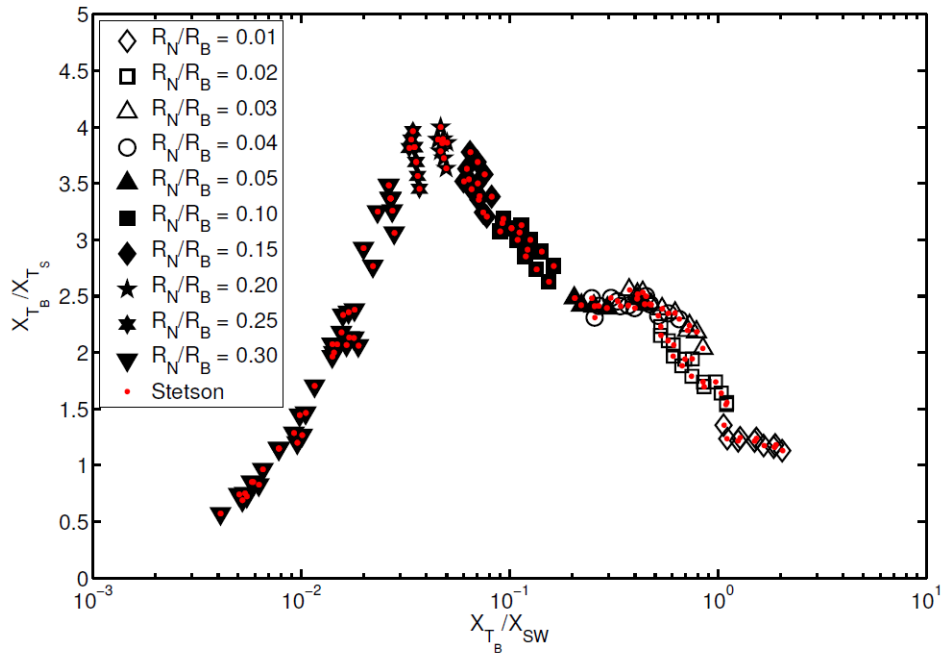


**Figure 3-5 Nosetip bluntness normalized by swallowing length vs. the transition location ratio.**



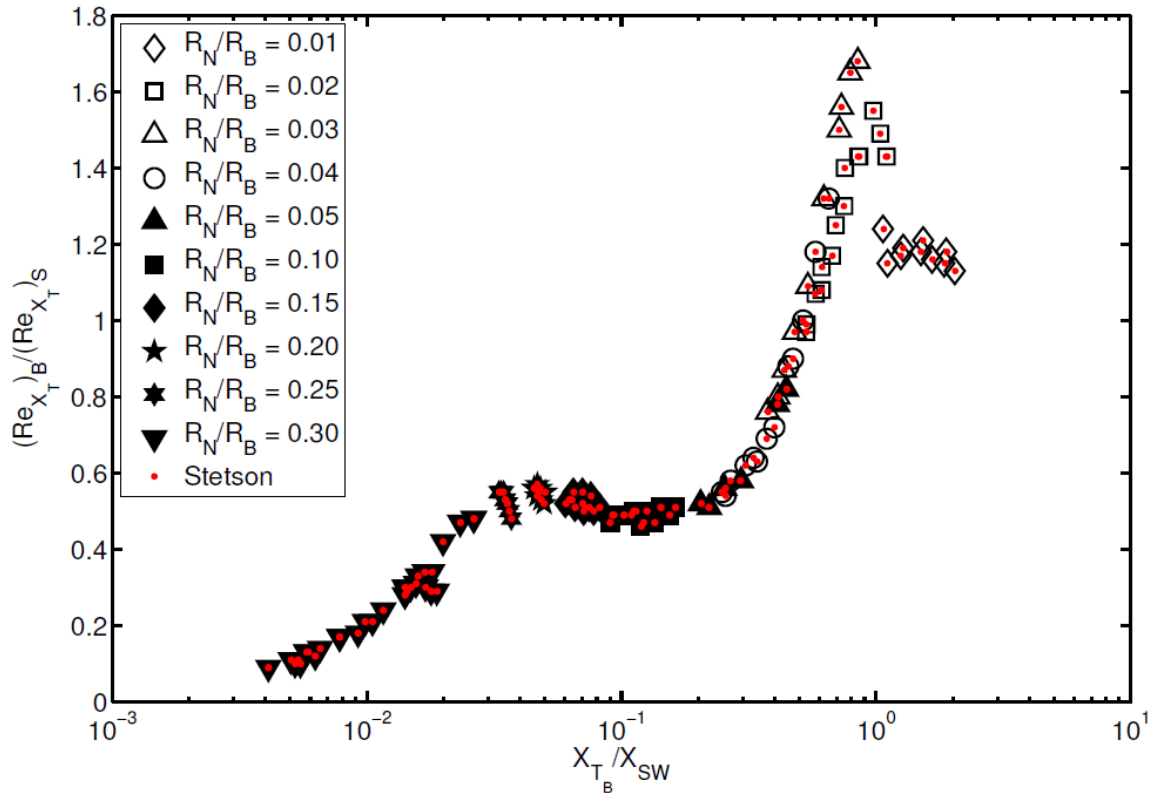


**Figure 3-6 Nosetip bluntness normalized by swallowing length vs. transition Reynolds number ratio.**

Following Marineau et al.<sup>41</sup> and Moraru<sup>51</sup>, the Stetson<sup>38</sup> results may also be presented, as in Figure 3-8, as a function of the freestream Reynolds number calculated with the nose radius as the relevant length scale. In this approach, the freestream Reynolds number at observed transition location increases with nosetip Reynolds number before dropping off sharply at about  $9 \times 10^5$ . This pattern is consistent with that observed by Marineau et al.<sup>41</sup> and Moraru<sup>51</sup>, although those authors found the drop-off point at nosetip Reynolds numbers of about  $3 \times 10^5$ .

### 3.4. Stability Computations

The stability analyses are performed using the PSE-Chem solver, which is also part of the STABL- 2D software suite. PSE-Chem<sup>52</sup> solves the reacting, two-dimensional, axisymmetric, linear parabolized stability equations (PSE) to predict the amplification of disturbances as they interact with the boundary layer. The PSE-Chem solver includes finite-rate chemistry and translational- vibrational energy exchange. The parabolized stability equations predict the amplification of disturbances as they interact with the boundary layer.

The band of amplified frequencies within the boundary layer predicted by LST is presented in a contour plot in terms of disturbance growth rate  $-\alpha_i$  in Figure 3-9.

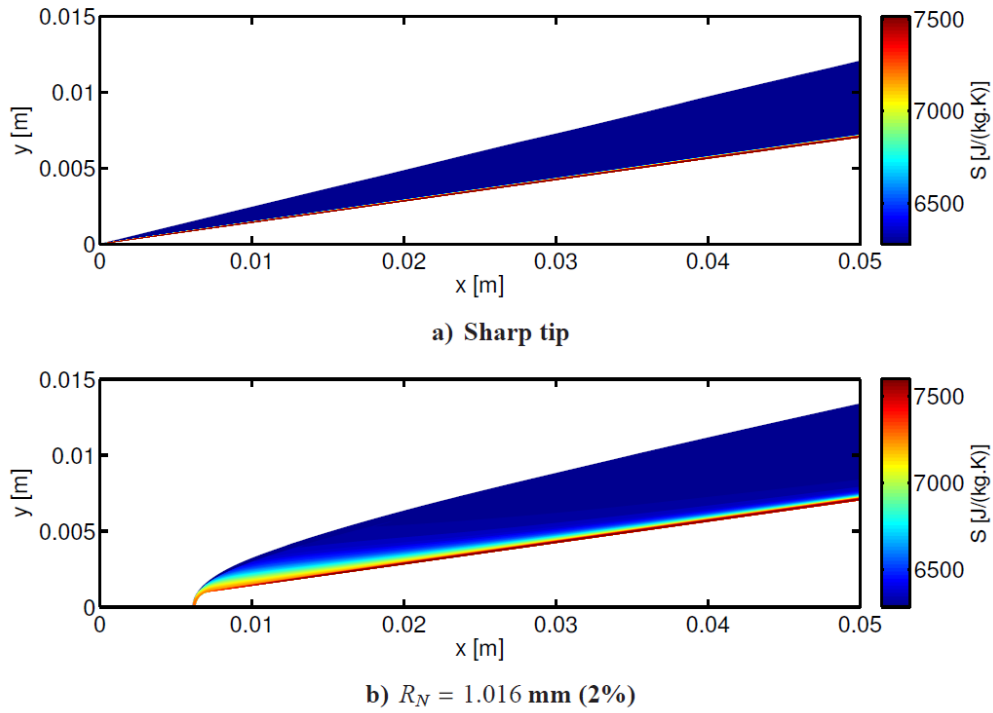


**Figure 3-7 Sharp and blunt cone entropy contours (detail),  $p_0 = 1400 \text{ psi}$ .**

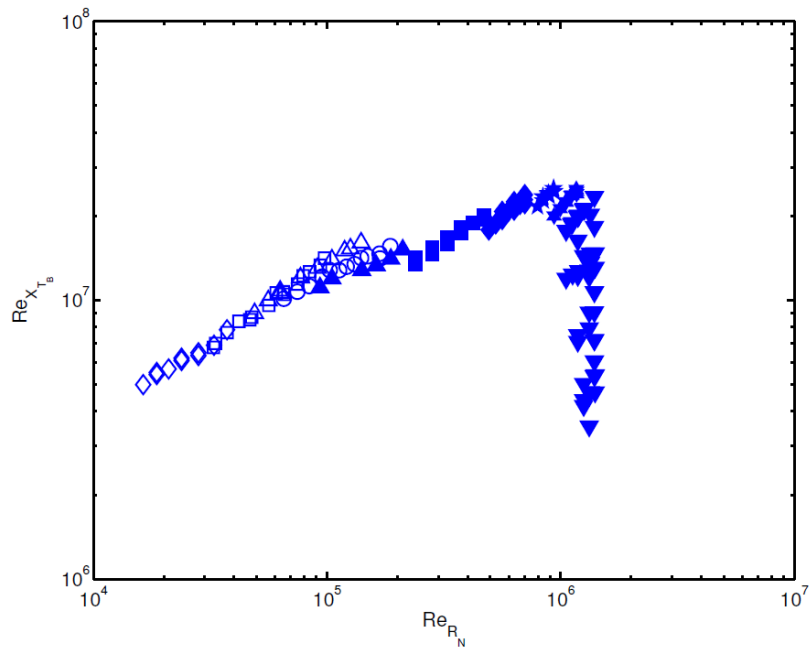


**Figure 3-8 Results as a function of nosetip freestream Reynolds number, where  $Re_{X_{TB}} = Re_{unit,\infty} X_{Tr}$  and  $Re_{R_N} = Re_{unit,\infty} R_N$**

In the present work the focus was on the 2D second mode, which should be dominant above approximately Mach 4.5 for conical geometry with significant wall cooling.<sup>53</sup> Marineau et al.<sup>41</sup> also did not observe strong first-mode activity in experimental results derived from a ray of surface mounted pressure transducers. Nevertheless, frequencies low enough to include the 2D first mode were also examined comprehensively, and oblique first modes were included in the computation for a subset of the blunt cases. Specifically, an oblique test matrix examined instabilities of spanwise complex wavenumbers  $\beta$  from 1/rad to 3000/rad and frequencies  $\omega$  from 20 kHz to 800 kHz over the entire surface of the cone for each of the bluntnesses listed in Table 2. For each bluntness, the study's maximum unit Reynolds number,  $92.1 \times 10^6/\text{m}$ , which corresponds to tunnel stagnation pressure  $p_0 = 2100$  psi (14.5 MPa), was chosen as the mean flow solution input for the oblique analysis. The results of this oblique mode study are tabulated in Table 3, which records the oblique mode with the maximum  $N$ -factor (where the maximum  $N$ -factor of an oblique mode is greater than the  $N$ -factor for the most unstable 2D mode at the same location) for each case. Significant amplification beyond that computed for the second mode was not observed in the computational results for any of the oblique cases. No amplification greater than that of the second mode was observed at any location for bluntnesses less than  $R_N = 10.16$  mm, so these cases are omitted from Table 2.

**Table 3-3 Characteristics of most unstable modes for cases where oblique modes dominate**

	$R_N$	$s$	$\psi$	$\omega$	$N_{\max}$
in.	mm	m	deg	kHz	
0.40	10.16	0.400	6.97	572.5	0.41
0.50	12.70	0.047	0.92	670.0	0.01
0.60	15.24	0.046	0.79	702.5	0.04

Computed second mode  $N$ -factors at the experimental transition location are presented in Figure 3-10. A strong trend with both nose tip bluntness and swallowing length ratio is observed. Note that the sharp data points (noted with an arrow) are located at infinity on the  $x$ -axis, as the swallowing length approaches infinity, and appear to be the asymptotic value for  $N$ -factor at transition with decreasing nose tip bluntness. An inset plot details the region of most rapid change in transition  $N$ -factor. Three regions are evident: for  $X_T/X_{SW} < 0.3$ , the computed  $N$ -factors at transition are less than one, indicating that modal growth is minimal and implying that an alternate transition mechanism, rather than the second mode, is important in this region, which is populated by the blunter cases. This result is consistent with past LST calculations on a smaller number of blunt hypersonic cone cases, for example Lei and Zhong.<sup>54</sup> Marineau et al.,<sup>41</sup> who observed a similar effect experimentally, propose that transient growth<sup>55</sup> or entropy-layer instability<sup>56</sup> may be plausible candidate mechanisms. From  $0.3 < X_T/X_{SW} < 1.0$ , the computed  $N$ -factor of transition rapidly increases. In this region, significant modal growth occurs and may compete with other mechanisms to provoke laminar-turbulent transition. For  $X_T/X_{SW} > 1.0$ , which includes the sharpest cones in the dataset, a consistent computed transition  $N$ -factor, falling within a range of 6.9 to 7.7, is observed. This result is consistent with Mack's second mode<sup>53</sup> as the dominant instability mechanism for the sharpest cases, and also significantly higher than the typical value of transition onset  $N \approx 5-6$  usually characterizing a "noisy" tunnel.<sup>57</sup>

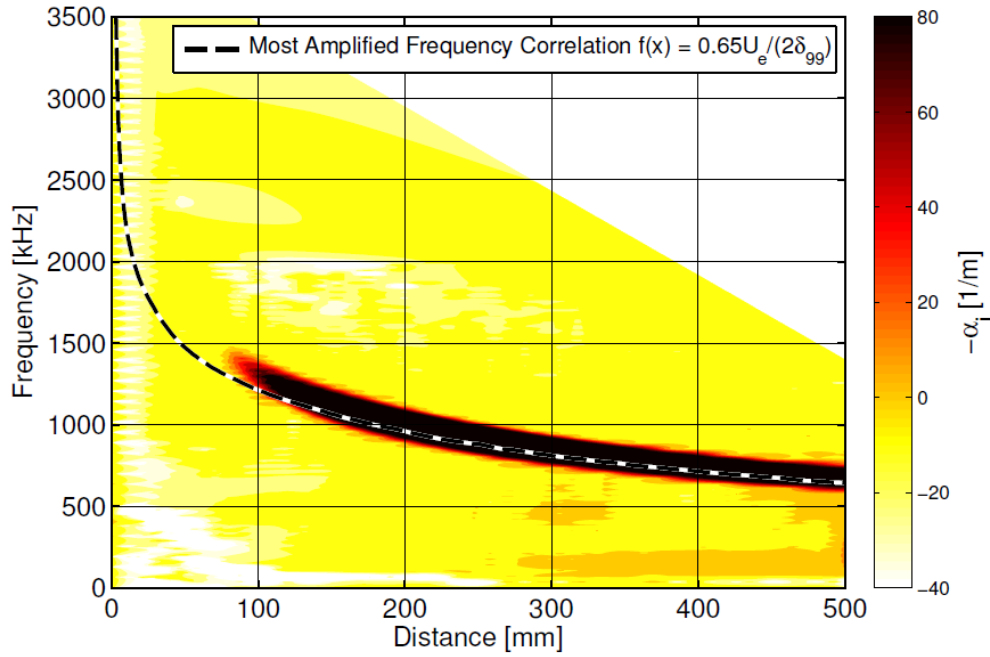


**Figure 3-9** LST contours of  $-\alpha_i$  for  $R_N = 1.016$  mm (2%) for  $p_0 = 1400$  psi.

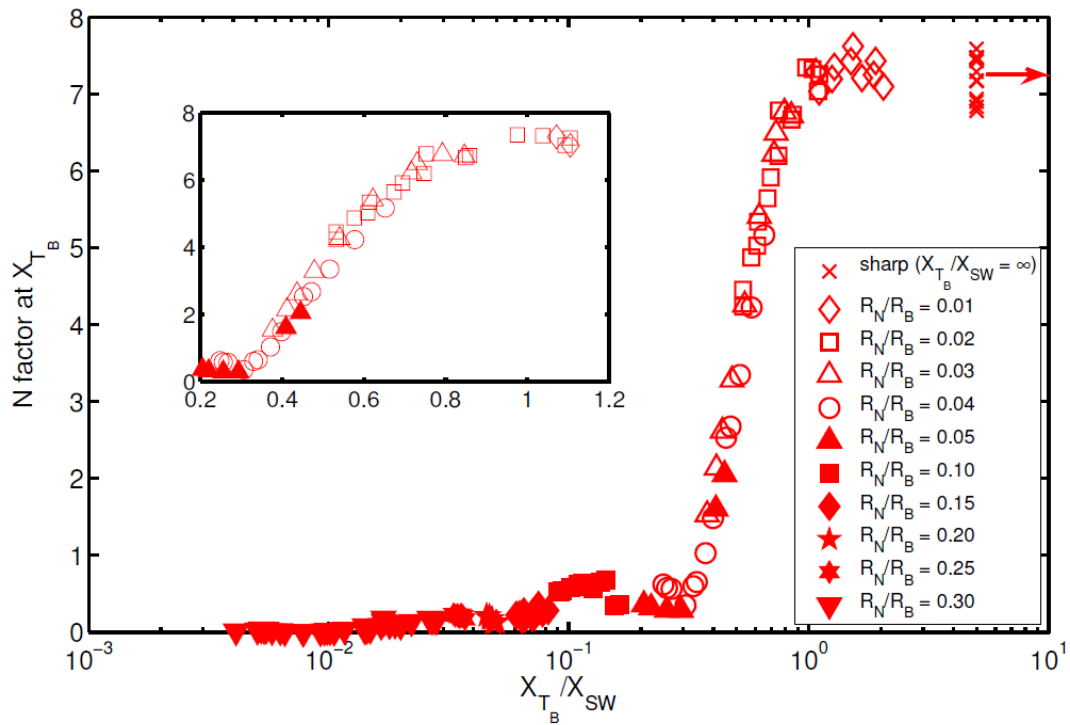


**Figure 3-10** Computed  $N$ -factor at experimentally measured transition location.

Transition in conventional hypersonic wind tunnels on cones with small bluntness has in some cases<sup>58</sup> been well-correlated with  $N$ -factors of about 5.5. Recent results<sup>46, 59, 60</sup> have found higher transition  $N$ -factors in some noisy hypersonic tunnels for cases where there is a mismatch between the strongest freestream noise frequencies and the most unstable boundary layer frequencies. Evidence supporting this mismatch hypothesis in previous studies has included a dependency of the correlating  $N$ -factor with the most unstable frequency at transition, in an effort to account for decreasing tunnel noise amplitude at higher frequencies. In contrast, the present dataset taken as a whole does not show any clear systematic variation in computed most amplified frequency at the measured transition location (see Figure 3-11). In fact, within each nose bluntness subset, the transition  $N$ -factor decreases with increasing frequency, which is the opposite of the effect that would be expected for noise-dominated transition onset with the typical noise spectrum of a hypersonic nozzle, which has higher amplitudes (and therefore, it is inferred, lower  $N$ -factors of transition) at lower frequencies. The outliers above 2000 kHz are likely the result of early bypass transition in the associated experiments, caused by roughness, particulate, or another unknown factor, when the boundary layer is still relatively thin and the calculated most unstable frequency is therefore large.

The region in which the second mode is significant may be defined by Mach number at the boundary layer edge, which in Figure 3-12a is presented at the measured point of transition as a function of  $X_T/X_{SW}$ . Figure 3-12b presents the variation of computed  $N$ -factor at the measured transition location as a function of edge Mach number. The maximum computed second mode  $N$ -factors occur for  $M_e > 4.5$ , while small second mode  $N$ -factors are computed for  $M_e < 3.9$ , which is consistent with the predictions of Mack<sup>53</sup> for the variation in the strength of the second-mode instability with Mach number. Since bluntness and resultant entropy layer swallowing length effectively mediate the edge Mach number, this may be the effect by which the second mode is emphasized or de-emphasized in the transition process. However, it does not indicate the alternate instability mechanism responsible for transition in the blunter cases with lower edge Mach number. The systematic oblique mode analysis described above for the highest Reynolds number case at each bluntness did not show significant amplification, which excludes oblique modes as the dominant instability mechanism for the blunt cases. As bluntness increases and the calculated swallowing distance lengthens, the computed  $N$ -factor at the experimentally-observed transition onset location drops below the level at which either the first or the second mode would be expected to lead to transition.<sup>61 62</sup> As the dominant instability mechanism for the transition reversal is neither the first nor the second mode, it is not explained by LST.

### 3.5. Conclusion

A strong trend in transition onset  $N$ -factor for both nose tip bluntness and swallowing length ratio is observed in the results computed (see Figure 3-10) from the complete set of Stetson Mach 6 conditions. As bluntness increases and the calculated swallowing distance lengthens, the computed  $N$ -factor at the experimentally-observed transition location drops below the level at which Mack's second mode would be expected to lead to transition. These results indicate that the dominant instability mechanism for the bluntest cases is likely not the second mode, which is consistent with recent blunt cone results at different conditions. A systematic examination of oblique modes for a subset of the cases also indicates that these are not the dominant instability mechanism, so the transition reversal is not explained by LST. Alternate instability mechanisms include transient growth or mean flow distortion from roughness, and entropy-layer instability.

Based upon the computed second-mode amplification factors  $e^N$ , transition onset in the AFRL Mach 6 High Reynolds Number facility is estimated to correspond to  $N \approx 7$  for the sharp and nearly sharp cases. These amplification values are high as compared to the more typical value of  $N \approx 5-6$  usually characterizing a “noisy” tunnel. One partial explanation may be a mismatch between the strongest freestream noise frequencies and the most unstable second mode boundary layer frequencies; however, no systematic variation in the computed most-unstable frequency at observed transition location is seen in the present dataset. Measurements of freestream and boundary layer instabilities in the Mach 6 tunnel, as well as further analysis of the oblique first modes, would be essential for further investigation of this potential effect.

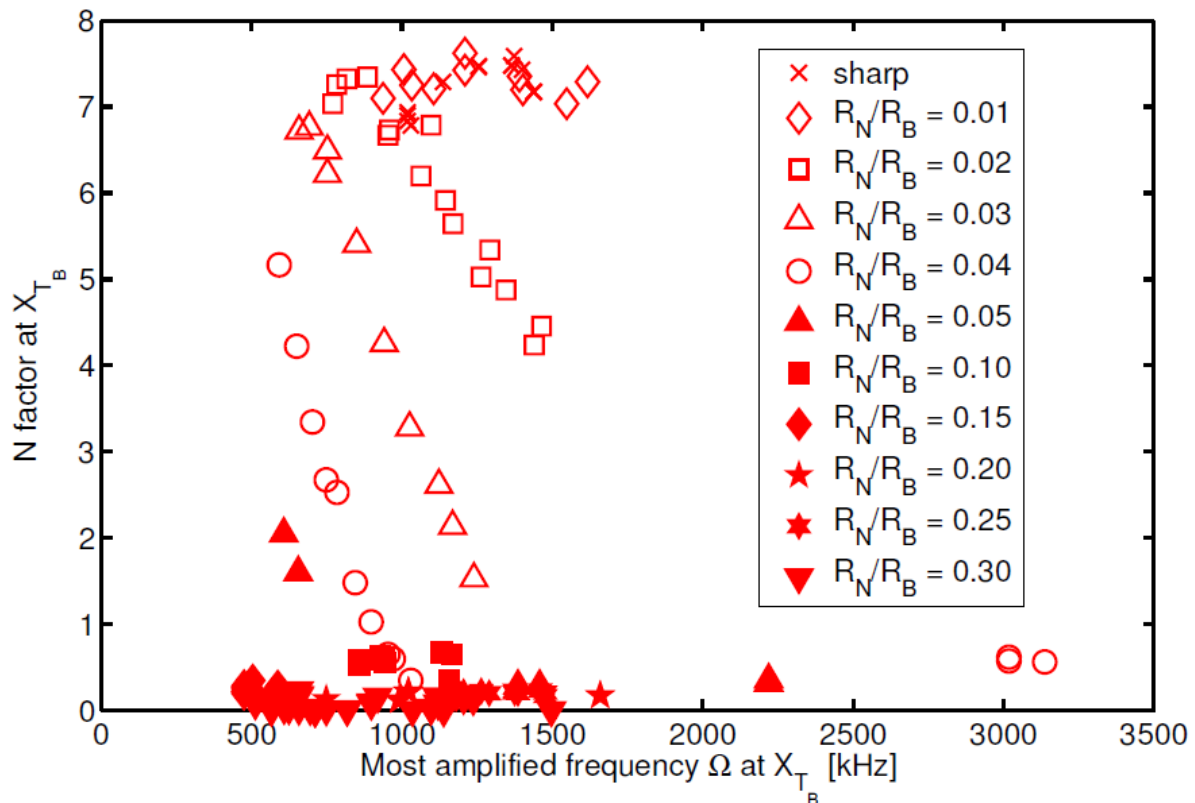


**Figure 3-11 Transition  $N$ -factor vs. computed most amplified frequency at transition location.**

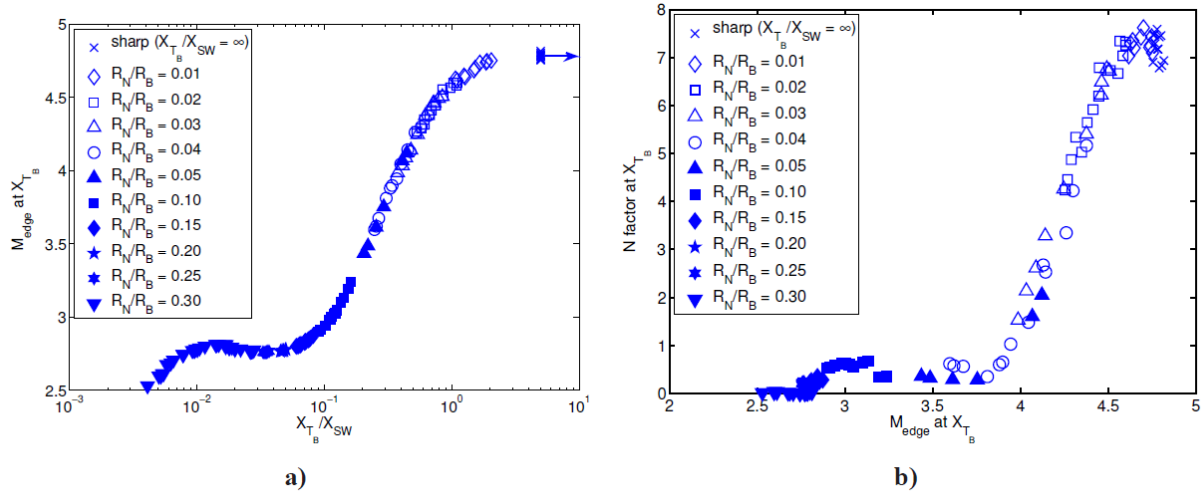


**Figure 3-12 Edge Mach number effects: a) Mach number vs.  $X_T/X_{SW}$ , b)  $N$ -factor vs. Mach number.**

## **4. Disturbance and Phase Speed Measurements for Shock Tubes and Hypersonic Boundary-Layer Instability**

### **4.1. Introduction**

In the study of hypersonic boundary-layer instability, recent research has focused on predicting, with numerical methods, the frequency content of disturbances that are measured over simple geometries. The motivation for these efforts is to refine the computational predictive tools when they are applied to flowfields with the most tractable and separable problems.

To facilitate the development of boundary-layer transition prediction tools, advances in experimental methods must also keep pace. Here, we focus on the application and development of two techniques: focusing schlieren deflectometry and FLDI. The focusing schlieren technique is well-known and in current use. The FLDI is here applied in a new way, set up such that two very closely spaced probe volumes permit the measurement of the phase speed or convective velocity of density disturbances in the flowfield, including in a shock tube and also for hypersonic boundary-layer instability wave-packets in a hypersonic ground-test facility. This technique will ultimately enable the measurement of both phase speed and frequency content, which should serve to support improvements in predictive capabilities.

### **4.2. Focusing schlieren Setup**

A Z-type focusing schlieren<sup>63, 64</sup> configuration is used in the present study. A high-powered LED light source with a condenser lens and a slit is used as an extended light source. The LED light source is a CXA3070 Cree X-Lamp, cool white in color, with a luminosity of 7945 lm, and is purchased from Mouser Electronics. In this configuration a heat sink is also required to conduct the heat away from the LED. In addition, a Photron SA-Z Camera with 50 mm focal length lens is used to register the schlieren images at resolutions up to 896×448 pixels with frame rates from 50,400 fps to 900,000 fps and exposure times less than 1  $\mu$ s.

Figure 4-1 shows a schematic of the focusing schlieren imaging system deployed in the new AFRL shock tube. The optical components are comprised of the high-powered LED light source (as above), a Fresnel lens, a 360 mm f/6.5 focusing camera lens, and complementary source and cutoff grids. The source grid is an array of horizontal clear-and-opaque bands, which function as multiple schlieren light sources at various angles with the optical centerline. The cutoff grid is a photographic negative of the source grid and is located in a plane optically conjugate to it. The schlieren effect can be achieved with an appropriate adjustment on the cutoff grid to block a fraction of the light from reaching the image plane. With the convergence of the schlieren light beam between the source grid and the camera lens, a relatively narrow “plane of focus” can be reconstructed in the vicinity of the image plane, and refractive disturbances outside this “plane of focus” are too blurred to be registered in the image. A simple lens is placed at the image plane to focus the light into the high-speed camera. This configuration provides a depth of focus of about  $\pm 4$  cm.



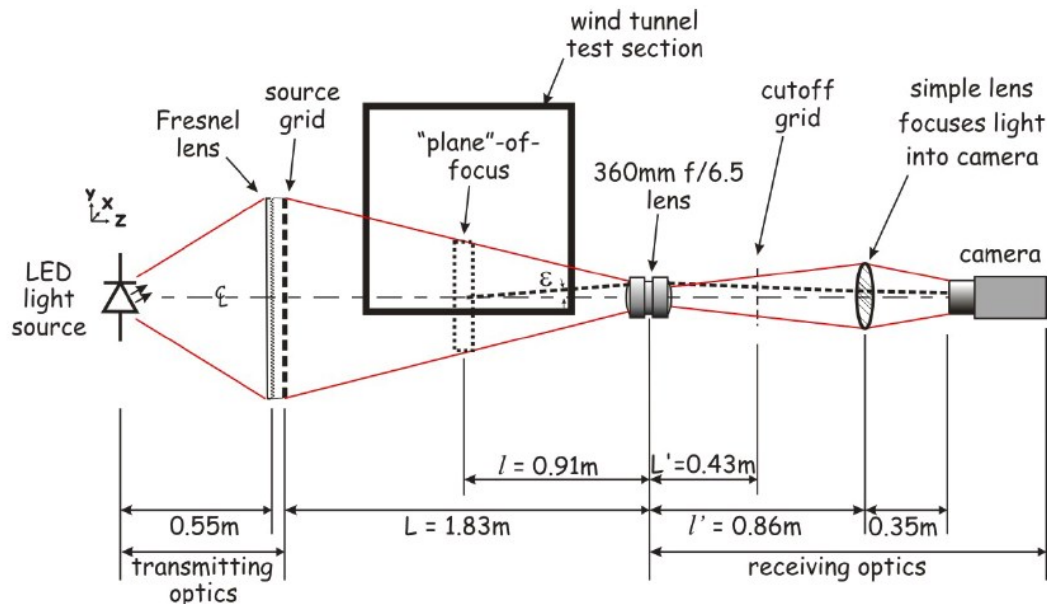


**Figure 4-1 Schematic of focusing schlieren imaging optics.**

#### **4.3. Double Focused Laser Differential Interferometry (FLDI)**

The FLDI<sup>65, 66, 67, 68, 69, 70</sup> is an optical technique which permits the high-speed and non-intrusive interrogation of small amplitude density perturbations at a small probe volume. In Smeets,<sup>67</sup> Figure 3 depicts the use of a Koester prism (an assembly of two identical right angle prisms) to separate a single FLDI bundle into two FLDI bundles. We refer to an FLDI bundle as the two orthogonally polarized laser beams that comprise one FLDI. In this work, we use a microscope slide placed at a prescribed angle so that approximately 1/3 of the FLDI beam is transmitted through the slide, and 2/3 of the FLDI beam is totally internally reflected and then transmitted through the slide. This setup results in a series of FLDI bundles that pass through the probe volume. The first totally internally reflected FLDI bundle has enough power to register sufficient SNR at a photodetector at the end of the beam path. The position and attitude of the microscope slide dictates the separation distance and orientation of the bundles relative to each other. A schematic of this FLDI setup is presented as Figure 4-2. In the shock tube experiments described in Section 4.4, the beam separation is 1620  $\mu\text{m}$  for the double FLDI setup. A similar setup has also been used in the Caltech T5 Hypervelocity Reflected Shock Tunnel<sup>71</sup> to measure disturbances in the boundary layer on a slender five degree half-angle sharp cone in one case, which was part of the test campaign described in Parziale<sup>72</sup> and Jewell.<sup>46</sup> In this case, presented in Section V, the two FLDI bundles are displaced approximately 1000 m from each other.

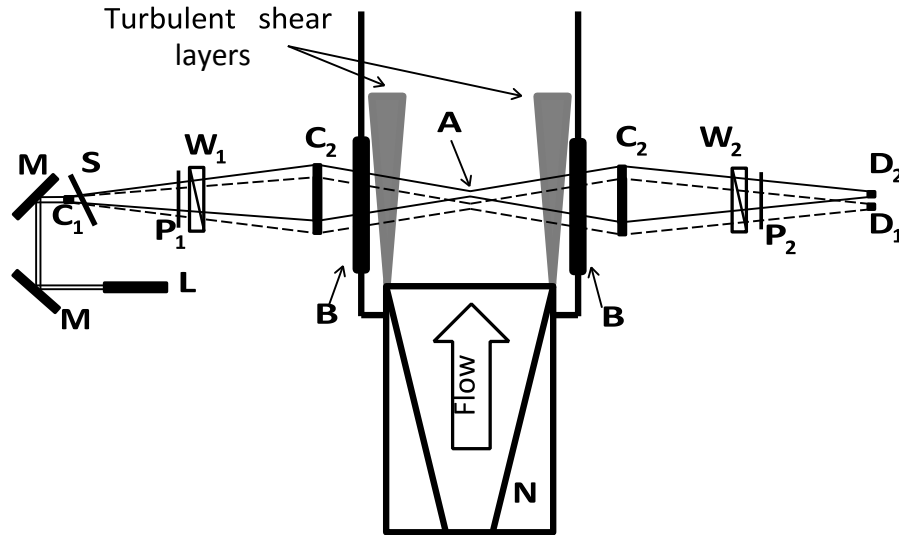


**Figure 4-2 Annotated schematic of the FLDI.**

Note for 4-2: L, Laser; M, mirror; C1, 10 mm focal length lens; C2, 300 mm focal length lens; P, polarizer; W, Wollaston prism (2 arc minutes); B, BK7 window; A, probe volume; D1 and D2, photodetectors; S, Microscope slide, N, nozzle. Solid and dashed lines are used to denote the separated FLDI bundles.

#### **4.4. Shock Tube Focusing schlieren and FLDI Results**

Single and double FLDI experiments, to compare FLDI-measured velocities with flowfield features of known velocity (such as shock waves) as well as to measure phase speeds or convective velocities of disturbances with unknown velocities (such as disturbances that may be present in the regions after the initial or reflected shock), are performed in a stainless steel shock tube at the U.S. Air Force Research Laboratory (AFRL) at Wright-Patterson Air Force Base, Ohio. The shock tube is comprised of a 4 m driven section and a 1 m driver section, with an inner diameter of 9.72 cm, as shown in rendered form in Figure 4-3 and schematically in Figure 4-4. A pair of flat fused-silica windows is mounted on the wall of the shock tube at a location of 82 cm from the driven section's end wall, to allow for optical imaging of the flow field. Three Kulite pressure transducers are installed in the wall over the last 1 m of the driven section to measure the traveling time of the shock front, and another Kulite pressure transducer is used as a flush-mounted Pitot probe mounted in a cylindrical tube, and positioned on the shock tube centerline near the center of the window through which the optical methods gain access. The FLDI sensor is positioned directly in front of the Pitot probe for FLDI experiments, and the camera is centered at this same location for the focusing schlieren experiments.

Prior to the experiment, both driver and driven sections are pumped down by a vacuum pump. In the present study, the driven section is filled up to 88, 123, and 142 Torr of air in separate double FLDI experiments, and 148, 292, and 446 Torr of air for matched pairs of experiments with single FLDI and focusing schlieren. This is followed by pressurizing the driver section with air until the breakage of the diaphragm. Once the diaphragm breaks, a shock wave is formed and travels along the driven section at (for example, for the 123 Torr condition)  $M_s = 1.6$  and  $V_s \approx$

519 m/s. The pressure behind the incident shock wave increases by a factor of 2.8 nearly instantaneously, and the shock-heated gas lags behind the shock wave at a velocity of  $\sim 264$  m/s.



**Figure 4-3 AFRL shock tube rendering.**

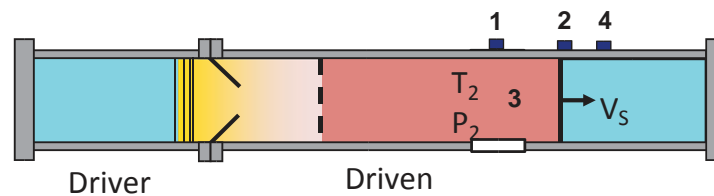


**Figure 4-4 AFRL shock tube schematic, with locations indicated for wall pressure transducers 1, 2, and 4, and Pitot transducer 3**

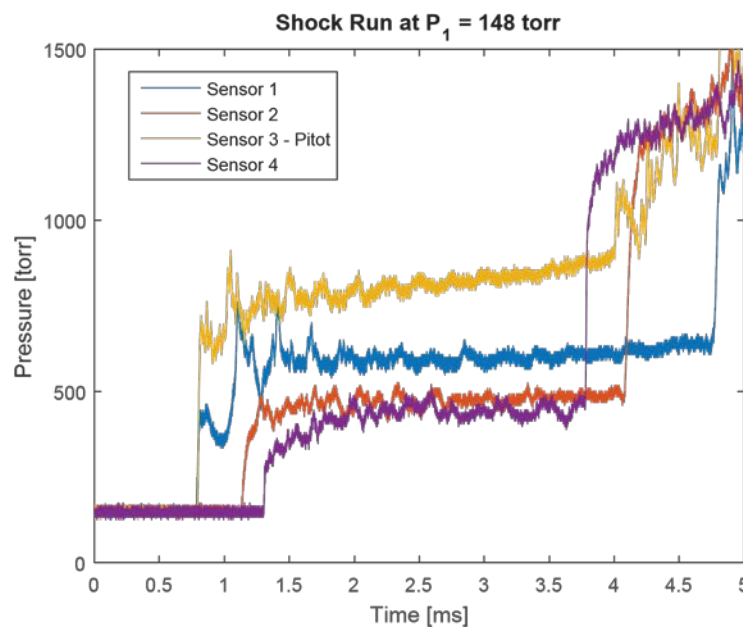


**Figure 4-5 Pressure data, including Pitot, from a typical shock tube experiment. The transducer locations are indicated in Figure 4-3.**

The shock wave then arrives at the end wall of the driven section and is reflected, causing another step change in temperature and pressure behind the reflected shock wave.

Figure 4-5 presents an example of the pressure signals acquired during a typical shock tube run.

Figure 4-6 shows a schlieren image of the shock-heated gas moving towards the driven section's end wall (from right to left). It appears that the flow is not perfectly uniform at this location, which might be attributed to the edge effect from the flat windows. Note that the width of the reflected shock front is supposed to be rather thin (within a few mean free paths). However, the measured shock front appears fairly thick or multi-valued, again possibly due to the effect of the flat windows, though the focusing schlieren should ensure that the signal received is disproportionately from the centerline.

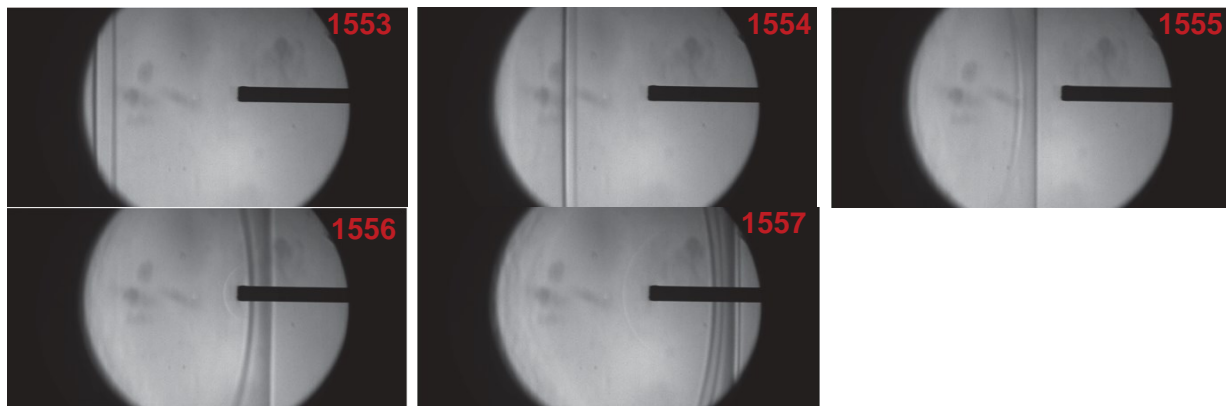


**Figure 4-6 Focusing schlieren images from five successive frames of incident shock propagation for a shock tube experiment. The Pitot probe is visible as a shadow.**

Turbulent structures are observed in the frames subsequent to the shock passage. For analysis at high frame rate (900,000 fps with shutter time  $1/1,260,000$  s), a small window of 128 by 56 pixels is selected directly in front of the Pitot probe, from which a small 4 by 4 subset, as depicted in Figure 4-7, is selected for frequency and velocity analysis. The shock speed is also directly measured by correlating these two signals. For the 148 Torr case, the incident shock speed was measured at 710.8 m/s with the focusing schlieren (the value from the transducers was 769 m/s); for the 292 Torr case, the incident shock speed was measured at 627.2 m/s with the focusing schlieren (the value from the transducers was 612 m/s); and for the 446 Torr case, the incident shock speed was measured at 561.2 m/s with the focusing schlieren (the value from the transducers was 557 m/s). The focusing-schlieren derived shock speed varies by less than 7% in all cases from that measured using the pressure transducers (e.g. in Figure 4-5).

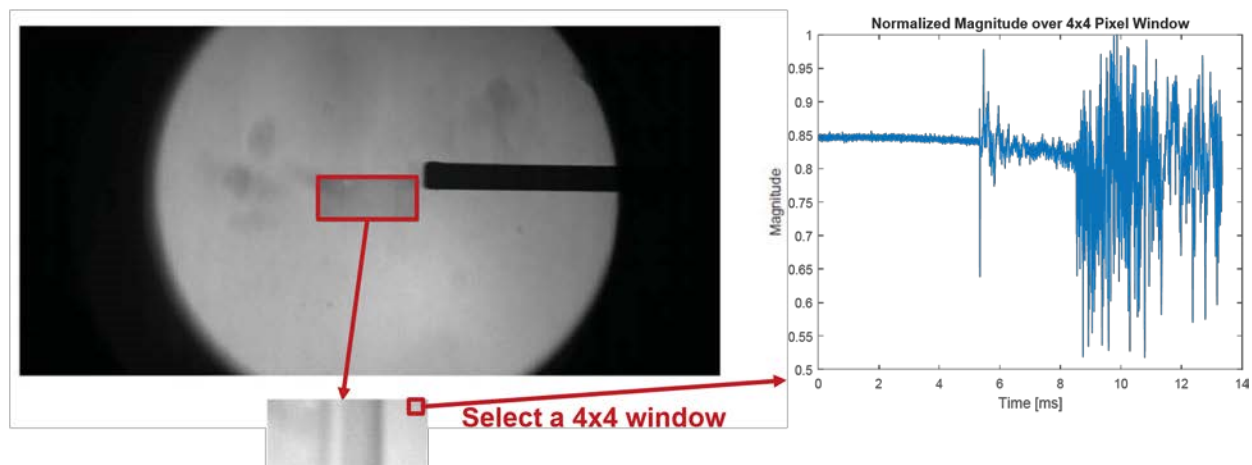
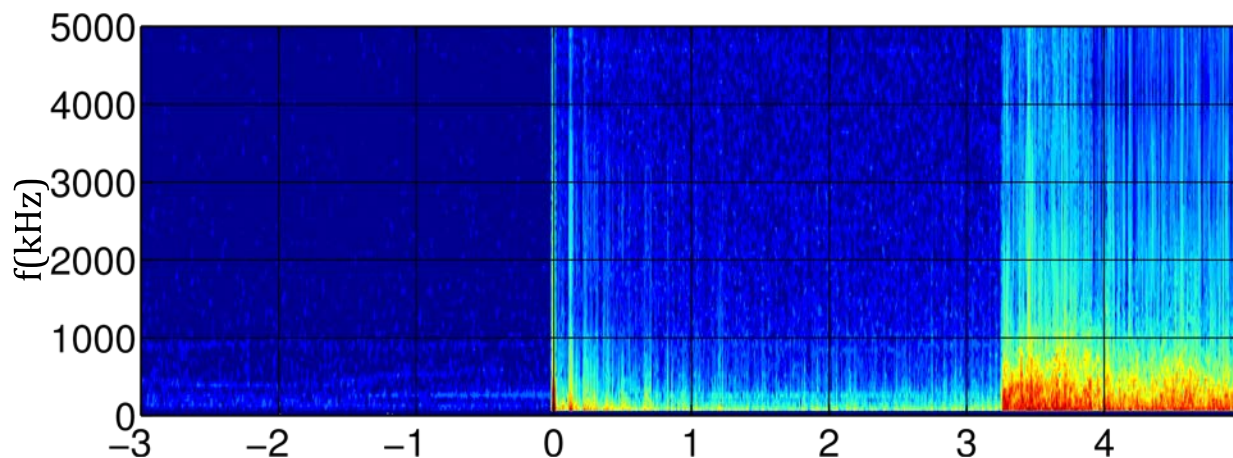


Figure 4-7 4x4 Window

Note for 4-7: A small window of 128 by 56 pixels is selected directly in front of the Pitot probe, from which a small 4 by 4 subset is selected for frequency analysis. For cross-correlation, a second 4 by 4 window (not pictured) on the far left side of this small window is selected.

A spectrogram (in arbitrary units calculated with the initial fill density) of a similar shock tube experiment, derived from a single-beam FLDI signal recorded at 20 MHz, is presented in Figure 4-8. The incident shock wave passes at the 0 ms point, with broadband disturbance across the entire spectrum, while frequency content after the shock is mostly limited to the range less than 1000 kHz. At 3.2 ms the reflected shock passes again across the sensitive region, with a similar but stronger broadband signal due to the increased density, and again followed by a region of primarily disturbances in the relatively low frequency range.



**Figure 4-8 FLDI spectrogram for a shock tube experiment, arbitrary units calculated with the initial fill density. The time scale is in milliseconds.**

A cross-correlation of double FLDI signals was performed for several shock tube conditions. The post-reflected shock region (similar to that observed after 3.2 ms in Figure 4-8, but in double FLDI experiments) contained coherent structures aligned along the long axis of the shock tube, which is the necessary orientation for FLDI sensitivity. An example of these cross-correlated

results, which are used together with the beam separation to calculate phase velocities across the entire signal with several different window sizes, are presented in Figure 4-9 compared with a Pitot signal recorded simultaneously just downstream of the FLDI to indicate the reflected shock region, from about 2 to 4 ms. A phase velocity of about -400 m/s is observed in the reflected shock region (from about 2 to 4 ms) for all window sizes; however, outside of this region no coherent structures strong enough to reliably cross-correlate were detected, as the random distribution of cross-correlated phase speeds indicate. It is possible that structures also exist in the other regions, but not in the sensitive orientation for the FLDI, or that the signal to noise ratio is not strong enough in the other regions. However, significant improvements in signal to noise ratio should be possible with the use of specialized optics for splitting the sensor bundles, rather than a glass slide.

Figure 4-10 presents a comparison of single FLDI and focusing schlieren signals and power spectral density. These results were obtained from two separate experiments performed at nearly the same conditions (estimated variability was 5%). Good agreement is observed in PSD rolloff between the two measurements at 148 Torr out to the limit of the focusing schlieren's Nyquist frequency in this case, and also in the other two pairs experiments, at 292 and 446 Torr (not pictured).

#### **4.5. Double FLDI Boundary Layer Results**

In Figure 4-11, we present the short time Fourier transform of the FLDI response for the upstream bundle (registered by D1 in Figure 2). In that signal, we observe narrow-band response that is consistent with the "Mack" or second mode.<sup>53, 73, 74</sup> An example of narrow-band response (NBR) is indicated in Figure 4-11, as well as an example of broad-band response (BBR).

The narrow-band response, marked by NBR, at approximately 1800 s in Figure 4-11 is of interest. A 24 s window about this wavepacket is presented as a spectrogram in Figure 4-12-left. Moreover, we present the upstream and downstream responses of the double FLDI system as Figure 4-12-top. The traces look very much the same, except they are slightly displaced in time. The local extrema are found with signal processing in MATLAB. The difference in time, or delay, is then found for the peaks (unfilled circles) and troughs (filled circles) as reported in Figure 12-bottom. Because the delay and the length ( $\approx 1000 \mu\text{m}$ ) between the detectors is known, a velocity scale can be found; this velocity scale is the local phase speed. Upon inspecting Figure 4-12 bottom, the average delay is approximately 0.4 s, so the local phase speed is approximately 2.5 km/s. This is approximately 80% of the edge velocity.

Trends in the structure of Figure 4-12-bottom are apparent. The phase speed appears to vary depending on the location within a wave-packet and the stage at which it passes through the FLDI probe volumes, but further investigation will be required to confirm this effect.

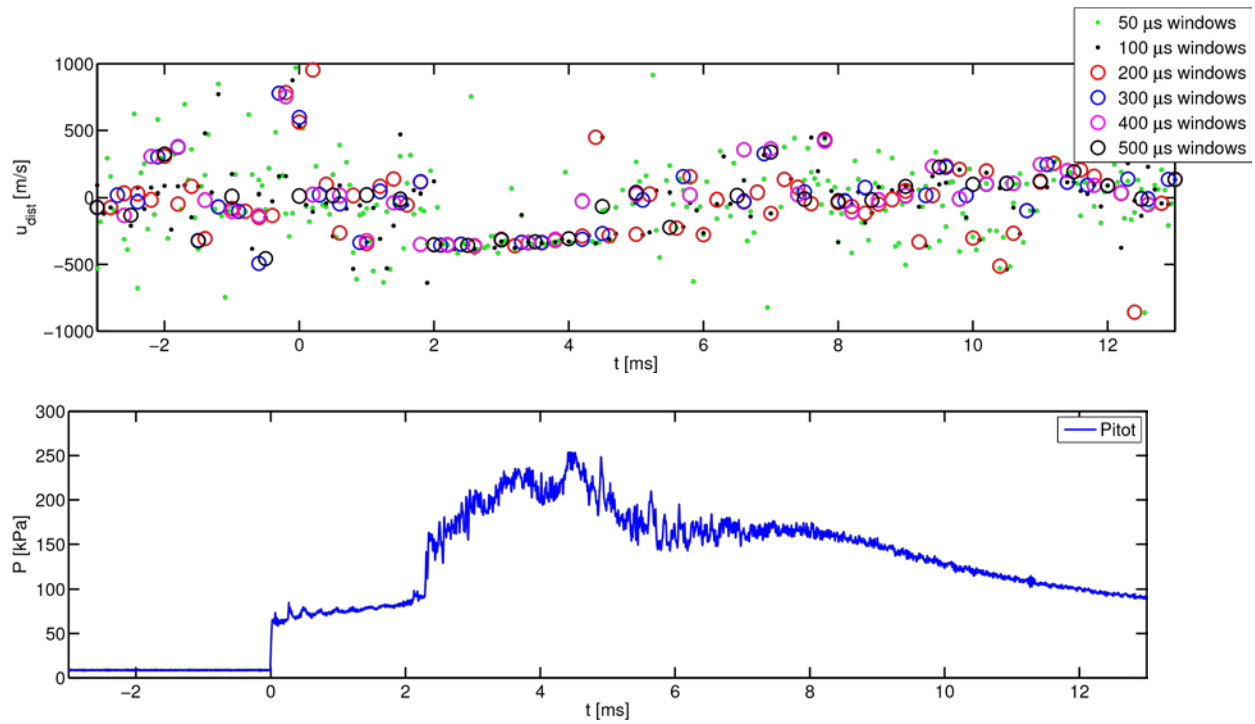


**Figure 4-9 Cross-correlation of double FLDI signals for one shock tube experiment, compared with simultaneous Pitot measurements recorded just downstream.**

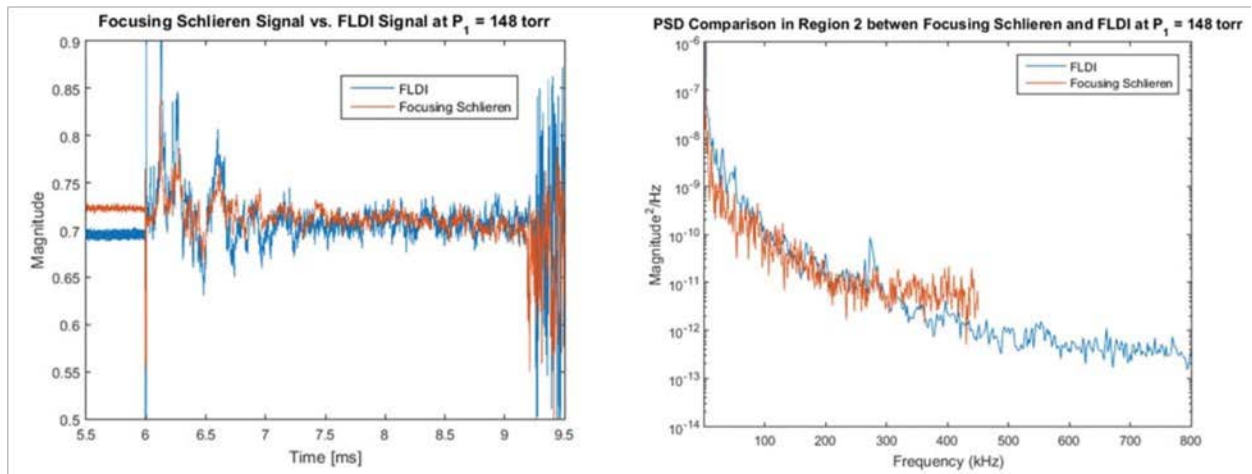


**Figure 4-10 FLDI and focusing schlieren signals (left) and power spectral density (right) compared.**



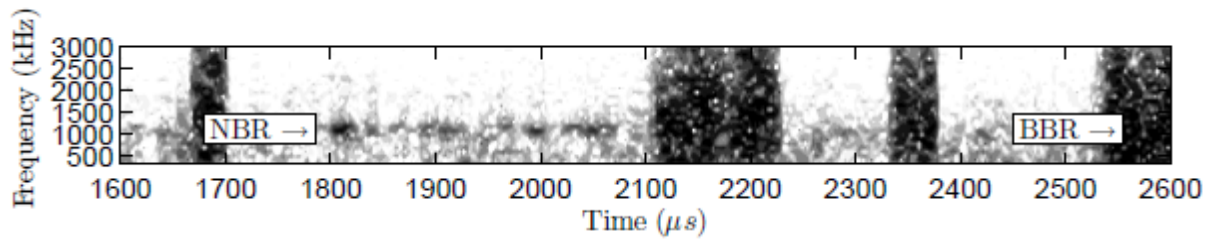


**Figure 4-11** Arbitrary logarithmic units of change in density, the spectrum is estimated by the short time Fourier transform. Darker shading indicates larger amplitude.

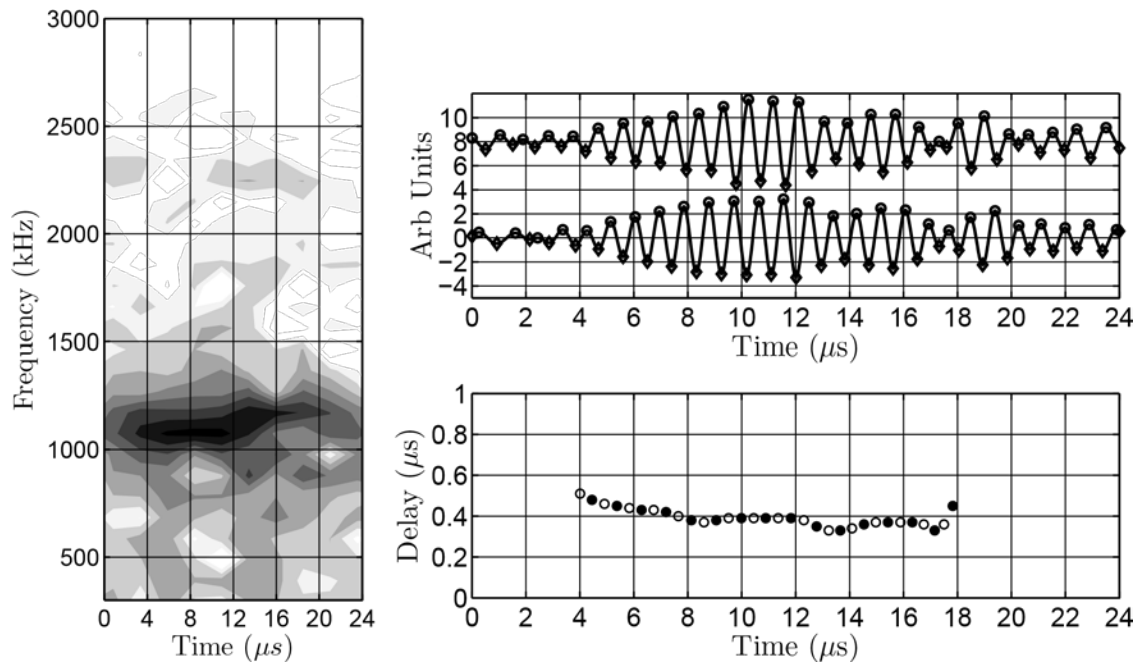


**Figure 4-12** FLDI Frequency and Time

Note for 4-12: Left: Zoomed in spectrogram around 24 s of the narrow-band disturbance indicated at approximately 1800 s by NBR in Figure 11. Top: Upstream and downstream FLDI responses recorded by detectors D1 and D2 in Figure 4-2. Bottom: The delay in s of the upstream and downstream response for the peaks (unfilled circles) and troughs (filled circles).

**Table 4-1** Summary of reservoir and edge conditions for shot 2821 in 50% CO<sub>2</sub>, 50% air by mass. For further details on this condition see Jewell and Shepherd.<sup>75</sup>

Shot	$h_{res}$ (MJ/kg)	$P_{res}$ (MPa)	$U_e$ (m/s)	$P_e$ (kPa)	$T_e$ (K)	$Tv_e$ (K)	$\rho_e$ (kg/m <sup>3</sup> )	$M_e$ (-)	unit $Re_e$ (1/m)
2821	6.70	42.5	3063	37.2	1362	1362	0.110	4.46	$7.23 \times 10^6$



## **5. Development of High-Speed Schlieren System for the New AFRL Mach-6 Ludwig Tube Hypersonic Wind Tunnel**

### **5.1. Background**

Several researchers<sup>76,77,78,79,80</sup> have implemented high-speed schlieren imaging techniques (using both conventional and focused methods) to investigate the development of second-mode instability waves in the hypersonic boundary layer of a slender cone in conventional wind tunnels. These second-mode waves can be observed as “ropelike” structures in the schlieren images.<sup>76</sup> The propagation speed of these second-mode waves can be determined by applying image-correlation techniques to image pairs in which such wave packets appear. In addition, wavenumber spectra can be obtained from the images by performing the Fourier transform of the intensity profile of a row of pixels at a given height above the cone surface. These can then be converted to frequency spectra using the previously-determined propagation speed.

This paper shows some preliminary imaging results during the start-up process in a new AFRL Mach-6 Ludwig tube hypersonic wind tunnel using the high-speed schlieren technique. In addition, frequency spectrum during the run is inferred from the high-speed images in order to characterize the tunnel noise. Finally, this paper shows some preliminary imaging results for boundary layer transition on a flat plate, and the frequency spectra at various streamwise locations are obtained from the high-speed images.

### **5.2. Experimental Setup**

#### *Ludwig Tube Setup*

A new AFRL Mach-6 Ludwig tube hypersonic wind tunnel has been constructed to operate at Mach 6 with unit Reynolds numbers of  $2 \times 10^6/\text{ft} - 10^7/\text{ft}$ , as shown in Figure 5-1. Various starting methods exist for this wind tunnel, including a fast-opening plug-type valve. Although the fast-valve is intended to be the primary starting method for this wind tunnel, the tunnel was also designed to be capable of operation with diaphragms. The fast-valve provides very rapid turnaround between runs (5-10 minutes), but presents some drawbacks compared to the diaphragm, including a finite actuation time and the presence of a center-body and supports upstream of the nozzle. Therefore, numerous diaphragm runs have been made to provide a baseline performance reference with very rapid actuation and little or no blockage upstream of the nozzle. Metal diaphragms (e.g., aluminum or steel) were used. During the test run, the diaphragm petals when a substantial pressure difference between the driver section and the test section has been achieved. This paper shows some preliminary imaging results (i.e., starting shock and start-up process) using the high-speed schlieren system. Laminar-turbulent transition experiments will be performed in the near future (once the tunnel condition is fully characterized). Other optical diagnostic techniques (e.g., 10 Hz Kr PLIF and focused laser differential interferometry), along with the high-speed schlieren system, will be employed to better understand the transition behavior in the hypersonic boundary layer (e.g., intermittency and the growth of second-mode waves).



**Figure 5-1 AFRL Mach-6 Ludwieg Tube Hypersonic Wind Tunnel.**

A Pitot rake is installed at the test section in order to characterize the flow conditions. Four Kulite pressure sensors are installed on the Pitot rake and were used to measure the stagnation pressures ( $P_{t2}$ ) behind the bow shock. Three of these sensors are flush-mounted onto the surface. The fourth sensor protrudes from the front of the rake in a conventional probe, as illustrated in Figure 5-2.

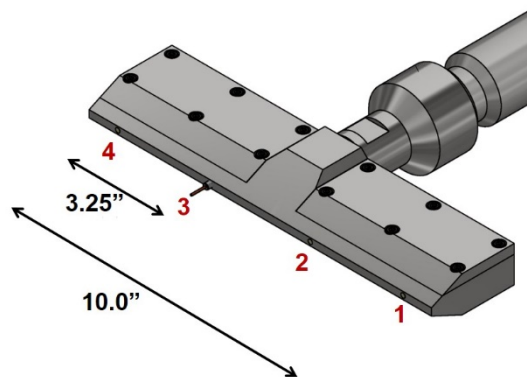


**Figure 5-2 Schematic of Pitot rake at the test section.**

In addition, there are a series of Kulite pressure sensors installed on the Ludwieg tube that are used to characterize the flow conditions of the tunnel and to determine the flow Mach number. Figure 5-3 shows the pressure time histories for three sensors, namely nozzle entrance pressure ( $P_{t1}$ ), nozzle exit pressure ( $P_t$ ), and Pitot pressure sensor 3 ( $P_{t2}$ , the sensor protruding from the surface), for the 90 psi stagnation pressure test run. The stagnation temperature was  $T_t = 450$  F for all runs. As illustrated in Figure 5-3, once the tunnel starts, a nearly uniform pressure region can be achieved over a period of 100 ms. Shortly after this quasi-steady period, a small pressure drop at  $t \approx 120$  ms is observed due to the arrival of the expansion fan reflected from the driver end wall, followed by another 100-ms quasi-steady period. After that, the tunnel unstarts at  $t = 240$  ms. Note that the nozzle exit pressure appears to be quite noisy during this run, which can be attributed to its rather low pressure readings.

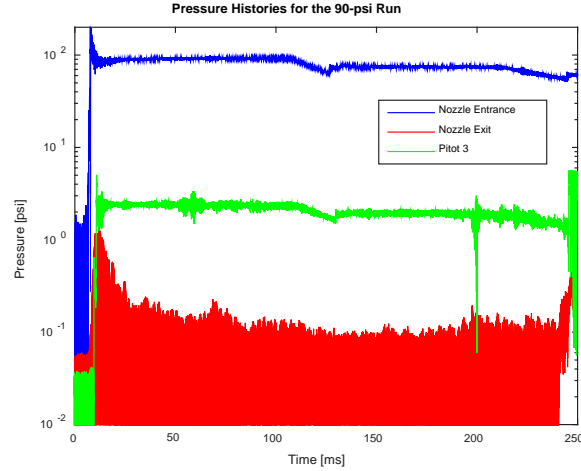


**Figure 5-3 Pressure time histories at nozzle entrance, nozzle exit, and Pitot rake.**

The flow Mach number can be determined using the normal shock relation:

$$\frac{P_{t2}}{P_{t1}} = \left[ \frac{(\gamma+1)M_1^2}{(\gamma-1)M_1^2+2} \right]^{\frac{\gamma}{\gamma-1}} \left[ \frac{\gamma+1}{2\gamma M_1^2-(\gamma-1)} \right]^{\frac{1}{\gamma-1}} \quad (1)$$

Figure 5-4 shows the computed Mach number using Eq. (1), and the computed flow Mach number is found to be about 6.20 for this 90 psi test run. Note that a large spike occurred at 200 ms (as illustrated in Figure 5-3 and Figure 5-4), which can be attributed to the particle impact on the Pitot sensor.

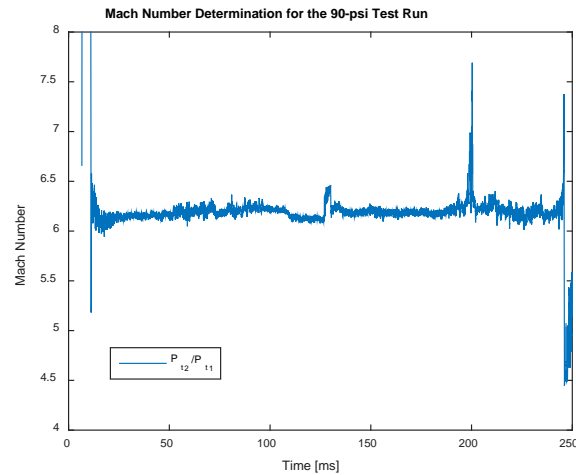


**Figure 5-4 Mach number determination for the 90 psi run.**

### High-Speed Schlieren System

The current system is a Z-type schlieren configuration, consisting of a pair of matched high f/#, large diameter parabolic mirrors (12.5 in dia. × 75 in focal length with a surface accuracy of  $\lambda/8$ )

and a set of flat mirrors (with a surface accuracy of  $\lambda/10$ ). These components were purchased from Edmund Optics. Long focal-length parabolic mirrors are preferred in order to enhance the schlieren sensitivity ( $S$ ), governed by:<sup>63,81</sup>

$$S = \frac{f_2}{a} = \frac{f_2}{b\left(1 - \frac{\%cutoff}{100}\right)} \quad (2)$$

A 200 W QTH lamp with a condenser lens and a 1.5-mm wide vertical slit was used as an extended light source in the present study. Note that we have recently purchased a 1000 W Mercury-Xenon arc lamp from Newport, and we are planning to replace the 200 W QTH lamp with the arc lamp. In addition, Photron SA-Z camera with a 180-mm FL camera lens was used to register the schlieren images in this study. A vertical cutoff was also selected to enhance the schlieren sensitivity in the horizontal direction.

### 5.3. Results and Discussion

#### *Schlieren Imaging Results for the Start-up Process During the 90 psi Run*

A pair of fused silica windows were installed on both sides of the test section to allow for imaging the flow interaction with the Pitot rake. For the 90 psi test run, the frame rate of the Photron SA-Z camera was set at 30,000 fps with a shutter time of 2.5  $\mu$ s. The pixel window area was set at 1024 $\times$ 688, which covered an observation area with a diameter of 8.375 in. Note that the pixel resolution is 0.195 mm/pixel. Figure 5-5 shows the starting shock traversing from right to left (starting from frame 1 to frame 7). Note that each frame interval represents a time interval of 33.3  $\mu$ s. Hence, it takes about 0.20 ms for the starting shock to travel a distance of approximately 8.375 in, and the starting shock speed is estimated to be approximately 1064 m/s. In particular, frames 4-7 show the interaction between the starting shock and the Pitot rake, and the reflected shock from the rake. It should also be noted that there is some small anomaly in one of the fused silica windows, which creates a blur at the lower right corner on each image.

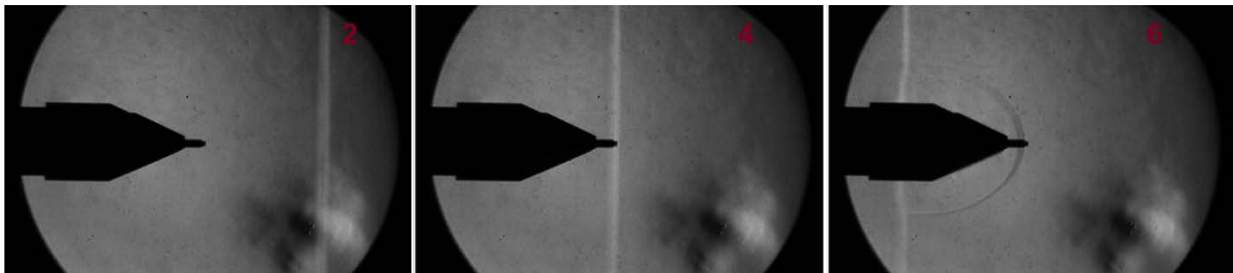


**Figure 5-5 Movement of the starting shock for the 90 psi run.**

Figure 5-6 illustrates some major events in the start-up process for the 90 psi test run. Waves are evident around the rake on frame 42. Shortly after, a wave appears on frame 44 and disappears after frame 52. Hence, the speed of the wave is about 798 m/s, which is on the same order of magnitude as the gas speed, consistent with the wave being a contact surface. According to these schlieren images, the tunnel appears to fully start on frame 57, and the entire

start-up process takes about 1.77 ms (53 frame intervals) since the arrival of the starting shock at the Pitot sensor 3.

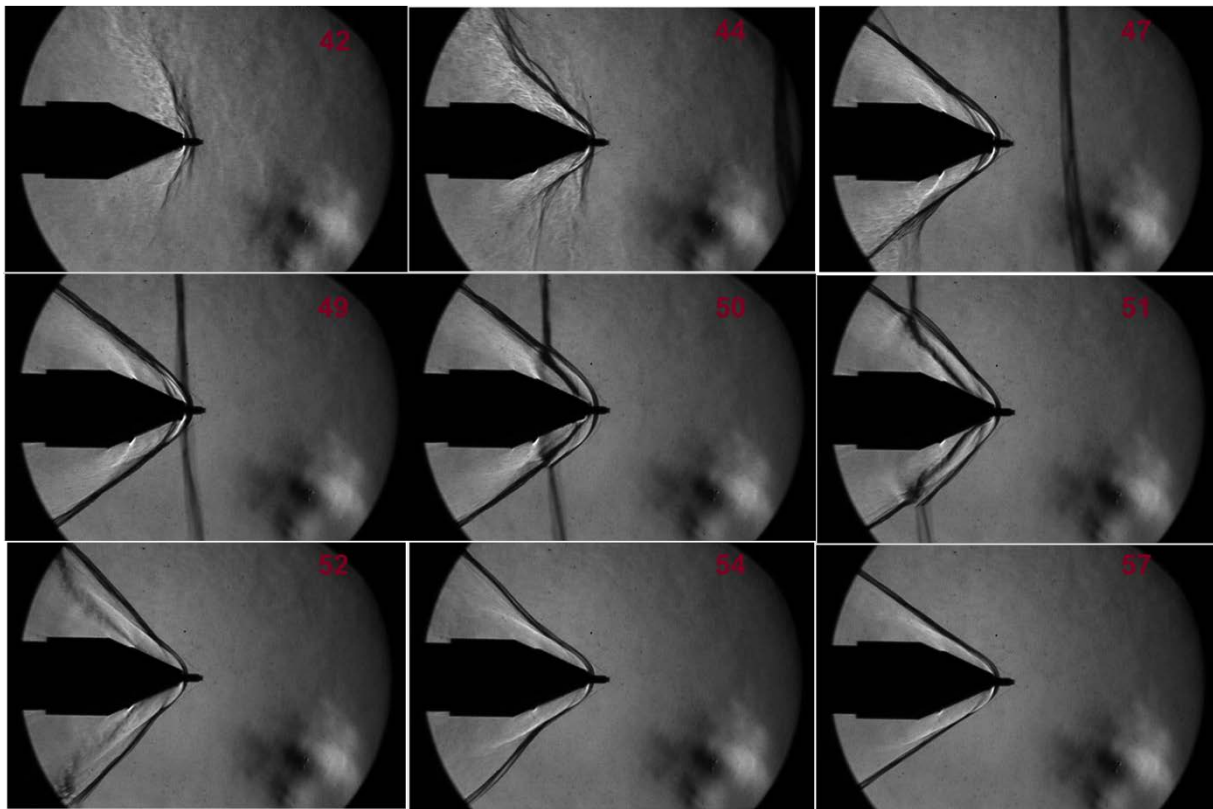


**Figure 5-6 Sample frames during the start-up process for the 90 psi run.**

Figure 5-7 shows the Pitot pressure time history for the 90 psi test run, and four events have been marked on the trace that correspond to particularly interesting frames during the start-up process. On Frame 4, the starting shock has just arrived at Pitot sensor 3, thereby increasing the pressure significantly. In frame 42, a shock begins to form in front of Pitot sensor 3. After another time interval of 0.27 ms, the contact surface arrives at the sensor on frame 49, and pressure decreases. Finally, the tunnel appears to fully start 1.77 ms after the arrival of starting shock at the Pitot sensor, as illustrated in frame 57.

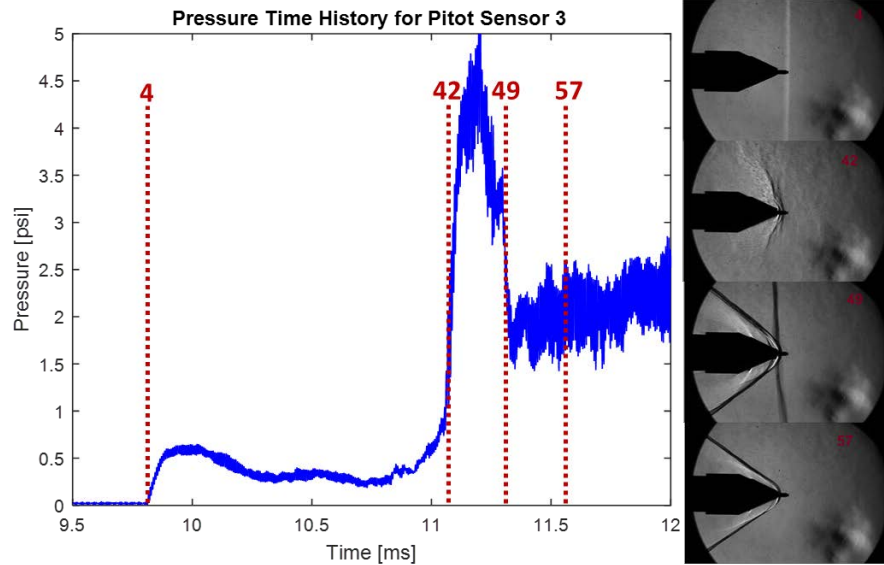


**Figure 5-7 Pressure time history for Pitot sensor 3 (marked with 4 major events) for the 90 psi run.**

#### Spectral Analysis on Schlieren Images

For hypersonic flow, the 2<sup>nd</sup> mode instability is quite susceptible to the tunnel noise via receptivity mechanisms, thereby affecting the transition location significantly. Hence, it is particularly crucial to characterize the tunnel noise (i.e., acoustic noise originated from the tunnel's nozzle wall boundary layer) prior to any boundary-layer transition experiments. In the present study, we attempt to use the schlieren images to characterize the tunnel noise based on the density gradient approach. The Pitot rake was placed in a vertical orientation for this set of experiments. Figure 5-8 shows a sample schlieren image for the Pitot rake in the vertical orientation during the 295 psi run. Note that there are some particle impacts on the Pitot rake during the run, as illustrated in Figure 5-8. Additionally, a small bow shock is formed upstream of the Pitot sensor 3, and is merged with the primary bow shock originated from the rake.

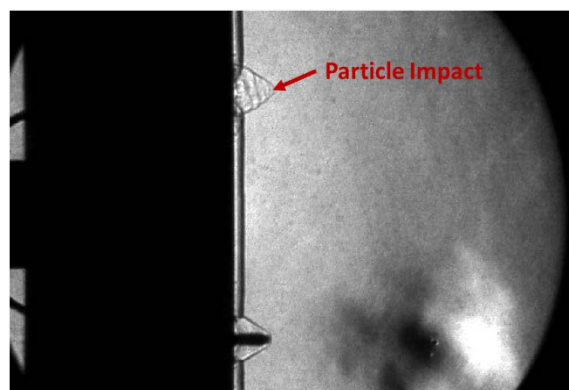


**Figure 5-8 Schlieren image for the Pitot rake in the vertical orientation.**

To obtain the higher-frequency components within the flowfield, a higher frame rate from the camera is needed. Hence, a much smaller pixel window area of  $128 \times 56$  with a frame rate of 900,000 fps and a shutter time of 794 ns was selected in order to obtain the frequency spectrum of the flowfield. This smaller pixel window area covered most of the regions around Pitot sensor 3, along with the region upstream of the bow shock. Figure 5-9 shows the normalized schlieren signal over a small region downstream of the bow shock (averaged over a  $2 \times 2$  pixel window) for the 375 psi test run (at  $T_t = 450$  F). The tunnel starts at around 100 ms, and the schlieren signal becomes much noisier during the run as compared to the background. Additionally, there is a small signal drop at  $t = 210$  ms that corresponds to the arrival of the expansion fan reflected from the driver end wall, followed by another 100 ms quasi-steady period.

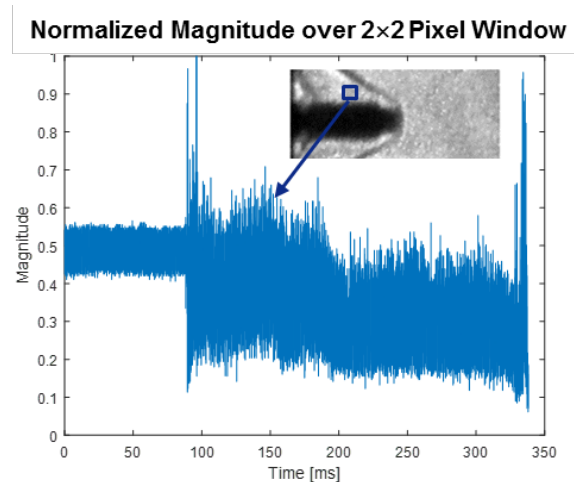


**Figure 5-9 Plot of normalized magnitude over a  $2 \times 2$  pixel window area over time for the 375 psi run.**

Power-spectral-density (PSD) analysis was then performed on the normalized schlieren signals during the 375-psi run. Figure 5-10 shows the frequency spectra in the regions upstream and downstream of the bow shock for the 375 psi run, along with the background spectrum. The spectral power of the schlieren signals during the run are clearly much larger than that of the background at frequencies less than 300 kHz. In particular, the spectral power in the region downstream of the bow shock is at least an order of magnitude larger than that in the region upstream of the bow shock. As expected, the tunnel noise is dominated by low frequency components (at frequencies less than 300 kHz).



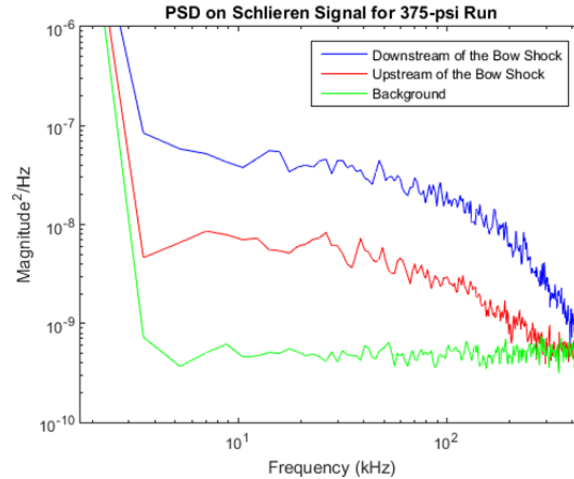


**Figure 5-10 Power-spectral-density (PSD) analysis on schlieren signals for the 375-psi run.**

### Spectral Analysis on a Flat Plate Experiment

This section presents some preliminary shadowgraph results for laminar-turbulent boundary layer transition on a flat plate with a sharp leading edge at an adiabatic wall temperature. The flat plate had a length of 10 in (or 25.4 cm). The experiments were conducted at the AFRL Mach-6 High Reynolds Number Facility. The nominal experimental conditions are  $P_t = 700$  psi and  $T_t = 900^\circ\text{R}$ , giving a unit Reynold number of  $Re = 1.3 \times 10^7/\text{ft}$  and a Mach number of 5.98. Figure 5-11 shows the sample shadowgraph image for this flat plate experiment (at the adiabatic wall temperature). Note that the pixel resolution is 0.24 mm/pixel.

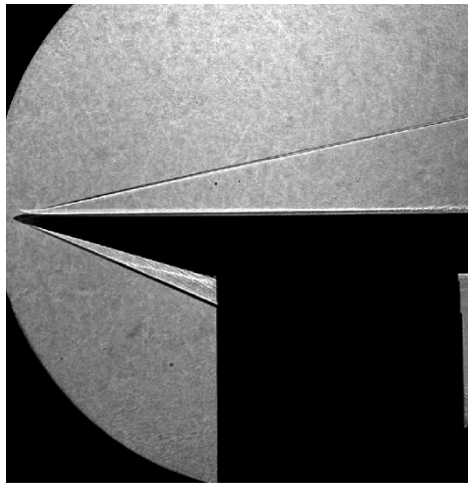


**Figure 5-11 Sample shadowgraph image for the flat plate experiment (at the adiabatic wall temperature).**

Similarly, a small pixel window of  $512 \times 24$  with a frame rate of 800,000 fps and a shutter time of 248 ns was selected to image the development of boundary layer on the flat plate over the region of 12.6-25.0 cm from the sharp tip. Figure 5-12 illustrates the development of boundary layer on



the flat plate. At a distance of 17.4 cm from the sharp tip, the boundary layer appears to be laminar. Shortly after, the boundary layer seems to undergo transition. It also appears that the boundary layer becomes fully turbulent by 22.2 cm. Figure 5-13 shows the PSD analyses on the shadowgraph images at various streamwise locations near the boundary layer edge. As the flow progresses downstream, there is an increase in spectral power. However, no distinct frequency peak associated with the second-mode wave can be identified.



**Figure 5-12 Shadowgraph image for laminar-turbulent boundary layer transition on the flat plate.**

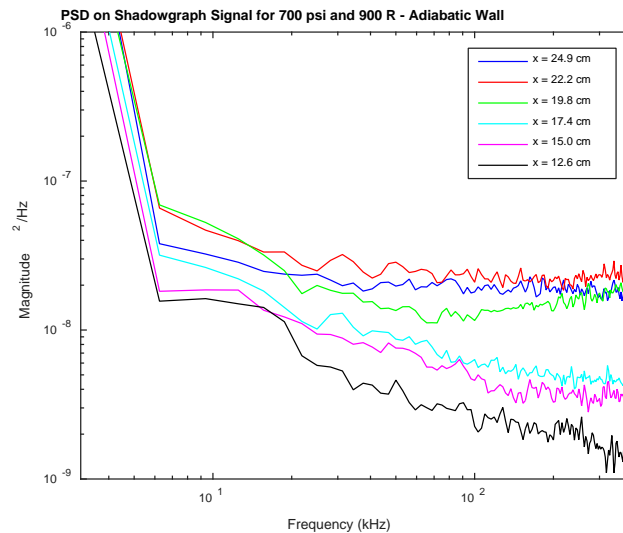


**Figure 5-13 PSD analysis on normalized shadowgraph signals for the flat plate experiment.**

## List of Acronyms, Abbreviations, Symbols

$A$  = disturbance amplitude, dimensionless  
 $a$  = width of unobstructed light source  
 $b$  = width of light-source image  
 $A_l$  = disturbance amplitude at lower neutral bound, dimensionless  
 $C_p$  = specific heat, J/(kg K)  
 $f$  = frequency or focal length, units as noted  
 $h$  = specific enthalpy, KJ/kg  
 $M$  = Mach number  
 $N = \ln[A(f)/A_l(f)]$ , dimensionless  
 $P$  = pressure, unites as noted  
 $p$  = pressure, units as noted  
 $P_t$  = Pitot pressure, units as noted  
 $R$  = radius, units as ntoed  
 $Re$  = unit Reynolds number per meter  
 $S$  = schlieren sensitivity  
 $T$  = temperature, K  
 $t$  = time, units as noted  
 $U$  = velocity, m/s  
 $u^*$  = friction velocity,  $\sqrt{\tau_w/\rho}$ , m/s  
 $X$  = streamwise coordinate  
 $x$  = streamwise coordinate, origin at model nose stagnation point, dimensions as noted  
 $y$  = spanwise coordinate, origin at model nose stagnation point, or coordinate normal to model wall, dimensions as noted  
 $y^+$  = distance from model wall,  $yu^*/\nu$ , non-dimensional  
 $\gamma$  = ratio of specific heats, dimensionless  
 $\nu$  = kinematic viscosity, m<sup>2</sup>/s  
 $\rho$  = density, kg/m<sup>3</sup>  
 $\tau$  = skin friction, Pa

**Subscripts**

$B$  = blunt

$e$  = conditions at edge of boundary layer

$N$  = nose

$S$  = sharp

$S_w$  = swallowing

$Tr$  = transition

$w$  = wall

$0$  = stagnation conditions

$1$  = conditions upstream of shock

$2$  = conditions downstream of shock, or at second mirror

$\infty$  = free stream, upstream of model bow shock

**Acronyms**

ACE	Actively-Controlled Expansion
AEDC	Arnold Engineering Development Center
AFRL	Air Force Research Laboratory
AoA	angle of attack
BAM6QT	Boeing/AFOSR Mach 6 Quiet Wind Tunnel
DFT	discrete Fourier transform
DPLR	Data Parallel-Line Relaxation
DRE	discrete roughness element
FL	focal length
FLDI	focused laser differential interferometer
fps	frames per second
HIFiRE	Hypersonic International Flight Research Experiments
IR	infrared
LED	light-emitting diode
LST	linear stability theory
NASA	National Aeronautics and Space Administration
PEEK	poly-ether ether ketone
PLIF	planar laser-induced fluorescence
PSD	power spectral density
PSE	parabolized stability equation
QTH	quartz-tungsten-halogen
RMS	root-mean-square
SNR	signal-to-noise ratio
TSP	temperature-sensitive paint

## References

- <sup>1</sup> Borg, M.P., and Kimmel, R. L., “Simultaneous Infrared and Pressure Measurements of Crossflow Instability Modes for HIFiRE-5,” AIAA paper 2016-0354, January 2016.
- <sup>2</sup> Jewell, J. S., and Kimmel, R. L., “Boundary Layer Stability Analysis for Stetson’s Mach 6 Blunt Cone Experiments,” AIAA paper 2016-0598, January 2016.
- <sup>3</sup> Jewell, J. S., Parziale, N. J., Lam, K.-Y., Hagen, B. J., and Kimmel, R. L., “Disturbance and Phase Speed Measurements for Shock Tubes and Hypersonic Boundary-Layer Instability,” AIAA paper 2106-3112, June 2016.
- <sup>4</sup> Malik, M. R., Li, F., and Choudhari, M., “Analysis of Crossflow Transition Flight Experiment Aboard the Pegasus Launch Vehicle,” AIAA paper 2007-4487, June 2007.
- <sup>5</sup> Malik, M., Li, F., and Chang, C.-L., “Crossflow disturbances in three-dimensional boundary layers: nonlinear development, wave interaction and secondary instability,” *Journal of Fluid Mechanics*, Vol. 268, 1994, pp. 1–36.
- <sup>6</sup> Saric, W. S. and Reed, H. L., “Crossflow Instabilities- Theory & Technology,” AIAA paper 2003-0771, Jan. 2003.
- <sup>7</sup> Bippes, H., “Basic experiments on transition in three-dimensional boundary layers dominated by crossflow instability,” *Progress in Aerospace Sciences*, Vol. 35, 1999, pp. 363–412.
- <sup>8</sup> Corke, T. and Knasiak, K., “Stationary-traveling cross-flow mode interactions with periodic distributed roughness,” AIAA paper 96-2016, June 1996.
- <sup>9</sup> Bippes, H. and Lerche, T., “Transition Prediction in Three-Dimensional Boundary-Layer Flows Unstable to Crossflow Instability,” AIAA paper 97-1906, June 1997.
- <sup>10</sup> White, E. B. and Saric, W. S., “Secondary instability of crossflow vortices,” *Journal of Fluid Mechanics*, Vol. 525, 2005, pp. 275–308.
- <sup>11</sup> Carpenter, M. H., Choudhari, M., Li, F., Streett, C. L., and Chang, C.-L., “Excitation of Crossflow Instabilities in a Swept Wing Boundary Layer,” AIAA paper 2010-0378, January 2010.
- <sup>12</sup> Eppink, J. and Wlezien, R., “Observations of traveling crossflow resonant triad interactions on a swept wing,” AIAA paper 2012-2820, June 2012.
- <sup>13</sup> Saric, W. S. and Reed, H. L., “Supersonic Laminar flow control on swept wings using distributed roughness,” AIAA paper 2002-0147, Jan. 2002.
- <sup>14</sup> King, R., “Three-dimensional boundary-layer transition on a cone at Mach 3.5,” *Experiments in Fluids*, Vol. 13, No. 4, 1992, pp. 305–314.

- <sup>15</sup> Beeler, G. B., Wilkinson, S. P., Balakumar, P., and McDaniel, K. S., "Crossflow instability on a wedge-cone at Mach 3.5," Paper 2012-2825, AIAA, June 2012.
- <sup>16</sup> Poggie, J., Kimmel, R. L., and Schwoerke, S. N., "Traveling Instability Waves in a Mach 8 Flow over an Elliptic Cone," *AIAA Journal*, Vol. 38, No. 2, 2000, pp. 251–258.
- <sup>17</sup> Choudhari, M., Chang, C.-L., Jentink, T., Li, F., Berger, K., Candler, G., and Kimmel, R., "Transition Analysis for the HIFiRE-5 Vehicle," AIAA paper 2009–4056, June 2009.
- <sup>18</sup> Swanson, E. O. and Schneider, S. P., "Boundary-layer transition on cones at angle of attack in a Mach-6 quiet tunnel," AIAA Paper 2010-1062, January 2010.
- <sup>19</sup> Craig, S. A. and Saric, W. S., "Experimental study of crossflow instability on a Mach 6 yawed cone," AIAA paper 2015–2774, June 2015.
- <sup>20</sup> Ward, C. A., Henderson, R. O., and Schneider, S. P., "Possible secondary instability of stationary crossflow vortices on an inclined cone at Mach 6," AIAA paper 2015–2773, June 2015.
- <sup>21</sup> Dinzl, D. J. and Candler, G. V., "Analysis of crossflow instability on HIFiRE-5 using direct numerical simulation," AIAA paper 2015–0279, June 2015.
- <sup>22</sup> Kimmel, R. L. and Poggie, J., "Transition on an Elliptic Cone at Mach 8," American Society of Mechanical Engineers ASME FEDSM97-3111, June 1997.
- <sup>23</sup> Kimmel, R. L. and Poggie, J. J., "Three-Dimensional Hypersonic Boundary Layer Stability and Transition," WL-TR-97- 3111, Air Force Research Laboratory Technical Report, Wright-Patterson Air Force Base, Ohio, Dec. 1997.
- <sup>24</sup> Kimmel, R. L., Poggie, J. J., and Schwoerke, S. N., "Laminar-Turbulent Transition in a Mach 8 Elliptic Cone Flow," *AIAA Journal*, Vol. 37, No. 9, September 1999, pp. 1080–1087.
- <sup>25</sup> Borg, M. P., Kimmel, R. L., Hofferth, J. W., Bowersox, R. D., and Mai, C. L., "Freestream effects on boundary layer disturbances for HIFiRE-5," AIAA Paper 2015-0278, January 2015.
- <sup>26</sup> Borg, M. P., Kimmel, R. L., and Stanfield, S. A., "Traveling crossflow instability for the HIFiRE-5 elliptic cone," *Journal of Spacecraft and Rockets*, Vol. 52, No. 3, May–June 2015, pp. 664–673.
- <sup>27</sup> Borg, M. P., Kimmel, R. L., and Stanfield, S., "Crossflow Instability for HIFiRE-5 in a Quiet Hypersonic Wind Tunnel," Paper 2012-2821, AIAA, June 2012.
- <sup>28</sup> van den Kroonenberg, A., Radespiel, R., Candler, G., and Estorf, M., "Infrared measurements of boundary-layer transition on an inclined cone at Mach 6," AIAA paper 2010-1063, January 2010.

- <sup>29</sup> Muñoz, F., Heitmann, D., and Radespiel, R., “Instability Modes in boundary layers of an inclined cone at Mach 6,” *Journal of Spacecraft and Rockets*, Vol. 51, No. 2, March–April 2014, pp. 442–454.
- <sup>30</sup> Willems, S., Gülhan, A., Juliano, T., and Schneider, S., “Laminar to turbulent transition on the HIFiRE-1 cone at Mach 7 and high angle of attack,” AIAA paper 2014–0428, Jan. 2014.
- <sup>31</sup> Schneider, S. P., “Design of a Mach-6 quiet-flow wind-tunnel nozzle using the e\*\*N method for transition estimation,” AIAA paper 98-0547, January 1998.
- <sup>32</sup> Li, F., Choudhari, M., Chang, C.-L., White, J., Kimmel, R., Adamczak, D., Borg, M., Stanfield, S., and Smith, M., “Stability Analysis for HIFiRE Experiments,” AIAA paper 2012–2961, June 2012.
- <sup>33</sup> Beresh, S. J., Henfling, J., Spillers, R., and Pruett, B., “Measurements of Fluctuating Wall Pressures Beneath a Supersonic Turbulent Boundary Layer,” Paper 2010-0305, AIAA, January 2010.
- <sup>34</sup> Boyd, C. and Howell, A., “Numerical investigation of one-dimensional heat-flux calculations,” Technical Report NSWCDD/TR-94/114, Dahlgren Division Naval Surface Warfare Center, Silver Spring, MD 20903-5640, October 1994.
- <sup>35</sup> Steen, L. E., “Characterization and Development of Nozzles for Hypersonic Quiet Wind Tunnel,” M.S. thesis, Purdue University (West Lafayette), December 2010, School of Aeronautics and Astronautics.
- <sup>36</sup> Juliano, T. J., Borg, M. P., and Schneider, S. P., “Quiet Tunnel Measurements of HIFiRE-5 Boundary-Layer Transition,” *AIAA Journal*, Vol. 53, No. 4, April 2015, pp. 832–846.
- <sup>37</sup> Stetson, K., Kimmel, R., Thompson, E., Donaldson, J., and Siler, L., “A Comparison of Planar and Conical Boundary Layer Stability and Transition at a Mach Number of 8,” AIAA Paper 91-1639, June 1991.
- <sup>38</sup> Stetson, K. F., “Nosetip Bluntness Effects on Cone Frustum Boundary Layer Transition in Hypersonic Flow,” 16th AIAA Fluid and Plasma Dynamics Conference, AIAA-83-1763, Danvers, Massachusetts, 1983.
- <sup>39</sup> Stetson, K. F., “Notes related to previous AIAA papers on blunt cones,” Personal communication to S. P. Schneider, Purdue University, West Lafayette, Indiana, December 2001.
- <sup>40</sup> Robarge, T. W. and Schneider, S. P., “Laminar boundary layer instabilities on hypersonic cones: Computations for benchmark experiments,” 19th AIAA International Space Planes and Hypersonic Systems and Technologies Conference, AIAA-2005-5024, Toronto, Ontario, 2005.
- <sup>41</sup> Marineau, E. C., Moraru, C. G., Lewis, D. R., Norris, J. D., Lafferty, J. F., Wagnild, R. M., and Smith, J. A., “Mach 10 boundary-layer transition experiments on sharp and blunted cones,”

19th AIAA International Space Planes and Hypersonic Systems and Technologies Conference, AIAA-2014-3108, Atlanta, Georgia, 2014.

<sup>42</sup> Wright, M. J., Candler, G. V., and Bose, D., “Data-parallel line relaxation method for the Navier-Stokes equations,” *AIAA Journal*, Vol. 36, No. 9, 1998, pp. 1603–1609.

<sup>43</sup> Johnson, H. B., “Thermochemical Interactions in Hypersonic Boundary Layer Stability,” Ph.D. thesis, University of Minnesota, Minneapolis, Minnesota, 2000.

<sup>44</sup> Johnson, H. B., Seipp, T. G., and Candler, G. V., “Numerical Study of Hypersonic Reacting Boundary Layer Transition on Cones,” *Physics of Fluids*, Vol. 10, No. 13, 1998, pp. 2676–2685.

<sup>45</sup> Stetson, K. F., “Hypersonic boundary layer transition experiments,” Tech. rep., Air Force Wright Aeronautical Laboratories, AFWAL-TR-80-3062, 1980.

<sup>46</sup> Jewell, J. S., *Boundary-Layer Transition on a Slender Cone in Hypervelocity Flow with Real Gas Effects*, Ph.D. thesis, California Institute of Technology, Pasadena, California, 2014.

<sup>47</sup> Bertin, J. J., *Hypersonic Aerothermodynamics*, AIAA, Washington, DC, 1994.

<sup>48</sup> Rotta, N. R., “Effects of nose bluntness on the boundary layer characteristics of conical bodies at hypersonic speeds,” Tech. rep., New York University, NYUAA-66-66, 1966.

<sup>49</sup> Stetson, K. F. and Rushton, G. H., “Shock Tunnel Investigation of Boundary-Layer Transition at  $M = 5.5$ ,” *AIAA Journal*, Vol. 5, No. 5, 1967, pp. 899–906.

<sup>50</sup> Goodwin, D. G., “An Open-Source, Extensible Software Suite for CVD Process Simulation,” *Proceedings of CVD XVI and EuroCVD Fourteen*, M Allendorf, F Maury, and F Teyssandier (Eds.), 2003, pp. 155–162.

<sup>51</sup> Moraru, C. G., “Hypersonic boundary-layer transition measurements at Mach 10 on a large seven degree cone at angle of attack,” Master’s thesis, Purdue University, West Lafayette, Indiana, 2015.

<sup>52</sup> Johnson, H. B. and Candler, G. V., “Hypersonic boundary layer stability analysis using PSE-Chem,” 35th Fluid Dynamics Conference and Exhibit, AIAA-2005-5024, Toronto, Ontario, 2005.

<sup>53</sup> Mack, L. M., “Boundary-Layer Stability Theory,” *Special Course on Stability and Transition of Laminar Flow*, edited by R. Michel, AGARD Report No. 709, pp. 3-1 to 3-81, 1984.

<sup>54</sup> Lei, J. and Zhong, X., “Linear Stability Analysis of Nose Bluntness Effects on Hypersonic Boundary Layer Transition,” *Journal of Spacecraft and Rockets*, Vol. 49, No. 1, 2012, pp. 24–37.



- <sup>55</sup> Reshotko, E., “Transient growth: A factor in bypass transition,” *Physics of Fluids*, Vol. 13, No. 5, 1998, pp. 1067–1075.
- <sup>56</sup> Kufner, E. and Dallmann, U., “Entropy-and Boundary Layer Instability of Hypersonic Cone Flows—Effects of Mean Flow Variations,” in *Laminar-Turbulent Transition*, ed. R. Kobayashi, Springer, Berlin-Heidelberg, 1995, pp. 197–204.
- <sup>57</sup> Schneider, S. P., “Effects of High-Speed Tunnel Noise on Laminar-Turbulent Transition,” *Journal of Spacecraft and Rockets*, Vol. 38, No. 3, 2001, pp. 323–333.
- <sup>58</sup> Alba, C. R., Johnson, H. B., Bartkowicz, M. D., Candler, G. V., and Berger, K. T., “Boundary-layer stability calculations for the HIFiRE-1 transition experiment,” *Journal of Spacecraft and Rockets*, Vol. 45, No. 6, 2008, pp. 1125–1133.
- <sup>59</sup> Jewell, J. S., Wagnild, R. M., Leyva, I. A., Candler, G. V., and Shepherd, J. E., “Transition Within a Hypervelocity Boundary Layer on a 5-Degree Half-Angle Cone in Air/CO<sub>2</sub> Mixtures,” 51st AIAA Aerospace Sciences Meeting including the New Horizons Forum and Aerospace Exposition, AIAA-2013-0523, Grapevine, Texas, 2013.
- <sup>60</sup> Jewell, J. S., Parziale, N. J., Leyva, I. A., and Shepherd, J. E., “Effects of Shock-Tube Cleanliness on Hypersonic Boundary Layer Transition at High Enthalpy,” *AIAA Journal*, in press, 2016.
- <sup>61</sup> Fedorov, A. V., “Receptivity of a High-Speed Boundary Layer to Acoustic Disturbances,” *Journal of Fluid Mechanics*, Vol. 491, 2003, pp. 101–129.
- <sup>62</sup> Fedorov, A. and Tumin, A., “High-Speed Boundary-Layer Instability: Old Terminology and a New Framework,” *AIAA Journal*, Vol. 49, No. 8, 2011, pp. 1647–1657.
- <sup>63</sup> Settles, G. S., *Schlieren and Shadowgraph Techniques*, Springer-Verlag Berlin Heidelberg, First ed., 2001.
- <sup>64</sup> Weinstein, L. M., “Large-Field High-Brightness Focusing Schlieren System,” *AIAA Journal*, Vol. 31, No. 7, 1993, pp. 1250–1255.
- <sup>65</sup> Smeets, G., “Laser Interferometer for High Sensitivity Measurements on Transient Phase Objects,” *IEEE Transactions on Aerospace and Electronic Systems*, Vol. AES-8, No. 2, 1972, pp. 186–190.
- <sup>66</sup> Smeets, G., “Laser-Interferometer mit grossen, fokussierten Lichtbündeln für lokale Messungen,” ISL - N 11/73, 1973.
- <sup>67</sup> Smeets, G., “Verwendung eines Laser-Differentialinterferometers zur Bestimmung lokaler Schwankungsgrössen sowie des mittleren Dichteprofiles in einem turbulenten Freistrahle,” ISL - N 20/74, 1974.

- <sup>68</sup> Parziale, N. J., Shepherd, J. E., and Hornung, H. G., “Differential Interferometric Measurement of Instability in a Hypervelocity Boundary Layer,” *AIAA Journal*, Vol. 51, No. 3, 2013, pp. 750–754.
- <sup>69</sup> Parziale, N. J., Shepherd, J. E., and Hornung, H. G., “Free-stream density perturbations in a reflected-shock tunnel,” *Experiments in Fluids*, Vol. 55, No. 2, 2014, pp. 1–10.
- <sup>70</sup> Fulghum, M. R., “Turbulence measurements in high-speed wind tunnels using focusing laser differential interferometry,” Ph.D. thesis, The Pennsylvania State University, 2014.
- <sup>71</sup> Hornung, H. G., “Experimental Hypervelocity Flow Simulation, Needs, Achievements and Limitations,” Proceedings of the First Pacific International Conference on Aero Sc. and Tech., Taiwan, 1993.
- <sup>72</sup> Parziale, N. J., “Slender-Body Hypervelocity Boundary-Layer Instability,” Ph.D. thesis, California Institute of Technology, 2013
- <sup>73</sup> Mack, L. M., “Linear Stability Theory and the Problem of Supersonic Boundary-layer Transition,” *AIAA Journal*, Vol. 13, No. 3, 1975, pp. 278–289.
- <sup>74</sup> Mack, L. M., “Stability of Axisymmetric Boundary layers on Sharp Cones at Hypersonic Mach Numbers,” Proceedings of 19th AIAA Fluid Dynamics, Plasma Dynamics and Lasers Conference, AIAA paper 1987-1413, Honolulu, Hawaii, 1987.
- <sup>75</sup> Jewell, J. S. and Shepherd, J. E., “T5 Conditions Report: Shots 2526–2823,” Tech Rep., California Institute of Technology, Pasadena, CA, June 2014, GALCIT Report FM2014.002.
- <sup>76</sup> S. J. Laurence, A. Wagner, K. Hannemann, V. Wartemann, H. Lüdeke, H. Tanno, and K. Itoh. “Time-Resolved Visualization of Instability Waves in a Hypersonic Boundary Layer,” *AIAA Journal*, Vol 50, no. 1, pp 243-246, January 2012.
- <sup>77</sup> S. J. Laurence, A. Wagner, and K., Hannemann, “Schlieren-based techniques for investigating instability development and transition in a hypersonic boundary layer” *Experiments in Fluids*, Vol. 55, pp 1782-1789, 2014.
- <sup>78</sup> K. M. Casper, S. J. Beresh, J. F. Henfling, R. W. Spillers, and B. O. M. Pruett, “High-speed Schlieren imaging of disturbances in a transitional hypersonic boundary layer” 51st AIAA Aerospace Sciences Meeting, AIAA paper 2013-0376, January 2013.
- <sup>79</sup> K. M. Casper, S. J. Beresh, R. M. Wagnild, J. F. Henfling, R. W. Spillers, and B. O. M. Pruett, “Simultaneous pressure measurements and high-speed schlieren imaging of disturbances in a transitional hypersonic boundary layer,” 43rd Fluid Dynamics Conference, AIAA paper 2013-2739, June 2013.

<sup>80</sup> C. P. VanDercreek, M. S. Smith, and K. H. Yu, "Focused Schlieren and deflectometry at AEDC hypervelocity wind tunnel No. 9," 27th AIAA Aerodynamic Measurement Technology and Ground Testing Conference, AIAA Paper 2010-4209, June 2010.

<sup>81</sup> D. R. Jonassen, G. S. Settles, and M. D. Tronosky, "Schlieren 'PIV' for turbulent flows," *Optics and Lasers in Engineering*, Vol. 44, No. 3-4, pp 190-207, Mar-Apr 2006.